Mathematical Modeling of Secondary Malignancies and Associated Treatment Strategies

by

Venkata Satya Manem

A thesis
presented to the University of Waterloo
in fulfillment of the
thesis requirement for the degree of
Doctor of Philosophy
in
Applied Mathematics

Waterloo, Ontario, Canada, 2014

I hereby declare that I am the sole author of this thesis. This is a true copy of the thesis, including any required final revisions, as accepted by my examiners.

I understand that my thesis may be made electronically available to the public.

Abstract

Several scientific and technological advancements in radiation oncology have resulted in dramatic improvements in dose conformity and delivery to the target volumes using external beam radiation therapy (EBRT). However, radiation therapy acts as a double-edged sword leading to drastic side-effects, one of them being secondary malignant neoplasms in cancer survivors. The latency time for the occurrence of second cancers is around 10-20 years. Therefore, it is very important to evaluate the risks associated with various types of clinically relevant radiation treatment protocols, to minimize the second cancer risks to critical structures without impairing treatment to the primary tumor volume. A widely used biologically motivated model (known as the initiation-inactivation-proliferation model) with heterogeneous dose volume distributions of Hodgkin's lymphoma survivors is used to evaluate the excess relative risks (ERR). There has been a paradigm shift in radiation therapy from purely photon therapy to other particle therapies in cancer treatments. The extension of the model to include the dependence of linear energy transfer (LET) on the radio-biological parameters and mutation rate for charged particle therapy is discussed. Due to the increase in the use of combined modality regimens to treat several cancers, it is extremely important to evaluate the second cancer risks associated with these anti-cancer therapies. The extension of the model to include chemotherapy induced effects is also discussed. There have been several clinical studies on early and late relapses of cancerous tumors. A tumor control probability (TCP) model with recurrence dynamics in conjunction with the second cancer model is developed in order to enable design of efficient radiation regimens to increase the tumor control probability and relapse time, and at the same time decrease secondary cancer risks.

Evolutionary dynamics has played an important role in modeling cancer progression of primary cancers. Spatial models of evolutionary dynamics are considered to be more

appropriate to understand cancer progression for obvious reasons. In this context, a spatial evolutionary framework on lattices and unstructured meshes is developed to investigate the effect of cellular motility on the fixation probability. In the later part of this work, this model is extended to incorporate random fitness distributions into the lattices to explore the dynamics of invasion probability in the presence and absence of migration.

Acknowledgements

It is a pleasure to thank those who made this thesis possible. First and foremost, I would like to thank my family for their unconditional support and encouragement throughout my PhD studies. I share the happiness of completion with my mother, sister and uncle, knowing this would not have been possible if not for their unconditional love and support. I would like to thank my supervisors, Prof. Siv Sivaloganathan and Prof. Mohammad Kohandel for their continuous support throughout my PhD program. Siv has always been there to guide me. I would like to express my deepest gratitude to Siv, as he was the one responsible for involving me in this mathematical medicine program, and also for his persistent support throughout my candidature. Mohammad was the one responsible for teaching me to formulate a biological/clinical problem, express research ideas, and taught me how to write good academic papers. Both Siv and Mohammad have been great mentors and instilled confidence in me when I doubted myself. A special thanks to Prof. Pino Tenti for teaching me what it takes to become a good teacher, presenter and a researcher.

I thank Prof. Jack Tuszynski, Prof. Adil Al-Mayah, Prof. Pino Tenti and Prof. Zoran Miskovic for serving as my committee members. Their valuable comments and suggestions have strengthened the quality of this thesis.

I would also like to thank Dr. David C Hodgson (Princess Margaret Hospital, Toronto) for helping me with his clinical expertise on secondary malignancies, and also for providing the relevant patient data. I am also grateful to Rachel Zhou (Princess Margaret Hospital, Toronto) who provided me with the radiotherapy images.

I would like to say "Thank You" to my fellow graduate students in the Biomedical research group, Dr. Hamid Molavian, Dr. Kamran Kaveh, Colin Phipps, Dr. Ali Mahdipour, Tahmineh Akhtar, Jonathan Murley, Ali Madani, Herbert Tang, Brandon May, Farinaz

Forouzannia, Andrew Dhawan. I specially thank Colin Phipps for his help in carefully reviewing and proof reading my papers and the thesis. Thanks to my other friends Dr. Mohammad Alwan, Dr. Hongtao Zhang and Dr. Wentao Liu for several lively discussions on math and life. I appreciate the friendship and support of my other friends Dr. Dhanaraja Kasinathan, Nithya Agatheeswaran for always being there when I needed the most. I enjoyed debates and discussions with Andree Susanto that covered topics from science to spirituality, and I also thank for all his help. Special "Thanks" to my dearest friend Pampa Dey who has been an inspiration and also for making life so meaningful. I would also like to thank Shivang Vyas, Shilpa, Nikky. Many thanks to all my other department friends Subasha Wickramarachchi, Daniel Otero, Alex Shum, Michael Dunphy along with other members of Applied Mathematics department for making my life in here so joyful.

I greatly acknowledge the financial support of NSERC, CIHR and assistantships from the Department of Applied Mathematics as well as University Graduate Student Office. Finally, I am thankful for the computing facilities provided by the MFCF (Department of Applied Mathematics), and a special thanks to Robyn Landers (from the MFCF) without which I'd surely still be waiting for some of my computational results.

Dedication

I dedicate this thesis to the loving memory of my father, who has been my role-model for hard work, and who instilled in me the confidence to achieve high goals. I also dedicate this thesis to my mother and sister who have been emotional anchors in my life.

Table of Contents

List of Tables

List of Figures

List of Abbreviations

BD Base Damage

CRT Chemo-Radio therapy

CT Chemotherapy

CTV Clinical Target Volume

DSB Double Strand Break

DVH Dose Volume Histogram

ERR Excess Relative Risk

GTV Gross Tumor Volume

HIT Heavy Ion Therapy

IFRT Involved Field Radiotherapy

IIP Initiation-Inactivation-Proliferation

INRT Involved Node Radiotherapy

IP Invasion Process

IV Irradiated Volume

LET Linear Energy Transfer

LQ Linear Quadratic

NHEJ Non-Homologous End Joining

PT Proton Therapy

PTV Planning Tumor Volume

RBE Relative Biological Effectiveness

RR Relative Risk

RT Radiotherapy

SSB Single Strand Break

TCP Tumor Control Probability

TV Treatment Volume

VM Voter Model

Chapter 1

Introduction

1.1 Cancer biology

Cancer may be viewed as a disease resulting in uncontrolled growth of cells within the body. Some of the reasons include (but are not limited to) are due to genetic changes, epi-genetic alterations, viruses, mutations and irregularities in metabolic functions. Cellular functions become abnormal due to genetic alterations or mutations, resulting in an uncontrolled growth of cells which manifests itself as a tumor over a period of time [1]-[3]. This abnormal behavior of cells can be due to several factors such as genetic, epi-genetic, micro-environmental variations, or other carcinogenic agents (which will be discussed in the next section). Carcinogenesis is generally viewed as an evolutionary process, because the pre-neoplastic lesions have to undergo several mutations in order to become neoplastic cells. In general, tumors can be distinguished as benign or malignant. A malignant tumor can invade the proximal tissue and can cause metastasis (i.e. migration and colonization of a different organ), and is considered to be fatal. A benign tumor is a non-malignant

cancer which is considered to be non-life threatening. There are two types of genes responsible for cancer initiation and progression, namely, oncogenes and tumor suppressor genes. Oncogenes (for instance, RAS) are genes that are believed to be responsible for healthy cells to become cancerous, which eventually leads to uncontrolled cell proliferation and tumor growth. On the other hand, tumor suppressor genes (for instance, P53) are those genes that inhibit abnormal cell proliferation, and protect the cell from the path leading to cancer.

The complexity and heterogeneity of cancer progression can be explained through somatic evolution of cancer where the process of cancer initiation and progression can be modeled through an evolutionary framework. The advent of pre-neoplastic cells in the system is controlled to some extent by its micro-environment. In fact, the micro-environment may or may not confer a fitness advantage to the pre-cancerous cell, eventually leading (in the former case) to invasion of neighboring tissue. It is commonly believed that pre-neoplastic or neoplastic cells gain a fitness advantage and take over a small neighborhood of host cells through a selection process and initiate a clonal area before expanding to neighboring tissue.

The most common treatment strategies in current clinical practice apart from surgery are chemotherapy and radiotherapy. All of these anti-cancer therapies can locally control the disease to a large extent, but at the same time can induce mutations in healthy tissue. These pre-neoplastic (also called pre-malignant or pre-cancerous) cells accumulate a number of genetic mutations, eventually leading to the development of a second cancerous tumor in one of the nearby organs of the primary tumor.

1.2 Second cancers

Advancement in radiation therapy techniques has improved the survival rate of cancer patients over the past two decades. This has come at the cost of some long term effects of the treatment. One significant concern for cancer survivors is the risk of developing a second primary tumor at later stages in their life. Radiation therapy is believed to be one of the major instigators of second primary tumors. Around 12% of patients who are diagnosed with cancer are treated with radiation. These patients receive high doses of radiation in the neighborhood of the tumor and low doses farther away from the tumor. The risk of secondary cancers increases with higher doses (both chemotherapy and radiation), dose-intensity and longer treatment times. The second cancer risk is much higher for organs that are close to the tumor treatment volume [4]. Second primary tumors are very evident among childhood cancer survivors [5]-[11]. The risk of second cancer is likely to be increased when combined modality treatments are used. In most patients these new malignancies occur in the same organ as the first primary tumor, or at a neighboring organ [7]-[13]. The most common second cancer is leukemia which takes approximately 5 years to occur while it takes solid cancers 10-15 years to develop [10].

When a target treatment volume is exposed to high doses of radiation (in particular due to the inaccuracy of the radiotherapy techniques and in particular the increase in beam-on time, i.e., the exposure time), the dosage is non-uniformly distributed over the general treatment area. This results in the neighboring normal cells of the tumor being irradiated. The normal cells which are located in the immediate vicinity of the tumor receive higher dosage than those located far away from the tumor. Most of the cancerous cells are eradicated but normal cells may undergo mutations, and become potential tumor initiator cells. If these initiated cells lose the capacity to repair themselves, they proceed

down a pathway that results in pre-malignant cells. These pre-malignant cells, over a period of time can undergo further mutations and give rise to a second malignancy in the same organ or other proximal organs. Thus, radiation decreases the number of cancerous cells but, in the process, initiates nearby normal cells to develop into pre-malignant cells. The further evolution of these pre-malignant cells gives rise to a second malignancy. Figure 1.1 shows a schematic representation of second cancer dynamics. The red colored cells

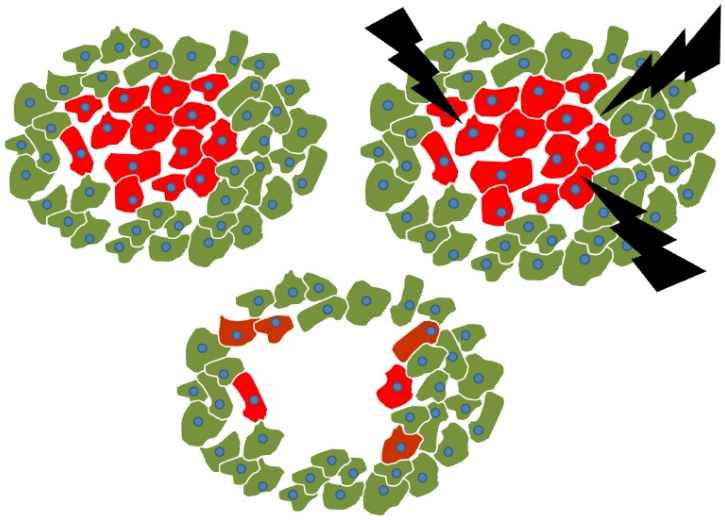

Figure 1.1: Schematic representation of second cancer kinetics.

represent the cancerous cells in the target volume, the green colored cells represent healthy cells which are located in the vicinity of the target volume, and the lightning denotes radiation that is used to inactivate tumor cells. Due to radiation some of the normal and pre-malignant cells become inactivated. Additionally, as a result of radiation, some normal cells are initiated to pre-malignant cells (which are represented in brown). After a couple of years or decades after irradiation of the tissue, the initiated normal cells (due to radiation) along with the leftover pre-malignant cells (if any) invade the neighboring tissue

niches until the tissue architecture is restored to its original structure. One of these pre-malignant clones undergoes additional mutations, invades the adjacent niches and forms a malignant tumor several years after irradiation. Figure 1.2 demonstrates the dynamics of second cancer evolution due to irradiation. As seen from Figure 1.2, the events that

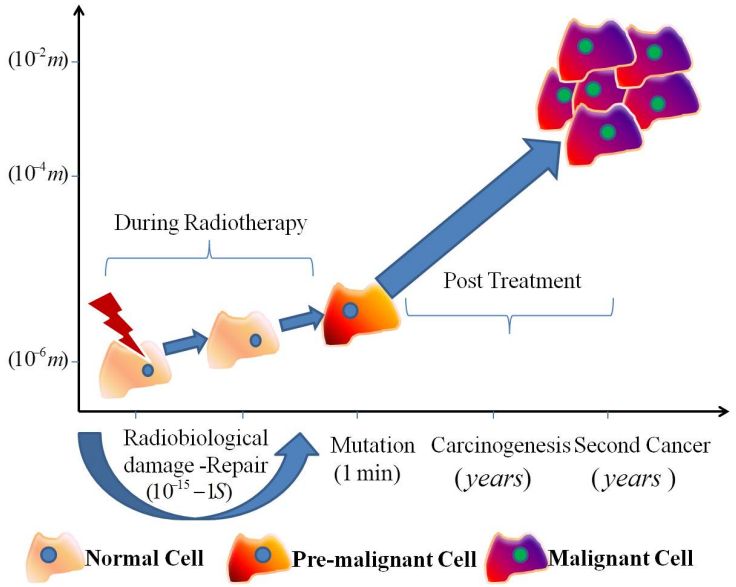

Figure 1.2: Evolution of secondary malignancy.

lead to radio-biological damage occurs at the order of nano to pico seconds. Depending on the type of DNA damage, the corresponding repair machinery kicks in to repair the cell, for instance, non-homologous end joining (NHEJ) gets activated to repair a double strand break. Mutation occurs if the cell is irreparable. This mutated cell proliferates, acquires a higher number of mutations and transforms itself into a malignant phenotype leading to a secondary malignancy. Second cancers are also known as radiation-induced primary tumors or second malignancies. It should be noted that second cancers are different from secondary tumors. From a clinical perspective, secondary tumors are metastatic cancers

that originate from the primary tumor volume. The main distinction between a second cancer and secondary tumor can be understood from the phenotype of a cancerous cell. As discussed earlier, a second cancer occurs in a new organ which is irradiated during radiotherapy, and secondary tumors arise as a result of cancerous cells that metastasize from the primary tumor.

1.3 Clinical rationale of radiotherapy

The planning process involves prescribing, recording and reporting a treatment schedule. Imaging techniques such as CT scan or MRI scans are employed to determine the exact location of the tumor as well as critical organs at risk in the vicinity of the tumor. A sketch of different volumes is shown in Figure 1.3 as defined by the International Commission for Radiation Units (ICRU 50, 1993) [12]. The Gross Tumor Volume (GTV) which is the actual location of the tumor is the most important volume required in the treatment planning. In order for the therapy to be successful, the clinical target volume (CTV) has to be effectively treated. During the treatment process, the geometry and position of the CTV might change. To account for these geometric uncertainties ICRU 50 defines the Planning Target Volume (PTV) as a volume obtained by considering all possible geometric variations during the process. The Treated Volume (TV) is the volume defined by the oncologist that encloses an isodose (absorbed dose is constant in a volume) surface. The Irradiated Volume (IV) is the volume that is irradiated due to the dosage.

Specific goals must be set on the desired dose to be delivered to the CTV taking into consideration the dose inhomogeneity, the minimum dose to be delivered to the organs that are at risk, and constraints on the dose fractionation schemes. Depending on the therapy used, a set of radiation beams are used to deliver the required dose. A critical part in the

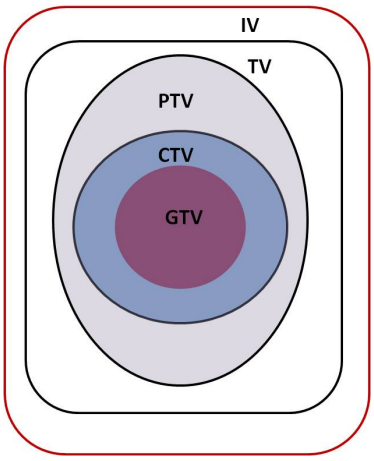

Figure 1.3: Organ delineation. Adapted from [12]

planning process is the calculation of dose distribution to the target volume. This is done by dose calculation algorithms like Broad-beam, Pencil-beam, Kernel-based and Monte Carlo which are software packages installed in the Treatment Planning Systems (TPS) [16]-[19]. Since they are not the subject or focus of my research, no further details will be given about these algorithms. The output of these algorithms is the dose distribution within a particular volume of interest summarized by means of dose volume histograms (DVHs) which are discussed in the next section.

1.3.1 Dose volume histograms

A DVH is a tool which displays a three-dimensional dose distribution in a two-dimensional graph. The main purpose of a DVH is to compare various treatment plans obtained from the TPS. Additionally, this is also used to validate the dose constraints on critical structures located on the vicinity of the tumor volume. There are two types of DVHs: differential and cumulative. The volume of interest is divided into smaller volume elements called voxels

of equal size such that the dose does not vary much in each voxel. The differential DVH is a histogram where each bin indicates the total volume of voxels receiving a specific range of dose assigned to that bin. The cumulative DVH has the x-axis as dose and y-axis as volume and each point on the graph describes the total volume that received greater than or equal to the dosage indicated on the x-axis. However, if the volume of interest is a moving organ, say a lung, then the concept of DVH can be redefined in terms of the dose mass histogram (DMH) which is a plot of the number of cells or mass against dose. DMH gives a better dose distribution than DVH if there is organ movement in the volume of interest. It should be noted that DVHs do not provide spatial information of dose. Figures 1.4 and 1.5 displays a sample cumulative and differential DVH delivered to bilateral lung tissue.

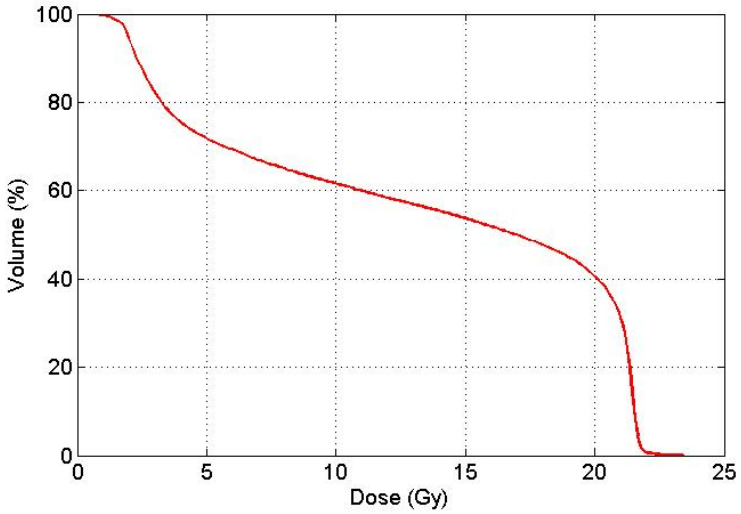

Figure 1.4: Cumulative dose volume histogram for bilateral lungs (Courtesy of Dr. D.C. Hodgson, Princess Margaret Hospital, Toronto).

Heterogeneous dose distributions are delivered using various external beam radiother-

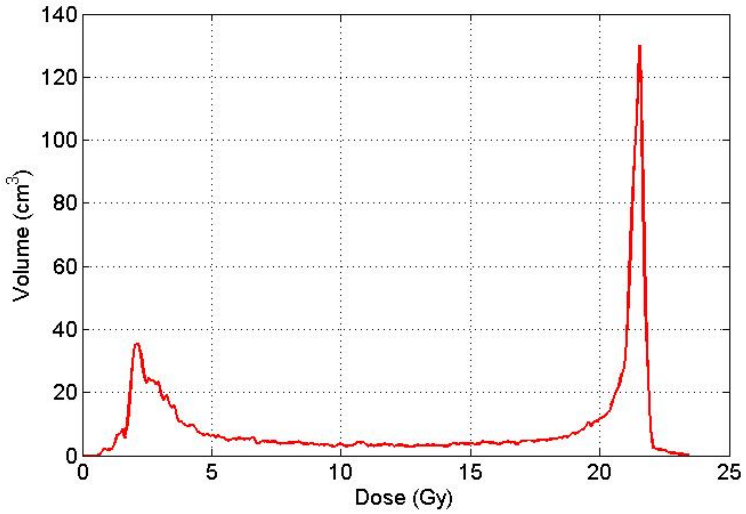

Figure 1.5: Differential dose volume histogram for bilateral lungs (Courtesy of Dr. D.C. Hodgson, Princess Margaret Hospital, Toronto).

apy techniques (EBRT). EBRT delivers dose from an external source through photons, protons, or ions. High energy beams are generated from the linear accelerator and directed towards the tumor volume, sparing the healthy tissue around the tumor. Some of the EBRT currently used include intensity modulated radiotherapy (IMRT), 3D conformal radiation therapy (3D CRT), Rotated Arc (RA) therapy, proton therapy and heavy ion therapy. The radiation quality depends on various dosimetric principles, which are discussed in the next section.

1.4 Features of radiation

1.4.1 Dose

One of the most important quantities in radiotherapy is the amount of dose that is absorbed by the biological medium. There are several terminologies used for specifying radiation dose and its effects on biological tissue. The most frequently used concept is that of the absorbed dose, which is defined as the amount of energy absorbed by the tissue, in unit of radiation, Gray (Gy) which is equal to 1 joule/kg. Occasionally, Gray is rescaled by rad where 1 Gy = 100 rad.

Another quantity that expresses radiation dose from various types of radiation is the equivalent dose. Different types of radiation have varied effects on biological tissue, due to which the absorbed dose is multiplied by a weighting factor (depending on the radiation type). Equivalent dose is usually expressed in sieverts (Sv), which is equal to 1 joule/kg.

Generally, radiation has varied effects on an organ depending on its anatomical structure and sensitivity. To account for these variations in tissue sensitivities, another quantity used is effective dose, where the absorbed or equivalent dose is multiplied by a tissue weighting factor. The unit of effective dose is also given in sieverts.

1.4.2 Linear energy transfer, relative biological effect and Bragg peak

The physical quantity that defines the variations in ionizing radiation is the linear energy transfer (LET). LET is defined as the amount of energy lost per unit path length as the beam traverses through tissue. According to the standards set by ICRU, LET is defined

as follows: *LET of charged particles in a medium is the quotient dE/dl, where dE is the average energy locally imparted to the medium by a charged particle of specified energy in traversing a distance of dl.*

It should be noted that LET is an average quantity whose units are keV/μm. There are several types of LET used in the literature such as track averaged LET, energy averaged LET and dose averaged LET (discussed in Chapter 4). The track average is estimated by dividing the track into equal lengths and averaging the energy deposited in each length. The energy average is calculated by dividing the track into equal energy intervals and averaging the lengths of the track that contain this amount of energy.

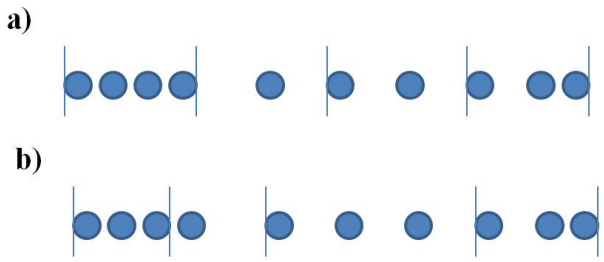

Figure 1.6: a) Track average and b) Energy average.

The biological effect of any radiation is usually expressed in terms of relative biological effectiveness (RBE). In general, equal doses of different types of radiation, say photons and protons, do not produce equal biological effect. In order to obtain the biological effect, say identical survival fraction of cells, RBE is defined as:

$$RBE = \frac{D_{\text{photons}}}{D_{\text{test radiation}}} \tag{1.1}$$

where, D_{photons} and $D_{\text{test radiation}}$ are the doses delivered by photons and test radiation respectively. In general RBE depends on the the type of biological end point (such as cell inactivation, initiation, etc), LET and tissue type.

One of the important features of particles used in radiotherapy is the Bragg peak. This is one of the fundamental reasons to exploit particle therapy in cancer treatments. Particle therapy, say for example protons, delivered at high doses to the target volume in a precise way, sparing the healthy tissue. Protons, being heavier particles, slow down faster than photons. As the proton travels through the biological tissue, it slows down by interacting with the medium and deposits more energy as it slows down. The absorbed dose increases gradually with lower speed and greater depth (of the tumor). At the end of its range (i.e. when the proton is ultimately stopped), the energy is suddenly deposited, rising to a peak. This phenomenon is known as the Bragg peak. Therefore, proton therapy is used to deliver radiation doses to those tumors (such as prostate cancer) that are located deep inside the tissue, such that healthy tissue is spared. Figure 1.7 is a caricature that displays the Bragg peak of a proton beam.

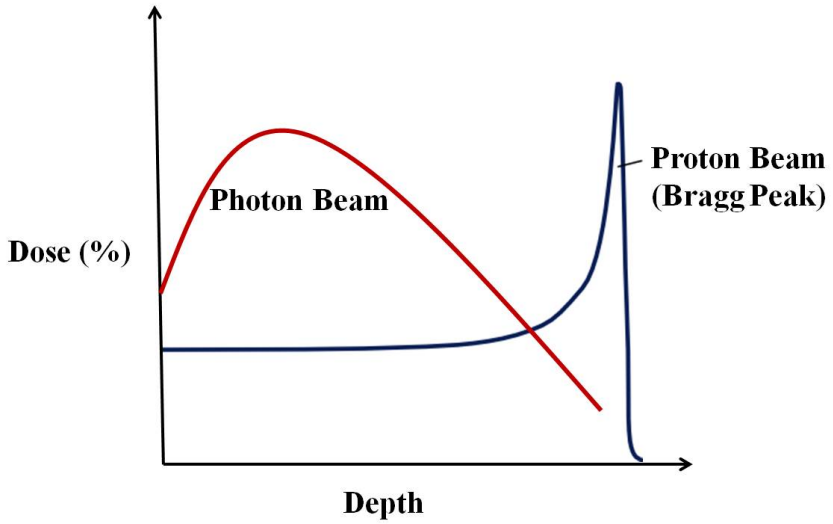

Figure 1.7: Schematic diagram of Bragg peak.

1.5 Late toxicities due to radiotherapy (RT)

In the last few decades, radiotherapy has replaced surgery for long term control of many types of cancers. Clinically, radiation therapy is considered to be one of the most effective therapeutic interventions to treat cancer. Additionally, it has gained importance in palliative treatments as well. Radiotherapy can be administered either externally (by using an external source of radiation) or internally (by surgically implanting a radioactive seed inside the tumor). In modern treatments, linear accelerators are capable of delivering the required dose precisely to the tumor volume.

There are several early and late toxicities associated with radiotherapy. Early toxicities are usually dictated by the anatomy of the critical structure that is irradiated. For example, irradiating the gastrointestinal tract can cause mucositis and irradiation of lung tissue can cause severe pneumonitis. Late effects arise due to radiation induced initiation, which eventually manifests as a second tumor after several decades post irradiation. Therapeutic effectiveness of a treatment paradigm is defined as maximizing the dose to the tumor volume with minimal toxicity to the healthy tissue. The manifestation of second primary tumors due to radiation primarily depends on normal tissue sensitivities (for instance breast tissue has a different sensitivity compared to prostate tissue). Historic radiotherapy treatments exposed larger volumes of healthy tissues, increasing the toxicity levels for induction of second cancers. As an example, we discuss the shift in treatment paradigms involved in treating Hodgkin's lymphoma (HL) disease. HL is a cancer that arises in the lymphatic system. Cancerous cells proliferate abnormally and may even spread to other organs. Techniques used in treating HL disease include extended beam RT, mantle RT, involved field radiotherapy (IFRT), and involved node radiotherapy (INRT). In the treatment of HL disease, traditional RT fields encapsulate the whole neck, bilateral axillae, the entire

length of the mediastinum, the spleen, and para-aortic nodes [13].The metamorphosis of historic RT to contemporary RT is displayed in Figure 1.8. All of the RT fields in Figure 1.8 are three dimensional reconstructions based on computed tomography (CT) imaging technique. The irradiated volume is represented by a light green color (and, the position of the heart is also shown). Panel A in the figure is the Mantle upper abdomen RT field.

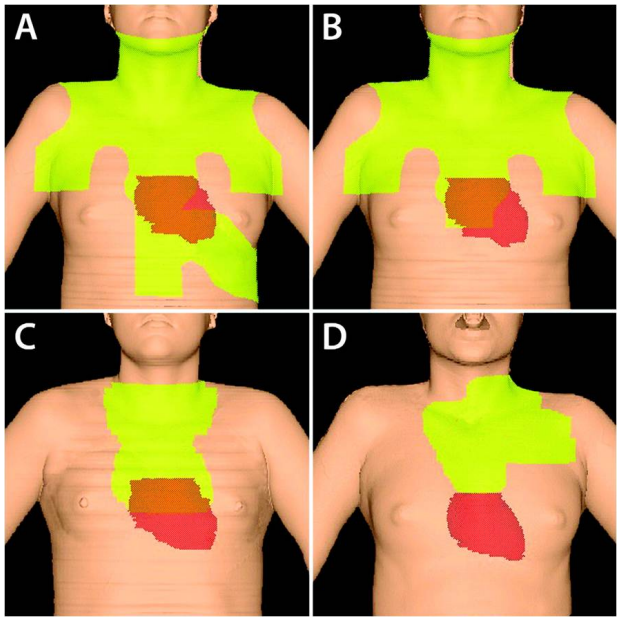

Figure 1.8: Evolution of RT fields from Mantle to Involved Node RT [13] (Courtesy of Dr. D.C. Hodgson, Princess Margaret Hospital, Toronto).

It should be noted that larger volumes of breast tissue and heart are exposed to radiation, and image in panel B represents mantle field. Mantle RT is usually associated with higher doses to axillary, mediastinal, and neck regions. Clinically, it is observed that there is a 2 to 20% increase in the relative risk (which is defined in chapter 4) of breast cancer and also lung cancer, depending on the diagnosis age of the patient. Panels C and D represent IFRT and INRT. Although it is very rare, in several cases, the spleen also gets

irradiated, which is considered to be a source of irradiation to left breast, lung and heart tissues. IFRT paradigm treats only those lymph node regions that are initially involved. For most patients with mediastinal disease, this technique excludes the axillae region, resulting in a reduction of dose to the breast and lung tissues. Simply speaking, IFRT is used for delivering a radiation dose only to those regions effected by lymphoma at the time of diagnosis. The change from traditional RT to IFRT has been shown to exclude most of the unwanted region that were being treated by extended beam RT. The substantial reduction of dose and volume to the normal tissue results in a decreased second cancer risk. Therefore, the reduction in second cancer risk is supported by volume reduction studies during treatment planning. INRT came into existence in order to reduce the field sizes compared to IFRT, which might further reduce second cancer risks. INRT fields do not comprise the entire nodal region, but all post chemotherapy volumes of the initially involved nodes. Although this is a new treatment paradigm, it might take several years to clinically evaluate the associated second cancer risks and the corresponding reduction of irradiated volumes.

1.6 Clinical example of HL disease

A sample treatment plan is discussed below, which is provided by Dr. D.C. Hodgson, Princess Margaret Hospital. Figure 1.9 shows a CT image of organ delineation. The nodal region being treated for this patient is the axillary lymph nodes, the supraclavicular lymph nodes, the hilar nodes and neck nodes. This plan is for the mantle treatment, delivering radiation to the mantle. All the contours in the image represent different organs. Red contour denotes shielding blocks to reduce radiation dose to the critical structures. Other organs included in the shielding are lungs, humeral heads, and the larynx. In female

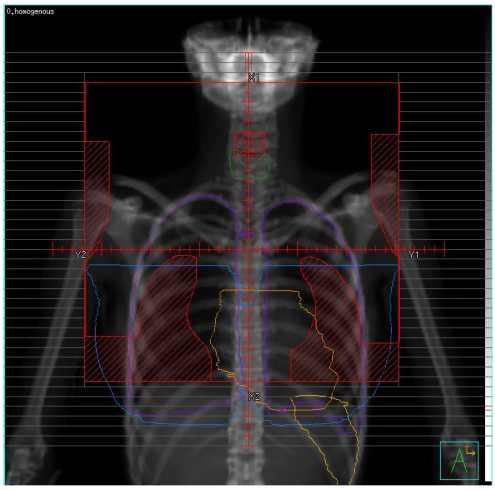

Figure 1.9: Organ delineation for HL disease (Courtesy of Dr. D.C. Hodgson, Princess Margaret Hospital, Toronto).

patients, partial shielding is carried out for the breast tissue too. Purple, blue, green, yellow, orange contours denotes shielding to lungs, breasts, thyroid, spleen and heart tissues respectively. Figure 1.10 displays a coronal slice, and the lines describe isodose curves. In this plan in particular, 2048 cGy was prescribed to the mantle isocentre (green circle with a cross) and then 2048 cGy to the yellow circle with a cross that is the abdomen isocentre. Figure 1.11 displays several beams emerging out from the linear accelerator, and different colors denote the field edges. The beams represent two different sites, mantle and spleen, i.e. two beams comprised of mantle treatment and two beams comprised of spleen treatment.

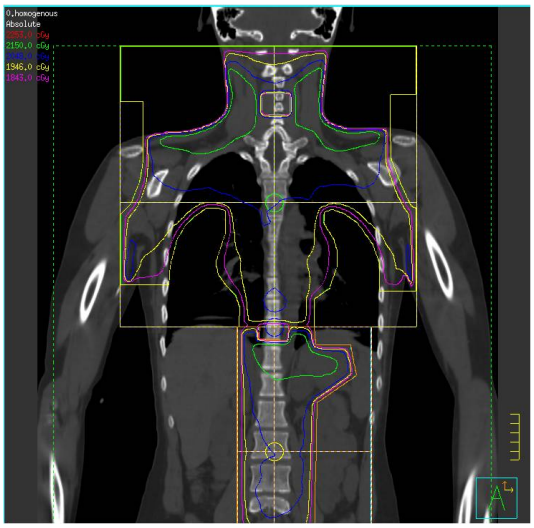

Figure 1.10: Three dimensional coronal view (Courtesy of Dr. D.C. Hodgson, Princess Margaret Hospital, Toronto).

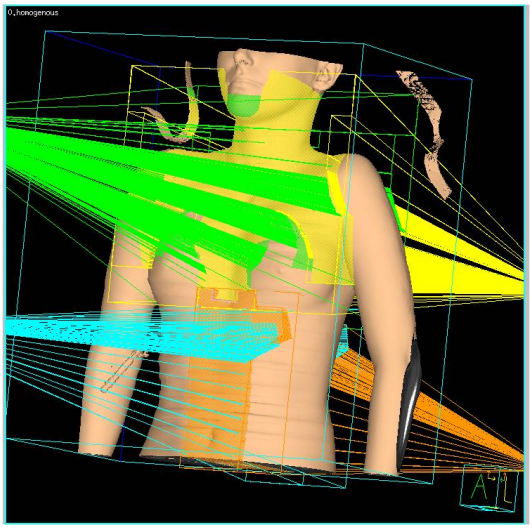

Figure 1.11: Radiation beams from the linear accelerator (Courtesy of Dr. D.C. Hodgson, Princess Margaret Hospital, Toronto).

1.7 Chemotherapy induced cancer

Chemotherapy is the process of administering drugs to kill cancerous cells. There are several negative implications of these cytotoxic drugs, and one of them is the killing or mutation of normal cells over the course of the treatment. Many alkylating agents used in primary cancer treatments are known to be potential carcinogens. Although these drugs are effective in treating aggressive tumors, they pose a high risk of chemotherapy induced second cancers. Recent clinical studies have identified a few types of cancers that are linked to chemotherapy, which include but are not limited to leukemia, breast and lung cancers in HL survivors [9]-[10]. Several case cohort and case control studies have reported that some chemotherapy agents increase ([112]) and some decrease the second cancer risks (for instance, procarbzine has tissue specific effects that leads to variations in the second cancer risks [113]-[114]). In most patients, chemotherapy is administered as a sole therapy or given in conjunction with radiotherapy. In these patients, however, there are several ongoing debates on the effect of chemotherapy on radiation therapy induced second cancers. For example, the data and analysis on the effect of chemotherapy on radiation-related risk of breast cancer have been under debate due to inconsistencies [14]-[15].

Most often chemotherapy drugs are combined with radiotherapy in order to achieve better disease control. A major leap towards an effective therapeutic benefit came from a cocktail of therapies such as adjuvant, neo-adjuvant and concurrent therapies. The administration of chemotherapy followed by radiotherapy is termed adjuvant therapy, while neo-adjuvant therapy is the administration of radiotherapy followed by chemotherapy. Concurrent therapy is the simultaneous administration of both chemotherapy and radiotherapy.

In this regard, numerous case control and epidemiological investigations have been carried out to investigate the effect of combined modality treatments on second cancer

risks. Travis et al. in his work [10] reported that the use of alkylating agents alone has a reduced breast cancer risk, and also observed a lower risk for a combined modality regimen compared to radiation alone. Clinical evidence supports the fact that hormonal stimulation is an important factor in cancer initiation and progression, particularly, in secondary breast cancer during and after the treatment.

1.8 Objectives and outline of the thesis

Mathematical models are now ubiquitous in cancer biology and will hopefully lead to a deeper understanding and resolution of some of the major questions facing cancer biologists and clinical oncologists. An important focus of current interest among clinical radiation oncologists is concerned with the side effects of anti-cancer therapies, which include chemotherapy and radiotherapy alone or as a combined regimen. It is of great importance to know the risk for a patient to develop a second cancer which could have been caused by the initial anti-cancer therapeutic modality. The central theme of this thesis is to estimate the second cancer incidence risk through the development of novel mathematical models, along with understanding the DNA damage induced by low energy protons. Survival probability of radiation induced pre-malignant cells is an important part of secondary tumor initiation. The second part of the thesis models the evolution of cancer initiating cells obtained from radiation, on spatial structures using an evolutionary dynamics framework.

Chapter 1 starts with an introduction to the biology of primary cancer and anti-cancer therapy induced second cancer. We briefly discuss various biological aspects of initiation and progression of second malignancies. Basic principles of dosimetry are defined and the fundamental aspects of radiotherapy treatment planning are also presented. The shift in the treatment paradigms from traditional to contemporary techniques are discussed along

with a clinical example. The role of chemotherapeutic drugs on radiation therapy and the effect of combined modality protocols on second cancers are discussed briefly.

In order to achieve therapeutic benefit from radiotherapy, one needs to investigate the radio-biological effects of ionizing radiation. There are several inaccuracies and biological uncertainties in the dosimetry in critical structures, so one has to resort to Monte Carlo approaches to evaluate the various biological end points. Chapter 2 presents a brief review of some fundamental concepts such as DNA, radiation induced radio-biological damage, basic interacting mechanisms of ionizing radiation (which include electrons, photons, protons) with the biological medium. A Monte Carlo tool kit, Geant4, is used to understand the probability of DNA damage irrespective of the location of the nucleus. As a particular case, we have considered low energy protons. This chapter is adapted from our paper which is currently under review [175].

Chapter 3 is devoted to mathematical modeling approaches found in the literature. We discuss the phenomenological approach of the cell survival model, and the definitions of relative and excess relative risks. The advantages and disadvantages of various models associated with estimating radiation induced carcinogenic risk are presented. This chapter gives the fundamental (biologically motivated) mathematical framework for second cancer modeling, which forms the basis for the subsequent chapters.

Chapter 4 presents a modified model of the initiation-inactivation-proliferation (IIP) formalism presented in the previous chapter. The IIP framework has been extended to include a radiation quality feature, importantly, LET of protons, alpha particles and heavy ions. Experimental data for cell inactivation and initiation was extracted for mono-energetic beams, and compared protons and alpha particles, along with heavy ions. This model demonstrates the importance of including LET in evaluating second cancer risks. This chapter is adapted from our paper which is currently under review [174].

Chapter 5 is concerned with the effect of combined modality treatments on second cancer risks. The aforementioned IIP framework is extended to include the effects of chemotherapy and radiotherapy. We compare various treatment strategies (that include adjuvant, neo-adjuvant and concurrent therapies), which are being used as contemporary treatment regimens. Various aspects of dose scheduling for chemotherapy and radiotherapy alone are also discussed. Although our second cancer risk predictions are theoretical, this study highlights and provides insight into designing an efficient combined modality treatment protocol that can minimize late toxicity to healthy tissue without impairing treatment to the primary tumor. An article discussing the mathematical framework and various results of this chapter is under review for publication [176].

Chapter 6 introduces a model to investigate the efficacy of radiotherapy dose escalation on second cancer risks for various fractionation protocols. We develop a mathematical framework by incorporating relapse dynamics and second cancer risk model into a tumor control probability model. We analyze the effect of dose escalation on various fractionated regimens and investigate an efficient protocol to reduce the risk of a secondary malignancy while maximizing local control of disease along with disease free survival. This chapter is adapted from our paper which is currently under review [177].

Chapter 7 presents a review of fundamentals in evolutionary dynamics from the perspective of cancer evolution. Evolutionary birth-death modeling on networks is discussed and the fixation probability on various structures are also addressed. The fixation probability on a two dimensional lattice in the presence of cellular motility is discussed, which forms a basis for the next two chapters.

In chapter 8, we extended the aforementioned evolutionary framework on lattices to unstructured grids and random meshes. We have modeled spatial structures that have random neighborhoods, in the presence and also in the absence of migration of cells. We

also examined the effect of boundaries on the fixation probability. This chapter is mainly adapted from our paper [170].

Chapter 9 deals with spatial evolutionary modeling with site dependent fitness of cells on a lattice. Several challenging questions are addressed, such as understanding the interplay between different types of spatial random fitness distributions (in the presence and absence of migration) on the fixation probability. This chapter is mainly adapted from our paper [178] that is currently in review.

Finally, we conclude the thesis with a brief discussion on the ideas presented, and address potential directions for the future work. In total, six papers (1-accepted and 5-currently under review) based on the work carried out during my PhD research have been submitted for publication.

Chapter 2

DNA Damage and Radiation Interactions

In this chapter, I will briefly discuss various phases of DNA damage through direct and indirect action of ionizing radiation. The interactions of electrons, photons and protons with a biological medium, and their basic mechanisms of energy deposition in the tissue, along with their track structures, are discussed. Finally, the probability density plots of DNA damage induced by a proton beam are presented.

2.1 Radio-biological damage

The most critical component of the mammalian cell is the nucleus. The fundamental functional unit in the nucleus is deoxyribonucleic acid, commonly referred to as DNA, which was discovered by Watson and Crick in 1953. The geometrical structure of DNA is double helixl with two strands (also known as backbone of the DNA). The main components

of each strand are sugar, which is a deoxyribose molecule, and a phosphate molecule which are alternatively placed. Each strand is comprised of four different bases: adenine (A), guanine (G), cytosine (C) and thymine (T), and the two strands are attached to each other by hydrogen bonds. Figure 2.1 illustrates a sample DNA fragment (taken from Wikipedia).

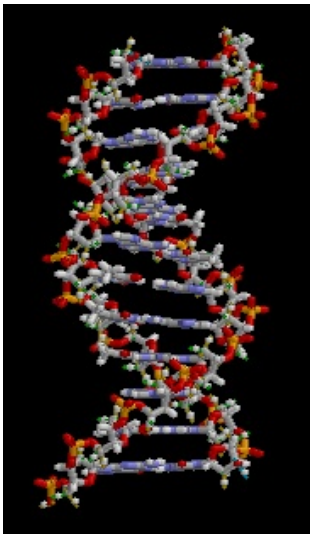

Figure 2.1: DNA molecule (Taken from wikipedia).

As ionizing radiation traverses biological tissue, energy is deposited. Energy that is absorbed in the medium may eventually lead to several biological effects in terms of radiation damage. Radiation injury can be in the form of targeted or non-targeted effects (related to endogenous reactions with the DNA). These endogenous reactions can instigate genomic instability, bystander effects, etc. There are several phases involved in the process of energy absorption in a biological medium. These processes occur at various time scales, eventually leading to either repair of the cell (if the cell is damaged), or to a mutated cell (if the cell is incompletely repaired). Figure 2.2 displays a caricature of various physical-chemical-biological mechanisms that occur as radiation traverses the tissue.

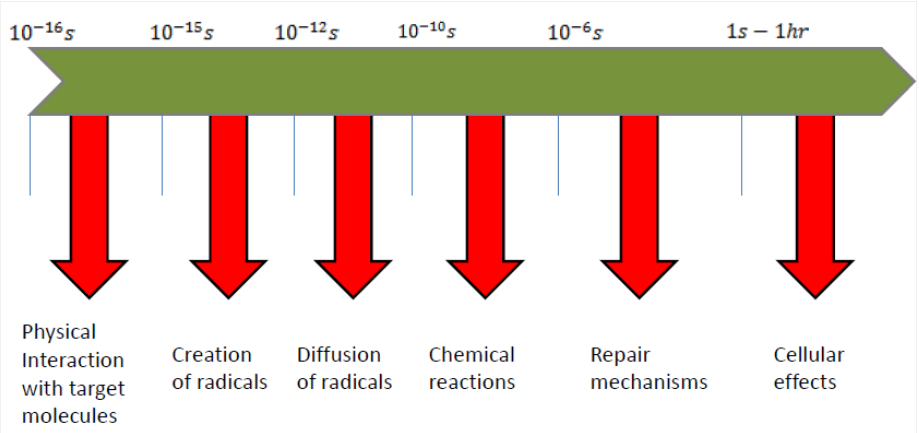

Figure 2.2: The catastrophe that occurs when ionizing radiation traverses biological medium.

When ionizing radiation passes through the medium, the initial events that occur is their interaction with several molecules, that happen on a time scale of $10^{-16} - 1$s. These events consist of ionization, excitation, scattering, and production of other secondary particles which eventually interact with the atoms of the target (mostly with water molecules) to produce ionizations, i.e. reactive oxygen species (or, free radicals) in the system. Then the chemical phase takes over, wherein, the reactive oxygen species that are produced at 10^{-12}s migrate and interact with various other molecules in the target. Since the life of free radicals is very short, they react instantaneously with the surrounding molecules, and these chemical reactions last only for a few milli-seconds. After the physico-chemical stages, the biological stage takes control, and triggers the repair machinery of the cell. Depending on the intensity of radio-biological damage, the repair mechanism can take several seconds to hours to repair it. If the DNA is incompletely repaired due to the complexity of the DNA damage, the after effects of this incomplete repair can either occur immediately, or, can manifest even after several years.

Radiation damage to the target molecules (inside the cell) causes malfunctioning of the cell. Radiation damage to the cell can be lethal, sub-lethal or potentially lethal. Lethal damage is irreversible, irreparable and leads to cell death; sub-lethal damage can be repaired within a period of time if there is no other sub-lethal damage that occurs within that same time period; potentially lethal damage occurs when the target cell is irreversibly modified by the post-irradiation environmental conditions. Cellular effects, particularly, the DNA damage induced by ionizing radiation can occur through direct or indirect effects. *Direct effect* is the direct action of ionizing radiation (i.e. ionizing some atoms) on the DNA molecule, which can happen only when the incident beam (and/or their secondary tracks) pass through the DNA molecule. This leads to several types of radio-biological damage depending on the spatial distribution of energy sub-cellular scales, i.e. at the order of nano-scale (which will be discussed later in this section). Therefore, it is clear that DNA damage also depends on the type of particle and initial energy of the incident beam.

Due to the smaller nuclear volume within a cell, there is a very small probability that ionizing radiation will directly hit the nuclear DNA. Therefore, most of the biological effects caused by radiation occurs through indirect action. *Indirect effect* is the action of ionizing radiation (i.e. ionizing some atoms) on the DNA molecule through free radicals in the system. Since a mammalian cell is composed primarily of water molecules (around 80%), ionizing radiation produces free radicals when it interacts with water molecules. These free radicals can be either atoms, molecules or ions which have an unpaired electron. Although there are several reactive oxygen species that can be formed in the system, the most effective and reactive one is OH^{-}.

The following (symbolic) chemical reactions describe production of OH^{-} ions. When ionizing radiation interacts with water molecules, an ion is produced by removing an elec-

tron from the water molecule:

$$H_2O \rightarrow H_2O^+ + e^-$$

This free electron in the above reaction interacts with another positively charged water molecule to produce a negatively charged water molecule, i.e.

$$H_2O + e^- \rightarrow H_2O^-$$

These positively charged water molecules undergo reactions to yield H^+ and OH^- ions as follows:

$$H_2O^+ \rightarrow H^+ + OH$$

$$H_2O^- \rightarrow H + OH^-$$

These ions might combine with other water molecules or free radicals in their vicinity. However, due to their short life time (approximately 10^{-9}s), they can migrate only a few nano-meters. Since most of the cell is comprised of water molecules, radio-biological damage to the DNA occurs mostly through indirect action, particularly in sparsely ionizing radiation, i.e. x-rays. Also, two ions of OH^- can combine to form hydrogen peroxide.

$$OH^- + OH^- \rightarrow H_2O_2$$

The life span of hydrogen peroxide is approximately 10^{-5}s [85], which also oxidizes several molecules in the vicinity, and inhibits nutrition from its neighboring cells. Indirectly, hydrogen peroxide restricts nutrients which leads to cell death. Additionally, the indirect effect caused by ionizing radiation through free radicals can be increased in the presence of oxygen concentration (or, other radio-sensitizers) in the system. This is because molecular oxygen reacts with the free radicals making them more stable, and thus fixing the radio-biological damage, which is termed as *oxygen fixation hypothesis* [85].

Radio-biological damage can take one of several forms such as base damage (BD), single strand break (SSB), double strand break (DSB) and a complex DSB. If the radio-biological damage occurs at any of the bases A, G, C, or T, then it is termed as base damage. The cell's machinery has a higher probability to fix this particular damage. SSB are damages that occur to either of the two backbones of the DNA molecule. Most of the SSBs occur only to one of the strands, and the repair probability to fix this damage is also quite high. Even though the number of SSBs are more in a DNA molecule, they are repaired quite efficiently by the cell. Due to high repair probability for an SSB, these do not contribute to any late biological effects. Double strand breaks are those damages that occur to both the strands. There can be several types of DSB damage- from a complex to a non-complex damage, and the probability to repair this type of damage is quite low. These mis-repaired cells are referred to as mutated cells, and these eventually lead to several late effects.

Ionizing radiation induces cell death through the following mechanisms: radiation-induced apoptosis, autophagy, senescence and mitotic catastrophe. Radiation initiates (or, activates) some signalling pathways to induce apoptosis. Autophagy is a degrading process of cellular elements, eventually leading to cellular death. Experiments have proved that radiation induced senescence occurs both in normal and also in cancerous cells. Senescence is a process of ageing that is introduced into the cell through shortening of the telomeres. Mitotic catastrophe is a process in which cells divide before being eliminated from the system.

2.2 Radiation interactions with matter

α-particles: An α-particle is composed of two protons and two neutrons with mass 6.6×10^{-27}kg. Due to the higher mass of the α-particle in comparison to the electron, deflection

as a result of collisions with electrons is negligible and the α-particle travels almost in a straight line in the tissue. When an α-particle traverses through matter it loses its energy through ionization and exicitation. Ionization is a process of converting an atom (or, molecule) into an ion by removing (or, adding) charged particles such as electrons. The α-particle has a double positive charge (due to the presence of two protons), which permits ionization by the formation of ion pairs. The traversing α-particle can either directly collide with the atomic electron knocking it off the orbit or it can excite the atom through coulombic interactions. The ion pairs thus formed consist of positively charged atoms and negatively charged ejected electrons. These free electrons have sufficient kinetic energy to cause further ionizations. Another mechanism through which energy loss occurs is by electron excitation. This happens when the α-particle does not impart enough energy to the atomic electron to knock it off its orbit, but simply shifts the electron to a higher orbital (or higher energy state). The excited elctron falls back to the lower energy state by emitting a photon. These effects lead to a change in the biological function of the cell, eventually causing damage.

The energy loss of the α-particle per unit path length (expressed as MeV cm^{-1}) is termed the stopping power of the medium for the α-particle, and is a quantity of central importance. Path length is defined to be the total distance travelled by the α-particle. The α-particles lose energy as they traverse through matter until the energy becomes zero and this distance is referred to as the range of the α-particle. Bethe [**?**] has derived the following expression for the stopping power of an α-particle [179]

$$S(E) = -\frac{dE}{dx} = \frac{1}{(4\pi\epsilon_0)^2}\frac{4\pi z^2 e^4 n Z}{mv^2}\left[\ln\left(\frac{2mc^2\beta^2}{I(1-\beta^2)}\right) - \beta^2\right], \tag{2.1}$$

where E is the energy and x is the path length, ϵ_0 is the vaccum permitivity (a physical constant that relates units of charge to mechanical quantities like force), z is the charge of

the α-particle, Z is the atomic number of the α-particle, e is the electron charge (which is 1.6×10^{-19} coulombs), n is the electron density of the medium, m is the electronic rest mass, $\beta = v/c$ (speed of the particle relative to speed of light c), I (units eV) is the weighted mean of the ionization and excitation process. The parameters that play a vital role are charge and velocity of the α-particle and the electron density of the medium. As the α-particle slows down in the tissue, more energy will be deposited at the end of the path leading to a peak, and this point at which the peak occurs is known as the Bragg-Kleeman curve.

Protons are positively charged particles with mass 1.6×10^{-27}kg. Protons being heavier in mass than electrons do not get deflected as easily after collision with electrons and hence move in a straight line. A proton can interact with the nucleus either elastically (i.e. after collision the proton gets deflected with some energy; the recoil nucleus gets scattered at some angle and the kinetic energy is conserved) or inelastically (i.e. where the kinetic energy is not conserved after the collision with the nucleus). Since protons have an electric charge, they interact with the electric field of the nuclei and also with the atomic electrons. Protons interacting with the nucleus experience elastic scattering while the interaction with the electrons is inelastic scattering. When a proton collides with an electron, partial energy is transferred to the electron which knocks it off its orbit leading to ionization. The ejected electron causes ionization of other atoms until it loses its energy. Protons penetrate further in the tissue than photons, for instance, x-rays, before the energy gets deposited at a particular site. This is one of the main reasons for recent interest in using proton therapy in the treatment of cancers. It is observed experimentally that the fluctuations in energy deposition per unit path length are small, and hence the energy loss is considered as an average quantity. The stopping power (or, the rate of energy loss) is then given by the Equation 2.1

Electrons are the most common light charged particles used in radiation therapy, for example, to treat skin cancers. They deposit energy in the tissue through two mechanisms: collisional losses and radiative losses. When electrons pass through matter, they lose energy by colliding with atomic electrons (also termed 'collisional losses') in matter which leads to ionization of the atom. Since particles participating in the collision are identical, large scattering angles are possible, which leads to the track becoming tortuous. Radiative losses occur because of the small mass of the electron. When the electron comes close to the atomic nuclei, the electron undergoes a change in deceleration and emits electromagnetic radiation referred to as Bremsstrahlung. The greater the change in the acceleration, the more energy in the Bremsstrahlung. This photon, when absorbed by an atom, excites the atomic electron to a higher energy state. If enough energy is imparted to the electron then it may get displaced from the nucleus leading to photo-ionization. Once again, an electron that falls to a lower energy state emits a photon of light.

Photons are quanta of electromagnetic radiation that have zero charge and zero rest mass. Photons can penetrate further than charged particles of similar energy. Photons with energy $E < 1$MeV are x-rays and with $E \geq 1$MeV are γ-rays. When a photon interacts with matter it can be absorbed or scattered by losing partial or total energy. Photons can lose energy through any of the following mechanisms: the photo electric effect, Compton scattering and pair production.

2.2.1 Track structure

The track structure of an electron, photon or a proton is determined by various physical mechanisms that occur at sub-cellular scales as they traverse the tissue. These include (but are not limited to) energy deposition in the biological medium, directions of various

secondary particles and their energy deposition in the medium, spatial distribution of ionization coordinates, etc. It is extremely complex to track individual tracks of particles using an experimental set-up. Therefore, the only methodology to observe these fundamental mechanisms is through Monte-Carlo approaches (MC). This tool kit has the ability to track the electrons in liquid water to the order of a few electron volts (eV). It has the capability to track primary and secondary electrons at the nano meter scale to a minimum threshold of 8.23 eV. The electrons are stopped below this energy, and they impart the rest of the energy to the biological medium. We used Geant4.9.5 software to model the track structure of various particles [20]-[22]. The tool kit encompasses all the Geant4 low energy physics models, and the physics calculations are based on these processes. Figure 2.3 presents a sample plot of ionization density for a single proton particle with 100 keV energy. A proton beam is shot from the center of a 10 μm cubic water phantom, and the red points in the graph denote the coordinates of ionization points.

2.3 DNA damage spectrum

As ionizing radiation traverses tissue, several chemical events occur that lead to radio biological damage. Lethal lesions to the DNA in the form of SSB, DSB and clustered DSB, might occur through direct action of particles, or through indirect action. In the past, radio-biological models and MC approaches have been developed to investigate the possible fundamental biological mechanisms of DNA damage. For the past several decades, MC simulations have played an impressive role in track structure calculations for various particles. Numerous MC approaches have been successfully employed to probe the spatial effects of radio-biological damage at sub-cellular scales, by investigating the track structures of the particles. Many authors have studied DNA damage through bio-physical

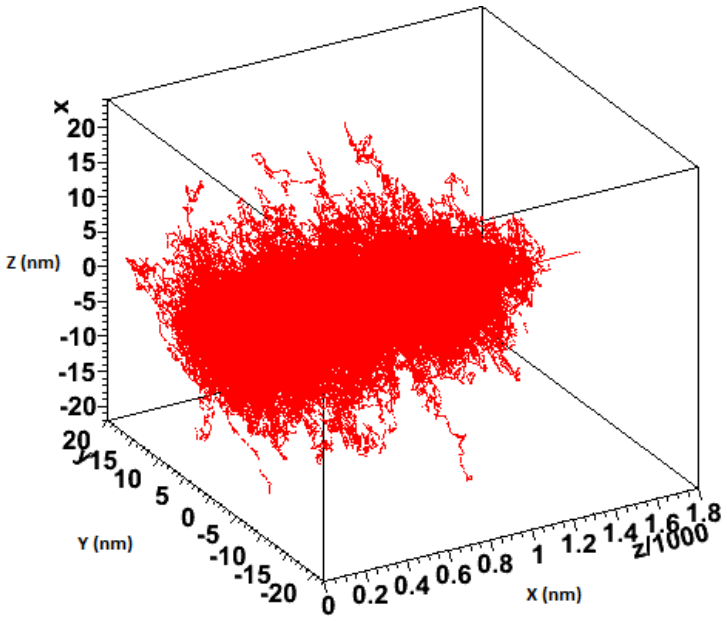

Figure 2.3: Track Structure of a 100 keV proton beam

modeling [23]-[28]. Brenner and Ward [29] reported that ionizations within $2-3$ nm sites correlate well with the experimental yield of double strand breaks. These works have been further extended to investigate the DNA damage in the form of double strand breaks [30]-[31]. When ionizing radiation interacts with biological tissue, several low energy secondary particles are produced which create multiple ionizations. These play an important role particularly in proton therapy in the plateau region of the Bragg peak. Since this plateau region is mostly located in the critical structure, it is of great importance to understand the spatial DNA damage caused by low energy protons. It is important to understand the formation of ionization clusters caused by low energy protons and investigate the relative biological effectiveness (i.e. DNA damage) of proton beams in the plateau region of the Bragg peak.

Most of the MC models in the literature consider the action of ionizing radiation on a

DNA molecule by overlapping a fixed geometry (either helical or cylindrical) in a specific cellular volume (say, in liquid water, or, in water vapor). Recently Bryne et al. [32] investigated the effect of ionizing radiation in a cellular phantom, which is composed of several chemical components of a cellular cytoplasm. Although it is very important to understand the spatial effects of radiation on a single DNA strand, this might not give an accurate description of DNA damage in a cell of different geometry. This is because, biologically, cells can have varied geometries (for example, the geometry of a normal epithelial cell is different from a mesenchymal cell, endothelial cell and a cancerous cell). Additionally the location and the size of nuclear DNA might vary for every individual cell. Experimental

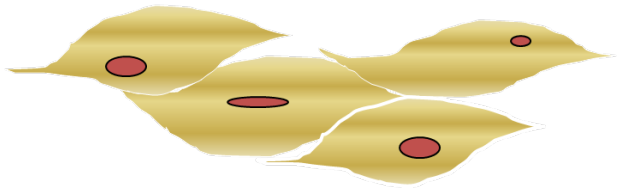

Figure 2.4: Various cellular geometries

observations have reported that some cells have smaller nuclei compared to others. Also, several biological experiments support the fact that the nucleus of a mammalian cell can take any shape, whose position is also not fixed within a cell. Figure 2.4 displays variations in the nuclei position within a cell (of different geometries). Given these cellular variations within a tissue, it is important to study the probability distribution of DNA damage within a given cell for any given type of ionizing radiation, irrespective of the position of the nuclei.

The effects of various micro-environmental conditions are ignored in this investigation on the spatial DNA damage. We present results related to the formation of radiation induced nano-metric ionization clusters by low energy protons as well as the probability density plot of DNA damage (double strand breaks) within a given system, using MC

simulations. Low energy protons are considered in order to understand the effects resulting from stray radiation (from the linear accelerator) and scattered radiation (from the primary radiation field to the out-of-field region).

To model proton interactions with the biological tissue, we used the open source MC simulation software Geant4.9.5 [20]-[22]. We implemented proton particles as mono-energetic beams of zero width in a liquid water phantom. Experimentally it is suggested that the dimension of a cell is approximately $10\,\mu$m, so we chose the size of the water phantom to be around $10\,\mu$m, with its center at the origin. The incident particles are shot from the center of the water phantom in the Z direction, i.e. along $(0, 0, 1)$. This simulation is carried out for several energies with a single proton particle: 100 keV and 1 MeV. Additionally, we have investigated the correlation between the number of incident proton particles (with $10, 20, 30$, and 40), and its effect on the distribution of nano-metric ionization clusters, and the corresponding probability density within the water phantom. Since the nuclear DNA can be located at any position within the phantom, we divided the 10μm box into several nano-voxels of dimension $2 \times 2 \times 2$ nm. This is done in order to understand ionization cluster distribution within a nano-metric volume. The probabilities of DNA damage are then estimated for a given nano-metric cluster with n number of ionizations. Grosswendt et al. [37] suggested a functional form for calculating the probability of double strand breaks (DSB). Recently, Garty et al. [38]-[39] in their work proposed a conditional probability formula based on a combinatorial formulation. The authors predicted the distribution of the number of DNA strand breaks for a given distribution of ionization clusters. Let p_c be the probability that a single ionization results in a strand break. Based on the assumptions that this probability is independent of the location of the ionization in the phantom, Lazarakis et al. [40] estimated the conditional probability

for a DSB given a cluster of ν ionizations to be:

$$P(DSB|\nu) = 1 + (1 - p_c)^{\nu} - 2\left(1 - \frac{p_c}{2}\right)^{\nu}. \tag{2.2}$$

In general, p_c is an adjustable parameter which may depend on several biological conditions in the given system. For simplicity, in all the calculations in this work we choose a constant value of $p_c = 0.1$.

As evident from the Figures 2.5–2.7, the probability of a double strand break is high close to the beam path. It should also be noted that the probability of a DSB still exists, although very small (and not zero), away from the beam path. The ionization distribution for protons is mostly concentrated along the beam path without any scattering. The total number of ionizations increases with beam energy and number of particles. As observed from the probability density plots, the maximum probability of DNA damage is high close to the beam path, indicating that most of the ionizations occur along, or in the vicinity of the beam path. The ionization cluster distribution increases as the number of particles in the proton beam increase. Also, the probability increases due to an increase in the number of ionizations within a nano voxel. Particularly, for 1 MeV proton beams whose range is on the order of the dimension of a cell (i.e. 10 μm), the probability of DNA damage depends on the location of the nuclei. If the nucleus is along the beam path, then the DNA damage occurs through direct or indirect action. Even if the beam misses the target by a few nanometres (less than 5 nm), the probability of DNA damage through indirect action is still quite high. However, if the nucleus is located within a distance of 10 nm from the beam path, there is still a small probability of DNA damage. From our preliminary investigations, we conjecture that the biological effectiveness also depends on the geometry of the cell along with the position of the target within the cell. Our results demonstrate the need for several experimental studies to understand radiation induced

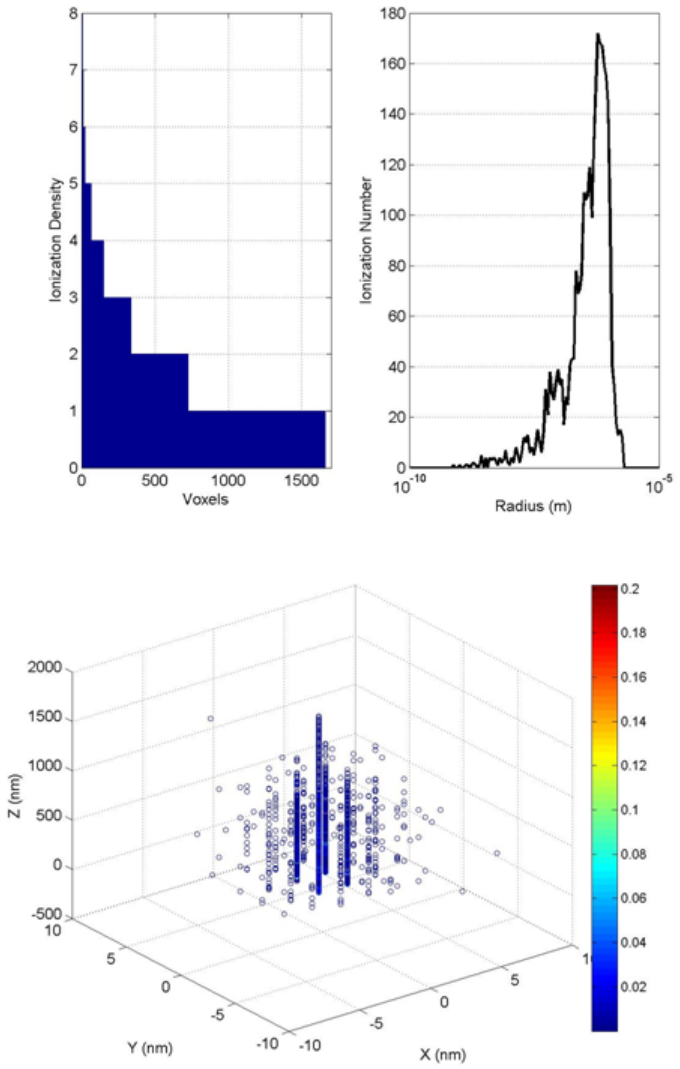

Figure 2.5: Ionization distribution frequency, radial distribution of ionizations and probability density plot induced by a single proton beam of energy 100 keV.

effects for several types of cells, including non targeted effects due to ionizing radiation. These results also provide insight into the variations in relative biological effectiveness of a beam which plays a crucial role in studies of radiation injury, and particularly, in

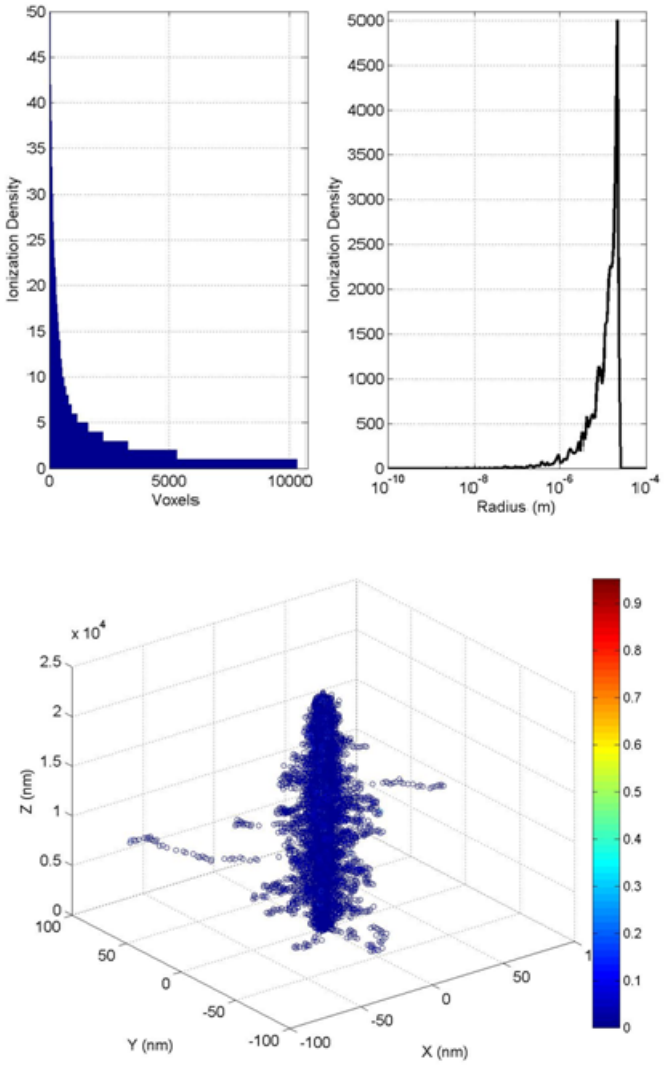

Figure 2.6: Ionization distribution frequency, radial distribution of ionizations and probability density plot induced by a single proton beam of energy 1000 keV.

the estimation of secondary cancers risks. In order to understand radiation induced tissue injury, numerous experimental studies are required using multiple beams with various fields at sub-cellular scales.

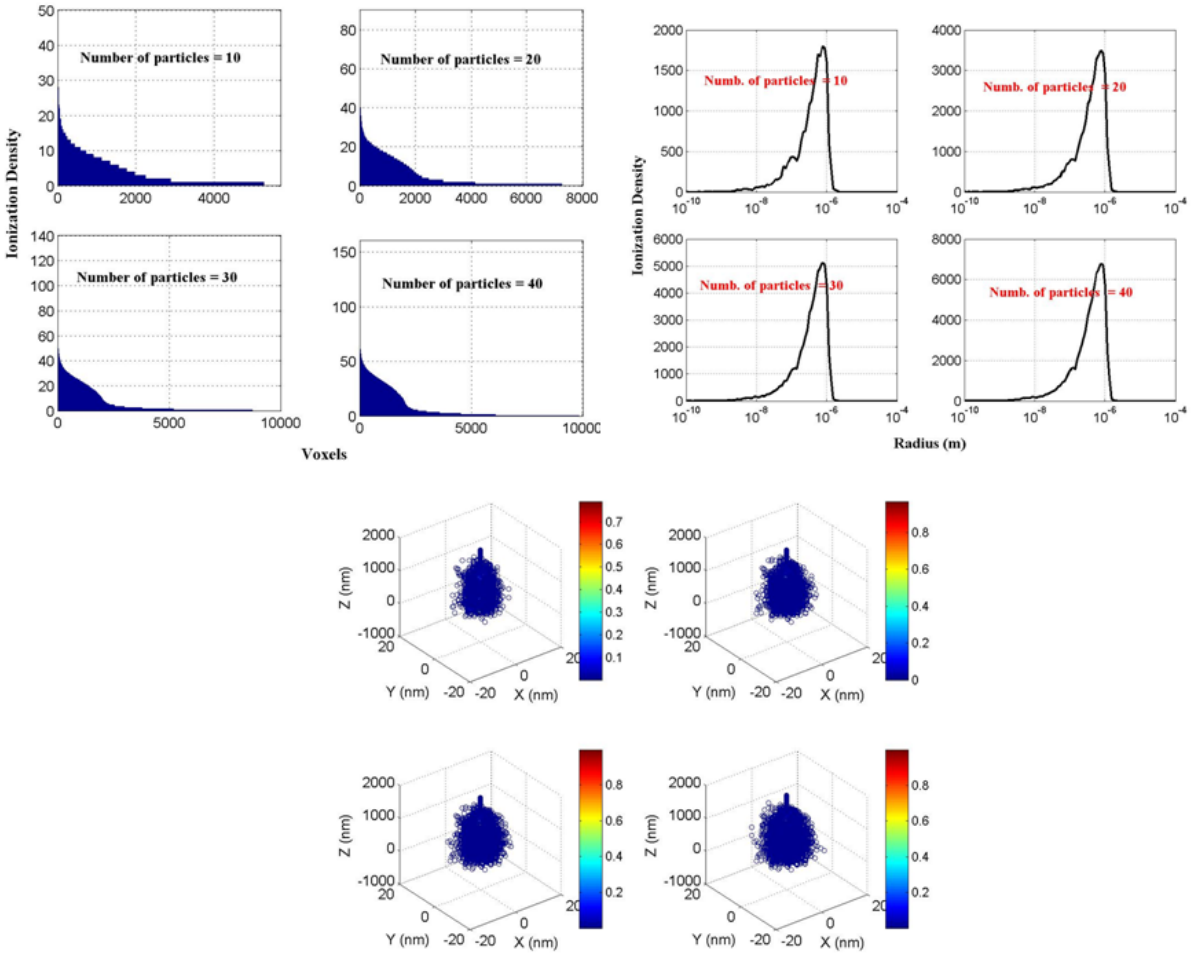

Figure 2.7: Comparison of frequency and radial distributions of ionizations along with the probability density plots induced by 10, 20, 30, 40 particles of single proton beam of energy 100 keV.

2.4 Short summary

In the present chapter, we have discussed the interaction of ionizing radiation with biological media and various biological aspects of radiation-induced DNA damage. We have

shown that the biological effectiveness (i.e. double strand break damage) also depends on the geometry and the location of the nuclei within the DNA through probability density plots. Incidentally, several potential applications are associated with this study in terms of understanding both targeted and non-targeted effects of radiation during cancer treatment in the form of stray radiation dose, medical imaging (e.g. mammography, computer tomography (CT)) and radio-protection. Radiation induced endogenous reactions with the DNA can instigate fibrosis, and cause genomic and chromosomal instability, as well as by-stander effects, oxidative stress and inflammation [33]-[35]. Further, secondary tumors have been reported by several authors [36]. Also, the spatial distribution of ionization clusters, which results in the probability density of DNA damage within the system (a cell), might also influence the value of the relative biological effectiveness (RBE) of a proton beam. RBE mainly depends on the linear energy transfer (LET) as well as on several micro-environment factors such as oxygen concentration. Since, LET is defined as the averaged energy deposition per unit distance travelled by the particle, the spatial distribution of ionization clusters at the sub-cellular scale, along with the location of nuclear DNA in a cell could play an important role in estimating the probability and/or the yield of DNA damage. These results might play a key role in several experimental investigations on radiation induced cellular effects along with non-targeted effects for various geometries of cells.

Chapter 3

Mathematical Modeling of Second Cancer Risks

In this chapter, I will briefly discuss the cell survival model used in radiotherapy, along with different types of risks associated with radiation-induced cancers. Mathematical models related to radiation-induced second cancer risks are presented in detail.

3.1 Cell survival model

A relationship between the dose delivered and the cell kill is given by the cell survival curve. The survival curve plots the dose delivered against the number of surviving cells. The earliest model was the single hit target model, wherein, a single event causes cell inactivation; this applies to biological targets such as bacteria and viruses [41]. It is assumed that energy deposition (or energy hits) is governed by a Poisson distribution, and during radiation there are a large number of hits on different cells. If S denotes the

surviving fraction of cells and D the dosage then the probability of the next hit occurring in a given cell is very small and given by $S = \exp(\lambda)$, where $\lambda = -D/D_0$ represents the dose that gives an average of one hit per target molecule within the cell. When $\lambda = 1$ i.e., when $D = D_0$ then $S = 0.37$. An extended model known as the single hit multi-target model, was proposed to obtain survival curves for mammalian cells. It is assumed that there are a number of targets in a cell and one hit by radiation on each of those sensitive targets in a cell is required for death of the cell. The probability of zero hits on a target is $P(0 \text{ hits}) = \exp(-D/D_0)$, hence the probability that a target is hit is $P(\text{a target is hit}) = 1 - \exp(-D/D_0)$. Since the theory assumes that there are n targets in the cell, hence $P(\text{all } n \text{ targets are hit}) = (1 - \exp(-D/D_0))^n$. Therefore, the survival probability, i.e., all the targets will not be hit is given by $P(\text{cell survival}) = 1 - (1 - \exp(-D/D_0))^n$.

Later, Chadwick and Leenhouts [42] improved the existing models and proposed a new model known as the Linear-Quadratic (LQ) model. The model has two components: a linear and a quadratic component. For the linear term, DNA damage occurs when a charged particle traverses through the cell, which is similar to that of the single hit model and hence the surviving fraction is $S = \exp(-\alpha D)$. For the quadratic term the DNA damage is caused by more than one charged particle. The probability that one DNA break occurs is proportional to the dose D and the probability that the second DNA break occurs is an independent event which is also proportional to the dose D. Therefore, the probability that both the events occur is βD^2 and the surviving fraction is $S = \exp(-\beta D^2)$. After combining linear and quadratic terms we obtain the surviving function as:

$$S = \exp(-\alpha D - \beta D^2). \tag{3.1}$$

In Equation (3.1), $\alpha\,(\text{Gy}^{-1})$ denotes the direct action of cell killing (which is lethal) and $\beta\,(\text{Gy}^{-2})$ denotes two track action where damage from two different radiation tracks interact to inactivate the cell. Both α and β are tissue dependent parameters. The ratio

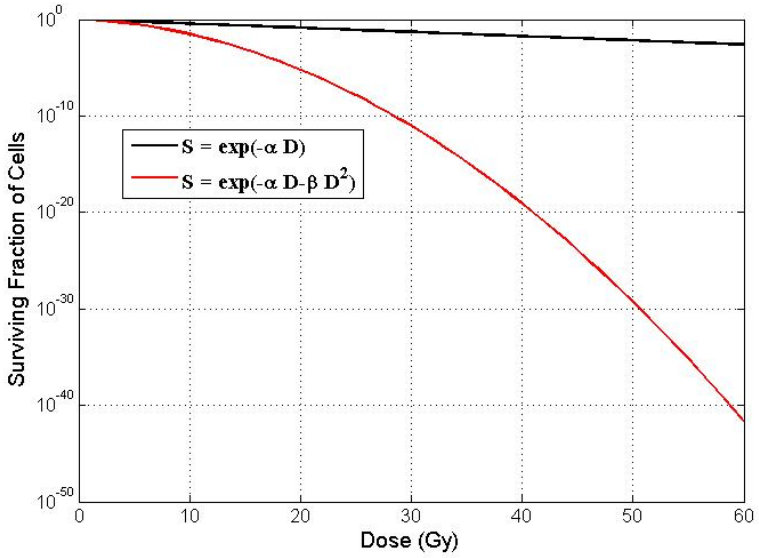

Figure 3.1: Survival fraction of cells due to an acute dose D. Parameters: $\alpha = 0.1(\text{Gy}^{-1})$, $\beta = 0.01(\text{Gy}^{-2})$

α/β defines the type of tissue that is being considered. For tissues with early effects, the value of α/β is high, the linear value is more important and hence there is less dependence on fractionations. For tissues with late effects, the value of α/β is low, the quadratic term becomes important and fractionation becomes relevant. Figure 3.1 displays a plot of surviving fraction of cells against acute dose D. The linear component denotes that cell killing is lethal and irreparable, and the surviving fraction is given by $S = \exp(-\alpha D)$. The effect of the quadratic term on the surviving fraction comes from the repair mechanisms. This quadratic component resembles the ability of a cell to self-repair, and is considered to be less lethal. Later, the LQ model has been extended to include the effects of cell cycle, redistribution, re-oxygenation, cellular proliferation, etc during fractionated radiotherapy[180].

3.2 Cancer risk

There are two important types of risks used in the literature, namely absolute risk and relative risk to quantify cancer risks. Absolute risk is defined as the probability that an individual is diagnosed with cancer during a specific time period in a given cohort. On the other hand, relative risks (RR) are used to describe the relationship between the risks in different groups. In other words, it gives the strength of relationship between cancer and a particular risk factor (such as ionizing radiation). It is defined as the ratio of probabilities of an exposed group to an unexposed group. If two groups have risks, say, R_1 and R_2 then $RR = R_1/R_2$. In many scenarios, it is useful to describe the risk $R_1 = R_2 + E$ where E is the excess risk. Then

$$RR = 1 + \frac{E}{R_2},$$

where the term E/R_2 is known as the excess relative risk. If $RR = 1$, then exposed and unexposed groups have equal chance of getting a disease; $RR > 1$ then exposed group is more likely to get the disease; $RR < 1$ then exposed group is less likely to get the disease than the unexposed group. ERR gives the percent increase above the normal incidence rate of a disease. For dose-response analysis ERR is measured to estimate the risk. It should be noted that these risks change over time due to various factors such as changes in food habits, environmental, biological, etc. However, the work presented in this thesis does not take into account the exposure or attained age of the patient.

The organ specific second cancer incidence due to ionizing radiation is proportional to the yield of pre-malignant cells at the end of the treatment. Therefore, the functional form used to obtain the excessive relative risk (ERR) estimate is given as the product of the yield of pre-malignant cells at the end of the treatment and a proportionality factor as

$$ERR = F(D)\, G(a, e, g) = M \times B \tag{3.2}$$

where $F(D)$ gives the number of radiation induced initiated pre-malignant cells. The second term $G(a, e, g)$ is a constant that depends on age at exposure a, time since exposure e and gender g. This is standard practice in the modeling of cancer risks as a result of ionizing radiation. It is evident from Equation (3.2) that the yield of pre-malignant cells given by $F(D) = M$ is dependent only on the radiation protocol and independent of patient age. The factor $G(a, e, g) = B$ is independent of radiation dose, but dependent on time. Since the incidence of second cancers is a multi step carcinogenic process post irradiation, the term B accounts for all these slower biological processes.

3.3 Mathematical models

Several models (using epidemiological, radio-biological and mathematical frameworks) have been identified in the literature for estimation of second cancer risks following radiation [44]-[63]. These have been extended by considering the influence of fractionation, dose distribution in the target volume, cell repopulation and inducible repair, etc [64]-[66]. However, we mainly focus on the radio-biological (also known as the initiation-inactivation) formalism, and mathematical (or, initiation-inactivation-proliferation (IIP)) model to estimate radiation-induced second cancer risks. Additionally, the uncertainties involved in modeling second cancer risks using radio-biological models will be discussed in detail. Finally, I will discuss the corrections made to the radio-biological model of Sachs et al. [53] and the resulting predictions which are compatible with the available clinical data. There are two classes of IIP models that are used to understand radiation induced carcinogenesis-short term and long term formalisms. Short term formalisms provide a detailed initial dose response relationship during the time of radiation treatment. Long term models formulate and track carcinogenesis. Throughout this thesis, we consider only the deterministic (short

term) formalism that occurs during radiotherapy.

Also, a single estimate of second cancer risk would underestimate or overestimate for any given cohort. Hence, the motivation to analyze individual estimates of second cancer risk for each patient is important, which can provide risk estimates for more contemporary radiation protocols. The importance of including the heterogeneous dose volume distribution (through the dose volume histograms) into second cancer models will be discussed.

3.3.1 Linear model

The simplest model used to evaluate radiation-induced cancer risks is through the linear model used in [67]. The ERR for a critical structure is given by:

$$ERR = ERR_D \times \bar{D}, \tag{3.3}$$

where ERR_D is the ERR per dose obtained from the epidemiological data, and $\bar{D}$ is the mean dose received by the healthy organ. This model turned out to be highly inconsistent with the epidemiological data. The risk estimation using the linear model holds true at low doses (< 3 Gy), but breaks down at intermediate and high doses. From Figure 3.2, it is clear that the linear model holds in the low dose region.

3.3.2 Initiation-Inactivation model

The initiation-inactivation model is also known as the non-linear model [60]-[61]. To investigate radiation-induced cancers, we have to consider the probability of radiation induced mutations and the survival probability of irradiated cells. United Nations Scientific Committee on the Effects of Atomic Radiation (UNSCEAR) [43] has proposed an expression

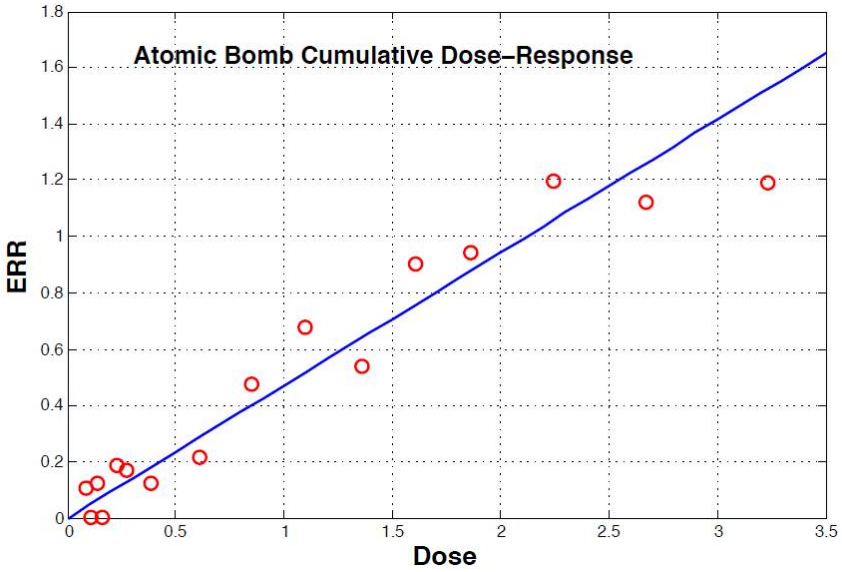

Figure 3.2: ERR vs. dose (data points extracted from epidemiological data [59]

relying on the LQ model. Based on the LQ model, the probability that a cell survives a dose D is given by Equation (3.2).

Therefore the probability that a cell escapes radiation, i.e. escapes radiation-induced mutation is $S_1 = \exp(-\gamma D - \delta D^2)$. Hence, the probability that a cell is mutated due to radiation is $S_2 = 1 - \exp(-\gamma D - \delta D^2)$. For low frequency effects (mutations arising from an initial population is low) this is approximated as $S_3 = (\gamma D + \delta D^2)$. Therefore, the total effect of radiation known as the excess relative risk (ERR) is equal to the product of the two probabilities S and S_3 given as

$$ERR = (\gamma D + \delta D^2)\exp(-\alpha D - \beta D^2),$$

where γ and δ are the coefficients of the linear and quadratic terms for radiation induced initiation, α and β are the coefficients of the linear and quadratic terms for radiation induced inactivation. The exponential term corresponds to the cell survival and the term

$(\gamma D+\delta D^2)$ gives a small probability that a normal cell becomes mutated and thus becomes pre-malignant. The factor $\exp(-\alpha D - \beta D^2)$ is the standard linear quadratic estimate of cell survival which is the probability that a cell is not inactivated by the dose (i.e. is still capable of generating its lineage). In the case of a fractionated regimen, the excess relative risk (ERR) becomes:

$$ERR = \left(\gamma D + \frac{\delta D^2}{K}\right) \exp\left(-\alpha D - \frac{\beta D^2}{K}\right),$$

where K is the number of fractions.

Figure 3.3 displays a plot of dose against ERR. It is clearly evident that at higher doses, the predicted ERR becomes small (and zero at very high doses) which is not observed clinically, showing a clear discrepancy with the available second cancer data.

This model is validated using the atomic bomb cancer incidence data and also with recent second cancer data. It has been found that there is lot of inconsistency at higher doses, for example, breast cancer and lung cancer risks do not decrease with increasing dose (from $3 - 40$Gy). Fractionation effects are included by multiplying the quadratic term by $1/K$. As seen in Figure 3.3 there is a decrease in risk at high doses which contradicts with the recent second cancer data. This is due to the fact that the formalism takes into account the balance between inactivation and initiation effects. Inference from this contradiction is that proliferation of normal tissue is assumed to occur for acute (at the end of radiation) and protracted exposures (in between the fractions and after the last dose). Hence, one has to incorporate cellular repopulation effects along with initiation and inactivation factors.

Several authors [60]-[61], [67] have extended this model to include heterogeneous dose distribution to estimate the excess relative risk. This is carried out by acquiring the differential DVH from the treatment planning system, to obtain individual risk estimates. If (d_i, v_i) represent dose and volume received by the ith voxel $(1 \leq i \leq N)$, then ERR is

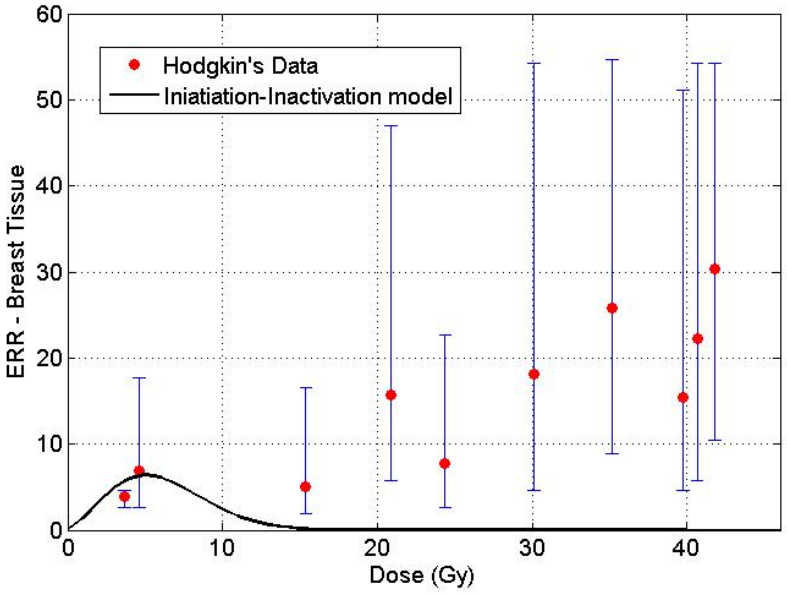

Figure 3.3: ERR-Breast tissue vs. dose using Inactivation-Initiation model (data points extracted from [15]). Parameters: $\alpha = 0.15(\text{Gy}^{-1})$, $\beta = 0.02(\text{Gy}^{-2})$, $\gamma = 0.98(\text{Gy}^{-1})$, $\delta = 0.70(\text{Gy}^{-2})$.

then given by:

$$\text{Effect}(d_i) = \left(\gamma d_i + \frac{\delta d_i^2}{K}\right) \exp\left(-\alpha d_i - \frac{\beta d_i^2}{K}\right),$$

Then the total effect for all the voxels is given by:

$$\text{Total Effect} = \frac{\sum_i v(i)\text{Effect}(d_i)}{\sum_i v_i},$$

and the ERR is then

$$ERR = \text{Total Effect} \times B \tag{3.4}$$

where B is the proportionality factor that depends on attained age, exposure age, gender and other demographic variables.

3.3.3 Initiation-Inactivation-Proliferation model

As discussed in the previous section, one of the major disadvantages of the initiation-inactivation formalism is the observed decrease in ERR at intermediate and high doses. The inconsistencies with the available clinical data are due to the fact that the formalism does not take into account the proliferation effects of radiation-induced mutated cells.

Several authors have tried to incorporate the repopulation effects to estimate radiation-induced second cancer risks [53], [62]-[63] during the fractionated treatment. These biologically motivated mathematical models incorporate detailed mechanisms, namely, cellular inactivation, initiation and proliferation. Authors in [62]-[63] developed a mathematical model based on two-point mutational process, i.e. normal cells get initiated to pre-malignant cells due to radiation which then transform to a malignant cell. Additionally, they assumed that radiation inactivates both normal and pre-malignant cell, which is compensated by cellular proliferation. They also incorporated tissue effects by assuming no proliferation under complete impairment, and repopulation resumes in unimpaired tissue. They showed that at higher doses (> 10 Gy), the predicted cancer incidence was consistent with the available clinical data. Lindsay and Weldon demonstrated the importance of the proliferation component in addition to initiation and inactivation components.

Another mathematical framework that refined the above suggested model was carried out by Sachs and Brenner [53]. This model was developed to include various fractionated protocols used in current clinical practice. One of the main advantages of this framework is that it has a smaller number of fitting parameters. This framework was validated with the epidemiological data on secondary breast and lung cancers post Hodgkin's Lymphoma disease.

The IIP model described in [53] attempts to track the number of radiation induced

pre-malignant stem cells at the end of the treatment. It tries to capture three distinct biological components: inactivation (cell killing due to ionizing radiation), initiation (radiation induced normal cell mutation), and proliferation (repopulation of cells during and after treatment). The organ specific second cancer excess relative risk (ERR) due to ionizing radiation is assumed to follow Equation (3.2).

Suppose $n(t)$ and $m(t)$ denote the number of normal and pre-malignant stem cells at time t. Following are the assumptions in their model:

- Radiation induced pre-malignant cells are defined as those cells that have the potential to transform into malignant cells,
- Radiation increases the number of normal stem cells that become pre-malignant (PM) cells,
- Repopulation of critical structures stem cells (both normal and radiation induced pre-malignant) begins when treatment starts and continues between fractions in the treatment regimen and also at the end of treatment.
- Homeostasis regulation of tissue is considered (and this is a valid assumption because the critical structure is healthy tissue) until the pre-malignant cells reach a steady state number N after the treatment,
- Long time scale post irradiation is not considered, and dose response curve is assumed to not have any effect on the longer time scale after irradiation,
- The proportionality factor in Equation (3.2) depends on demographic factors, gender, age, etc of the patient.

Figure 3.4 displays a caricature of the IIP framework. Let the number of fractionations

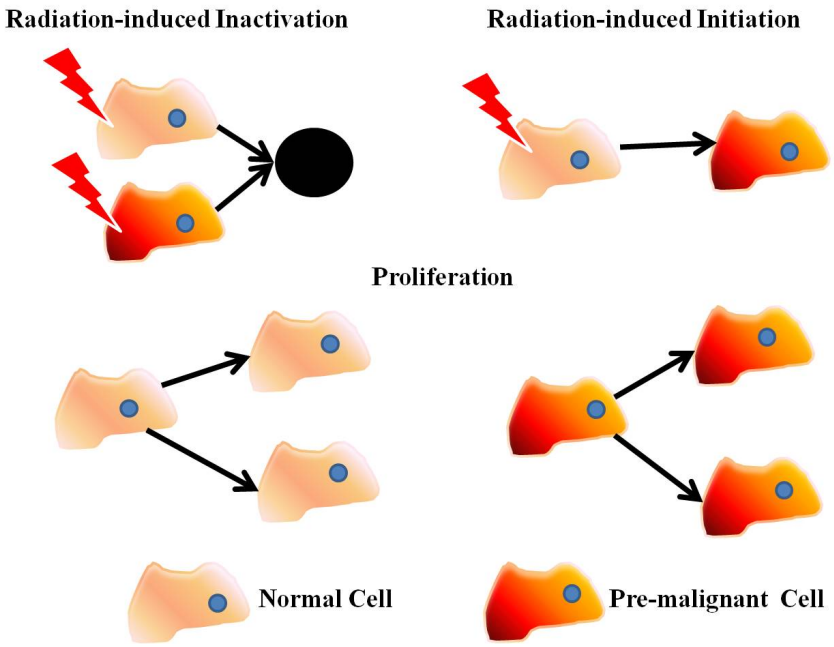

Figure 3.4: Caricature of IIP formalism: radiation induced cell inactivation, initiation and proliferation of both normal and pre-malignant cells.

be K and the mean dose per fraction be d for the whole organ, so that the total dose is given by $D = Kd$. T denotes the time between any two fractions, which is assumed to be constant.

We let n^-, m^- and n^+, m^+ denote the number of normal and pre-malignant cells just before a dose fraction and immediately after the dose fraction respectively. Suppose $k = 1, 2, \ldots, K$, then the surviving fraction of cells (S) due to dose d is given by (ignoring the quadratic term),

$$S = \exp(-\alpha d) \tag{3.5}$$

where $\alpha(\mathrm{Gy}^{-1})$ is the cellular radio-sensitivity parameter. The fraction of normal stem

cells that are not initiated as pre-malignant cells in a given fraction is given by

$$P = \exp(-\gamma d) \approx 1 - \gamma d \tag{3.6}$$

where $\gamma(\mathrm{Gy}^{-1})$ is the mutation induction parameter. The number of normal and pre-malignant cells that survive the kth dose fraction are,

$$\begin{aligned} n^{+}(k) &= SPn^{-}(k), \\ m^{+}(k) &= S\left[m^{-}(k) + (1-P)n^{-}(k)\right] \end{aligned} \tag{3.7}$$

The first term in the above equation can be interpreted as the surviving fraction of initiated cells from the previous dose fraction. And, the second factor represents the number of normal cells that are initiated from the previous dose fraction. Therefore, the number of pre-malignant cells immediately after the kth dose fraction is the sum of the two terms. Clearly, the above equation depends on the number of pre-malignant cells just before administration of the kth dose fraction. Due to homeostatic regulation of tissue, we assume that the repopulation mechanism of normal and pre-malignant cells during and after radiation follows a logistic growth model, where λ and $r\lambda$ are the repopulation rates of normal cells and pre-malignant cells, respectively. The repopulation of normal cells follows a logistic growth equation given by

$$\frac{dn}{dt} = \lambda n\left(1 - \frac{n}{N}\right), \ \ \lambda > 0 \tag{3.8}$$

where, N is the steady state number in the critical structure and λ is the rate at which the normal cells repopulate. This can be interpreted as the increase in the number of normal cells due to homeostasis regulation of tissue. The factor $\lambda\left(1 - \frac{n}{N}\right)$ can be understood as the per cell growth rate of normal cells.

The repopulation mechanism of pre-malignant cells also follows the same logistic growth pattern as that of the normal stem cell compartment, except that the per cell growth rate

term differs by a constant factor r,

$$\frac{dm}{dt} = r\lambda m\left(1-\frac{n}{N}\right), \quad r>0 \tag{3.9}$$

where, $r\lambda$ is the repopulation rate of pre-malignant cells. The solutions of Equations (3.8)-(3.9) can be used to model the repopulation mechanism between any two fractions and after the last dose fraction. Therefore, the repopulation mechanism for surviving normal cells is given by

$$n^{-}(k+1) = \frac{N}{\left[1-\exp^{-\lambda T}\left(1-\frac{N}{n^{+}(k)}\right)\right]} \tag{3.10}$$

and, the growth kinetics of pre-malignant cells is given by

$$m^{-}(k+1) = m^{+}(k)\left[\frac{n^{-}(k+1)}{n^{+}(k)}\right]^{r} \tag{3.11}$$

The number of pre-malignant cells after the last dose and until the normal cells have reached their steady state number N is given by

$$M = m^{+}(K)\left(\frac{N}{n^{+}(K)}\right)^{r}. \tag{3.12}$$

Solving the above set of discrete equations with initial conditions $n^{-}(1)=N$ and $m^{-}(1)=0$ numerically, we obtain the yield of pre-malignant cells at the end of the treatment, and until the repopulation of normal cells reaches its steady state. Figure 3.5 displays a plot of the yield of pre-malignant cells against time (days).

A total dose of 40 Gy is administered to the healthy tissue during radiotherapy treatment. Each fraction in this fractionated regimen produces several radiation-induced PM cells in the system. These cells proliferate in between fractions increasing their number in the tissue. Intuitively, there is a competition occurring between two biological mechanisms: proliferation of PM cells and cell killing of both normal and PM cells. Although

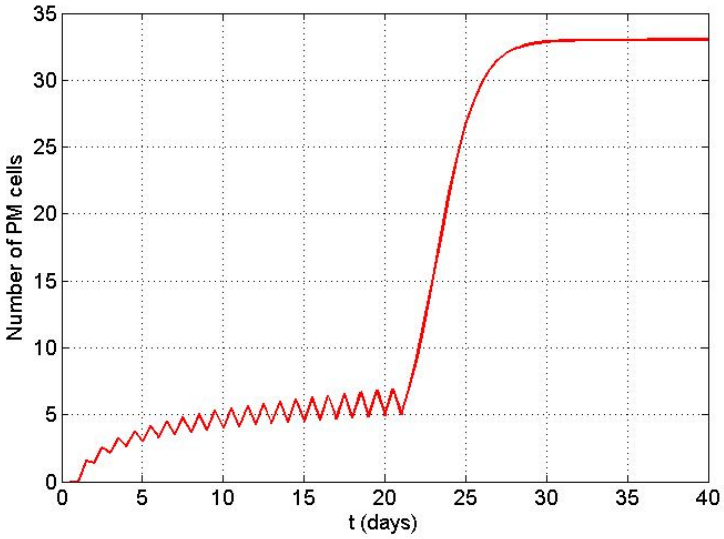

Figure 3.5: Number of pre-malignant cells vs. time. Parameters: $\alpha = 0.18(\text{Gy}^{-1})$, $\gamma = 10^{-6}(\text{Gy}^{-1})$, $\lambda = 0.4\,(1/\text{day})$, $r = 0.96$, $D = 40$ Gy, $K = 20$. (reproduced from [53])

radiation induces cell kill in both normal and PM cells, thereby decreasing the number of normal cells that are at risk becoming PM. However, the increase in the yield of PM cells is compensated for through the repopulation mechanism during and at the end of the treatment. The IIP model developed by Sachs et al. [53] is validated on epidemiological data of secondary breast cancer risks, which is displayed in 3.6.

The model fit was carried out using the relative proliferation potential of PM cells r to be equal to 0.76 [53]). Solid line in the plot denotes theoretical risk prediction by the IIP formalism. Data points are taken from the clinical studies of secondary breast cancers in HL cancer survivors. The model is very sensitive to relative proliferative potential of PM cells, and when $r = 1$ the corresponding risk grows linearly. When $r > 1$, the model over estimates the cancer incidence even at intermediate doses. The model fits well with the current clinical data under the assumption that the growth advantage is conferred on the

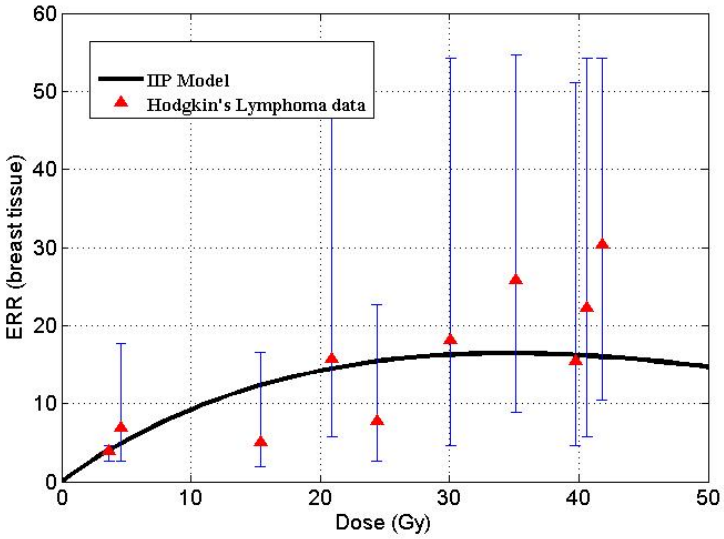

Figure 3.6: ERR breast tissue vs. Dose (error bards denote the confidence intervals). Parameters: $\alpha = 0.18(\mathrm{Gy}^{-1})$, $\gamma = 10^{-6}(\mathrm{Gy}^{-1})$, $\lambda = 0.4\,(1/\mathrm{day})$, $r = 0.76$, $K = 20$, $B = 1.2$. (reproduced from [53])

radiation initiated PM cells during the recovery period post irradiation. It should also be noted that radiation initiated PM cells have a growth disadvantage during the treatment (which is one of the differences with the classical clonal expansion models).

A single estimate for a specific cohort can either over estimate or under estimate the risks due to anatomical differences in patients. This motivated Hodgson et al. [68] to study risk estimates for individual patients, which can provide better insights into risks induced by current protocols. If V is the total irradiated volume and (d_i, v_i) are points from the differential DVH, then the ERR using the IIP formalism is given by:

$$\mathrm{ERR} = \frac{1}{V}\sum_i ERR(d_i)v_i,$$

This extended model of incorporating differential DVH into the IIP framework has been

validated for Mantle radiation therapy.

3.4 Short summary

In this chapter, we presented various mathematical formalisms used to estimate radiation-induced secondary cancer risks. The disadvantages of initiation-inactivation formalism is pointed out and the improvements to this model by Sachs et al. [53] is also discussed. The importance of heterogeneous DVH is discussed for individualized estimates in a given cohort. This chapter forms the fundamental basis for various extensions and modifications in the subsequent chapters of this thesis.

Chapter 4

Radiation Quality and Second Cancer Risks

In chapters 4-6 we discuss several extensions to the IIP formalism. There have been several scientific advancements in radiotherapy techniques (including photon, proton and ion therapies), thus it is very important to investigate the effects of various particles on secondary cancer risks. In the first section, we present the effect of radiation quality on second cancer risks. In the second section, we discuss the effect of combination of treatments and discuss the importance of treatment sequencing in the context of secondary cancers. Finally, we investigate an efficient treatment regimen that can maximize tumor control, increase disease free survival and at the same time reduce second cancer risks. It should be noted that all of these extensions are of paramount importance from the point of view of clinical investigations and practice.

4.1 Introduction

In the last few decades, external beam radiation therapy has become one of the primary therapeutic interventions in many cancer treatments, resulting in an overall increase in the survival rate of cancer patients. One of the primary reasons is due to better dose conformity and delivery to the target volumes. As discussed in previous chapters, radiation therapy acts as a double-edged sword leading to drastic side-effects, one of them being secondary malignant neoplasms in cancer survivors. Several investigations by epidemiologists have indicated that the mortality rate of Hodgkin's Lymphoma (HL) survivors is high post irradiation [69]. Abundant evidence from cohort and case control studies have also implied that there is an increased risk of second malignancies with young HL survivors [69]-[76]. Recently, several clinical studies have characterized the risk of various subtypes of second malignancies, indicating that there is a high incidence rate of breast cancer among young HL survivors [77]-[78]. The latency is typically between 10 to 20 years from the time of primary treatment. Hence, a challenge in radiation treatment planning is to prescribe an efficient treatment regimen to minimize the dose distribution to normal tissue, without hindering the treatment to the tumor volume.

There are several forms of radiotherapy treatment in current clinical practice. The most common form uses high energy photon beams, these include 3D conformal radiotherapy (3DCRT) and intensity modulated radiotherapy (IMRT). Other forms of treatment include proton therapy (PT) and heavy ion therapy (HIT). Although PT is being used to treat several tumors (such as prostate cancer), it is still in the experimental stages (and the same holds true for HIT also). There are several forms in which a healthy tissue can receive unwanted doses. During the process of tumor volume and critical structures delineation, organs of interest are found to be partially within the radiation field (located in the plateau

region of the Bragg peak and correspond to the high dose region) or adjacent region (which corresponds to the intermediate dose region). Healthy tissues that are proximal to the primary target volume receive doses anywhere between $0.1-50$ Gy. Another source arises from the linear accelerator, in the form of scattered and the leakage radiation, that contributes to low level doses (< 0.1 Gy) [79]-[80]. Conventional treatment techniques that use photons deposit energy as they traverse tissue, leading to radio-biological damage of healthy tissue. Several experimental studies have been carried out to quantify the secondary particle exposures resulting from the production of protons, neutrons and alpha particles which also contribute to the overall risks of secondary cancers [79]-[83]. However, in the current work, we neglect the contributions of risks from photo-nuclear reactions within the patient body, along with the contribution from the neutron dose that is generated from the head of the linear accelerator.

On the other hand, protons or heavy ions have different dosimetric features compared to photons. These particles are usually accelerated to specific energies depending on the tumor depth. Heavily charged particles enter the body with low dose (causing no significant damage), but deposit the bulk of their energy as the particle slows down at the end of its path. This phenomenon can be clearly understood in terms of the Bragg peak [79], [84], [85] as discussed in Chapter 2. One of the major advantages of PT and HIT over photons is their physical characteristics. Maximum energy deposition occurs precisely at the tumor volume and the dose is delivered with much greater precision, resulting in a higher tumor control probability. Thus, the total energy deposited in the patient associated with photon therapy is often larger when compared to proton or heavy ion therapy [79], [84], [85]. Therefore, PT and HIT deliver a lower integral dose to the healthy tissue compared to photons, leading to minimal side effects and lower induction of second cancer risks [79]-[80]. Several studies report that neutron production (due to nuclear reactions) also contributes significantly to

the overall secondary cancer risks [86]-[91]. There are ways to shield neutron radiation from the linear accelerator, the production of neutrons within the patient cannot be avoided. Neutron production also depends on the type of biological material in the beam path as well as the beam design, leading to large variations in neutron doses [80]. However, to simplify our mathematical framework, we ignore the risk contributions associated with neutrons (both from the linear accelerator and within the patient). In this work, we use a biologically motivated mathematical model (the IIP formalism), described in the previous chapter.

There has been a great deal of modeling and experimental studies that have investigated the dependence of particle type on the radio-sensitivity parameters. These investigations have highlighted that particle type has a predominant effect on the radio-biological parameters as well as on the mutation induction frequency of normal cells to pre-malignant state. In particular, these studies have outlined the effect of mono-energetic protons, alpha particles and heavy ions (for example, carbon and neon), radiation-induced cellular effects [93]-[103]. These effects include (but are not limited to) cellular inactivation and initiation parameters. Since second cancer risks are a function of cellular inactivation and mutation induction, it is therefore important to study the effect of various radiation quality features such as linear energy transfer (LET) of a charged particle or an ion.

Numerous experimental and clinical studies have suggested that LET has a predominant impact on the cellular radio-sensitivity [93]-[103]. In the current work, we consider dose averaged LET, which is defined as,

$$\langle LET \rangle = \frac{\sum_i LET_i D_i}{\sum_i D_i} \tag{4.1}$$

In the above equation i refers to dosimetric particle tracks and D_i denotes the corresponding dose. Radiation induced biological damage (both inactivation and initiation)

highly depends on the microscopic track structure. In the present work, we use clinically relevant LET values in our modeling efforts. Clinical proton beam energies can lie anywhere between $70-250$ MeV [93]-[94]. For the maximum therapeutic proton energy of 250 MeV, the corresponding value of LET is $0.39\,(\mathrm{keV}/\mu\mathrm{m})$; and LET increases to $83\,(\mathrm{keV}/\mu\mathrm{m})$ for 0.08 MeV. In addition, authors in [93]-[94] have shown that the maximum value of the dose averaged LET is around $30\,(\mathrm{keV}/\mu\mathrm{m})$. Variations in clinically relevant dose averaged LET for heavy ions are still unclear, thus we consider a range of LET values for this scenario.

Another radio-biological parameter required to model radiation induced second cancer risks is the mutation induction rate. Several systematic experimental investigations have characterized the mutation induction frequency for several LET values and for various doses [95]-[97]. These studies have indicated that mutation frequency is dependent on fractionation. Hence, it is important to include the effects of mutation rate on dose per fraction, and this may have an impact on the overall radiation induced cancer risk.

All proximal organs located in the vicinity of the primary radiation field are referred to as the in-field volume, which receive doses from $0.1-50$ Gy. The out-of-field volume is the region that receives very low doses (less than 0.1 Gy) due to leakage or scattered radiation. The main objective of this study is to model the risks of second malignancies by including the dependence of radio-biological parameters and mutation rates on LET for protons and heavy ions, for organs located in the in-field region. We also compare photon therapy against PT for various dose regimes. In order to carry out a fair comparison between protons and photons, photon dose is converted to Cobalt Gray Equivalent (CGE) using proton $RBE = 1.1$ [79]-[80]. The proximal organs around the target volume are located in the plateau region of the Bragg peak, with an LET of 4-10 $(\mathrm{keV}/\mu\mathrm{m})$. We evaluate the second cancer risks in the plateau region of the Bragg peak for high and intermediate dose regions outside the primary treatment volume. It is known that a proton beam with

energy 1.2 MeV, and an alpha particle with energy 30.5 MeV have the same LET value of 23 (keV/μm). Goodhead et al. [102] and Belli et al. [103], used specific beam energies 1.44 and 1.23 MeV for protons, and 35.7, 30.5 MeV for alpha particles in order to obtain the same LET. Belli et al. [103] obtained similar LET of 20.3 (keV/μm) and 23 (keV/μm) for protons and alpha particles. Finally, we try to compare the second cancer risks induced by protons and alpha particles of different energies, given that they both have the same LET as reported by Goodhead et al. [102] and Belli et al. [103].

We model radiation induced second cancer risks for the critical structure, i.e. breast tissue in Hodgkins Lymphoma survivors. In general, the dose and volume distribution in the critical structure will differ depending on the treatment approach (either using photons or particles). Although it is not the case clinically, to simplify the mathematical framework we assume that the organ of interest receives a uniform dose distribution irrespective of the treatment approach. Also, our model (as mentioned earlier) does not take into account the risk induced by stray radiation (either from the linear accelerator, or, from neutrons) outside the radiation field, and also the dose delivered by the plateau (of the Bragg peak) within the radiation field. Our mathematical framework models the risks within the irradiated volume that received high to intermediate doses only.

4.2 Mathematical framework

4.2.1 Dependence of radio-biological parameters on LET

We extend the IIP formalism to incorporate the dependency of LET on the radio-biological parameters. In particular, the cellular inactivation parameter α is described by two models in the literature. The non-linear model was suggested by Chen and Ahmad [100], where

the α dependency of proton LET using V79 cells (in vitro) was fit using least squares method, which is given by:

$$\alpha_P = \alpha_0 + \frac{1 - \exp(-\theta_1 \, (\mathrm{LET})^2)}{\theta_2 \, (\mathrm{LET})} \tag{4.2}$$

where $\alpha_0 = 0.1 \ (1/\mathrm{Gy})$, $\theta_1 = 0.0013 \, (\mathrm{keV}/\mu\mathrm{m})^{-2}$ and $\theta_2 = 0.045 \, \mathrm{Gy}(\mathrm{keV}/\mu\mathrm{m})^{-1}$ [100]. Figure 4.1 displays the dependence of α_P on proton LET. It should be noted that as LET increases, α_P increases, reaching a maximum value at an $LET \sim 30.5 \, (\mathrm{keV}/\mu\mathrm{m})$, and decreases for high values of LET. We are interested in relevant values of LET (below $30 \, \mathrm{keV}/\mu\mathrm{m}$) in a clinical setting. Hence, we assume a linear dependence for α_P as follows:

$$\alpha_P = \alpha_{P_1} + \alpha_{P_2} \, (\mathrm{LET}) \tag{4.3}$$

where $\alpha_{P_1} = \alpha_0 = 0.1 \, (1/\mathrm{Gy})$ and $\alpha_{P_2} = \theta_1/\theta_2 \sim 0.02 \, \mathrm{Gy}(\mathrm{keV}/\mu\mathrm{m})^{-1}$ [93]-[94].

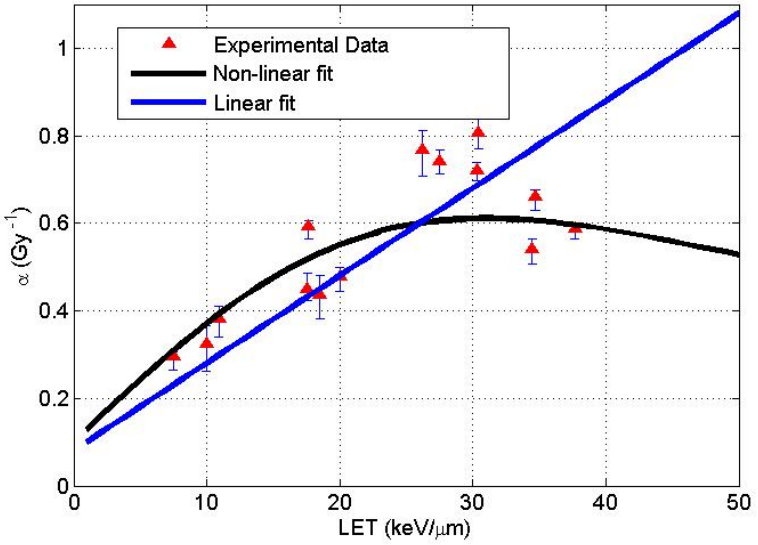

Figure 4.1: Linear and non-linear dependence of α_P on LET.

In a similar way for heavy ions, we assume that α_i is a linear function of LET [98], (and neglecting the decrease in α for high values of LET:

$$\alpha_i = \alpha_{i_1} + \alpha_{i_2} \, LET \tag{4.4}$$

where $\alpha_{i_1} = 0.03044\,(1/\mathrm{Gy})$ and $\alpha_{i_2} = 0.01091\,(\mathrm{Gy\ keV}/\mu\mathrm{m})^{-1}$ are for Carbon ion and $\alpha_{i_1} = 0.00327\,(1/\mathrm{Gy})$ and $\alpha_{i_2} = 0.007395\,\mathrm{Gy}(\mathrm{keV}/\mu\mathrm{m})^{-1}$ for Neon ion, obtained from linear fits. Figure 4.2 displays the dependence of α_i on the Carbon and Neon LET, where the experimental data is taken from [101]. Finally, for photons, we assume that $\alpha = 0.18$ $(1/\mathrm{Gy})$, independent on LET value [53].

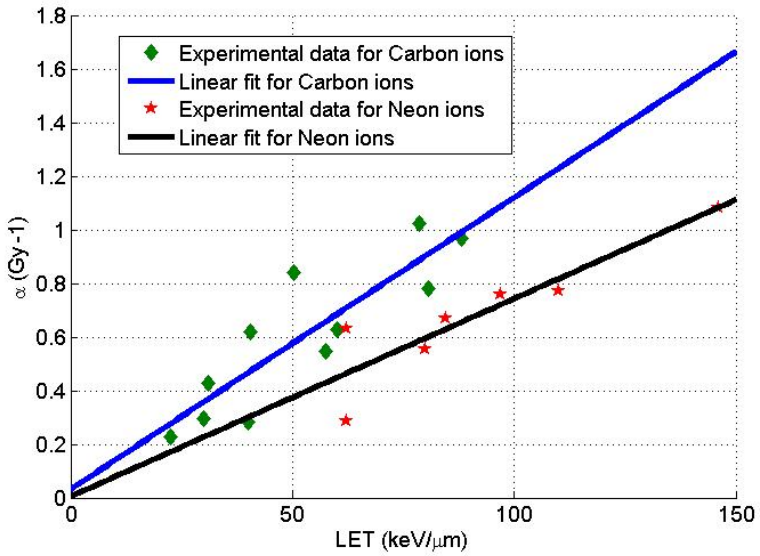

Figure 4.2: Linear dependence of α_i on LET.

4.2.2 Dependence of mutation rate on LET

Many experimental studies have pointed to the importance of understanding the effects of radiation quality on several biological factors. These works have demonstrated that the microscopic track structure properties might have subtle effects on the biological properties of a cell. One of the most important biological factors is the radiation induced mutation frequency, which plays a predominant role in carcinogenesis and, particularly, in the initiation of radiation-induced secondary malignancies post irradiation. Using the conventional definition, mutation frequency is defined to be the fraction of mutated cells within a given cell culture. The mutation rate is defined as the rate at which mutations occur in a given time period. Since, the relationship between mutation frequency and mutation rate is highly complex and non-trivial, we make the simplifying and plausible assumption that the mutation frequency is proportional to the mutation rate. This assumption is based on the experimental evidence of HPRT (hypoxanthine-guanine phosphoribosyltransferase) locus induction. Experimentalists have investigated the effects of mono-energetic proton beams on Chinese hamster V79 cells, and reported the results for the mutation frequency. We extracted the experimental data related to HPRT locus mutation induction due to protons, as well as for ions (both for Carbon and Neon), and performed a linear fit for various LET values. Figure 4.3 shows the mutation frequency induced by protons for various LET values ($7, 11, 20, 30.5\,\mathrm{keV}/\mu\mathrm{m}$) and different doses. We consider slope of these linear fits to be a function of LET. The mutation induction parameter is then given by $\gamma = \gamma_0(\mathrm{LET})$, where γ_0 is a proportionality constant with units $((\mathrm{Gy\ keV}/\mu\mathrm{m})^{-1})$. Figure 4.4 displays the mutation frequency induced by Carbon and Neon ions of approximately the same LET, i.e. $68\,\mathrm{keV}/\mu\mathrm{m}$ for Carbon ion and $63\,\mathrm{keV}/\mu\mathrm{m}$ for Neon ion.

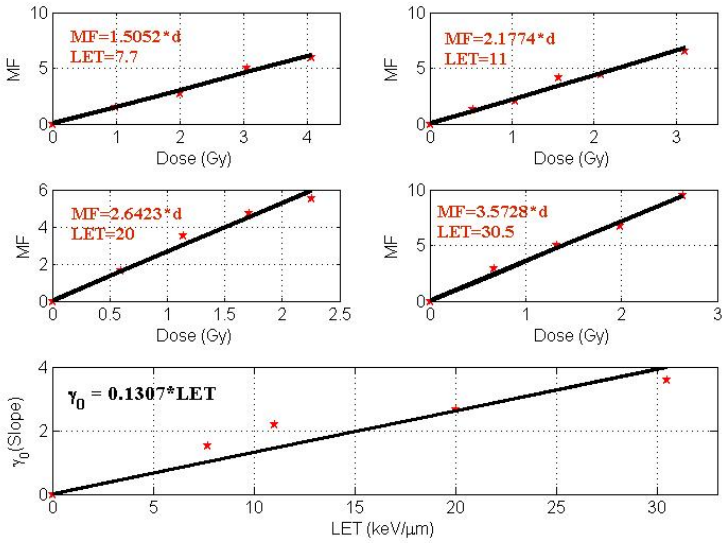

Figure 4.3: HPRT mutation induction due to mono-energetic proton beams. Points denote the experimental data [97] and black line resembles a linear fit for the (mutation frequency (MF) $\times 10^{-5}$).

4.3 Results

We consider the critical structure to be the breast tissue since secondary breast cancer is one the leading causes of death in Lymphoma survivors. We apply the extended IIP formalism presented in the previous section, and estimate the ERR for proton and heavy ions using the appropriate LET values in the clinically relevant dose regions.

4.3.1 Comparing Photons and Protons

Firstly, we present results comparing protons and photons. Several authors have reported variations in mutation induction frequency with respect to dose for X-rays. The exper-

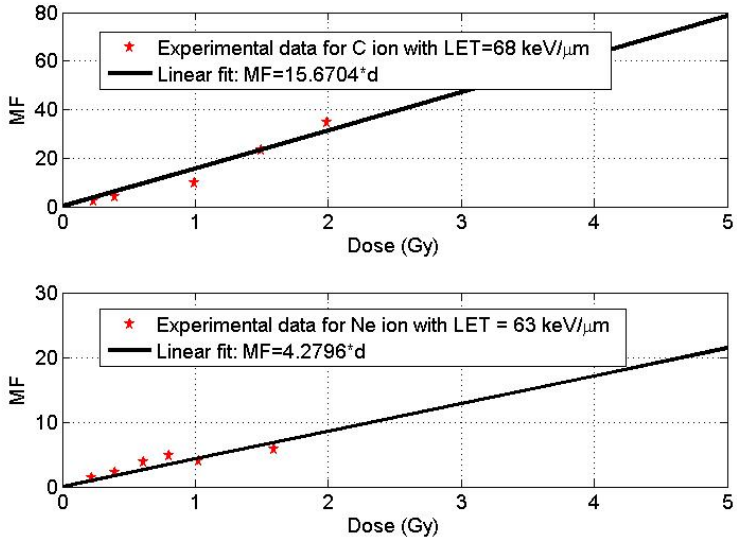

Figure 4.4: HPRT mutation induction due to mono-energetic ions. Points denote the experimental data [99] and black line resembles a linear fit for the (mutation frequency (MF) $\times 10^{-5}$).

imental data can be fitted using a linear function, with the proportionality constant set to 0.1. Since the clinical LET value for protons in the plateau region of the Bragg peak is around 4-10 (keV/μ m), we chose the proton LET of 4 (keV/μm) and compared the secondary cancer risks against photons. In the case of protons, the cell killing parameter equivalent to that of the cell killing parameter for photons, was obtained for a proton with LET value 4 (keV/μm) and the proportionality constant for the mutation rate is chosen to be 0.185. The ERR values were calculated for photons and protons for various dose regimes. These results are presented in Figure 4.5. The red curve in the figure is the ERR for a proton LET of 4 (keV/μm) and the blue curve denotes the ERR due to photons. In order to have a fair comparison, we converted the photon dose to cobalt gray equivalent

(CGE) by multiplying with the RBE of protons (taken to be 1.1). The plot clearly indicates that the ERR for protons is lower than that of photons, which is also something observed clinically. More experimental investigations are necessary in order to understand the influence of LET on α for various treatment field options with various energies in the low dose region for clinically relevant values of LET in the plateau region.

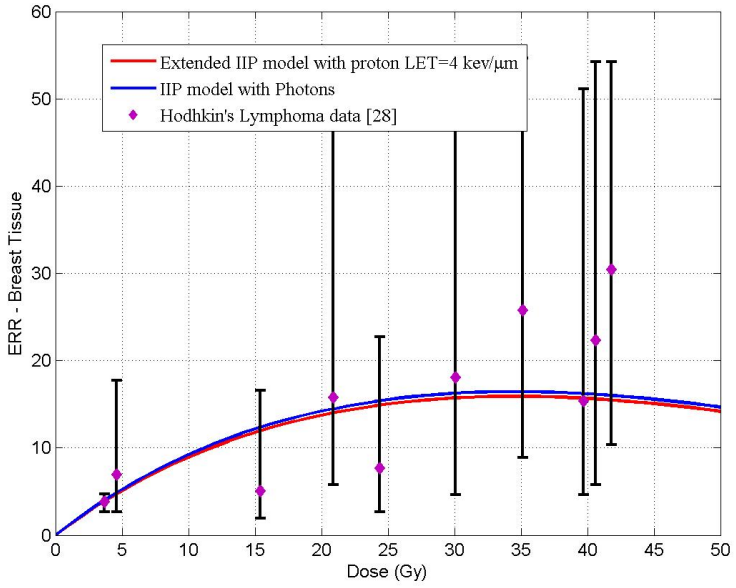

Figure 4.5: Comparison between protons and photons. Parameters: $\lambda = 0.4(1/\text{day})$,$r = 0.76$, $\gamma_{proton} = \gamma_0 = 0.189 \times 0.1307\,\mu\text{m}(\text{keVGy})^{-1} \times \text{LET} \times 10^{-5}$. For photons $\gamma_{photon} = \gamma_0$ is assumed to be proportional to dose. In this plot, we chose LET$= 4\,\text{keV}/\mu\text{m}$ so that cell inactivation parameter is the same for both protons and photons, $N = 10^6$, $B = 1.2$.

4.3.2 ERR vs. Proton LET and ERR vs. Proton Dose

The results on the dependence of proton LET on ERR are now discussed. Figure 4.6 is a plot of the ERR over a clinical range of LET values for various doses. The nonlinearity is seen for low LET protons and for all dose regimes. There are several critical points at which the curves intersect, indicating that the ERR values are equal at those critical points. It is quite interesting to note that cellular initiation and proliferation mechanisms (of pre-malignant cells) dominate at different critical points resulting in identical ERR values. The ERR is small and almost linear for low LET and low doses (which is also observed epidemiologically), compared to low LET and high doses. However, the risk increases as LET increases and decreases for high LET values, which is 10 (KeV/μm).

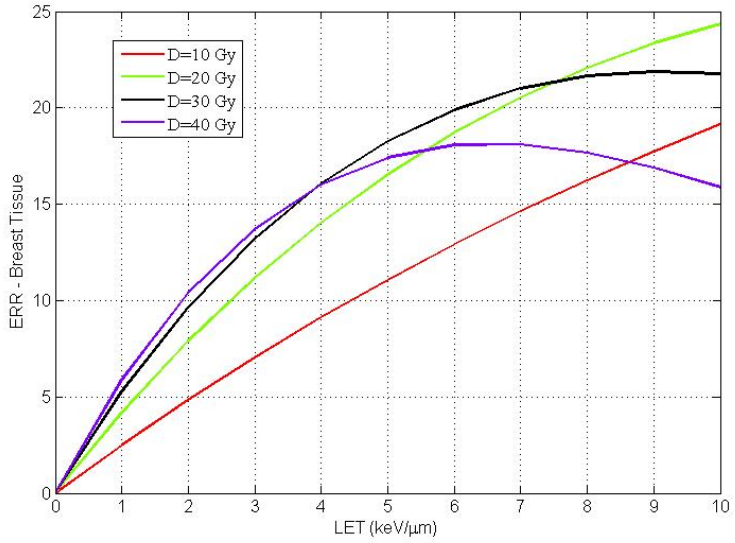

Figure 4.6: ERR vs. Proton LET. Parameters: $\lambda = 0.4(1/\text{day})$,$r = 0.76$, α_P is linear model, $\gamma_{proton} = \gamma_0 = 0.189 \times 0.1307\,\mu\text{m}(\text{keVGy})^{-1} \times \text{LET} \times 10^{-5}$, $N = 10^6$, $B = 1.2$.

Figure 4.7 is a plot of the ERR for a range of LET values in the plateau region of the

Bragg peak for various doses with conventional fractionated therapy (2 Gy/fraction). The cell killing parameter is estimated using the linear model. The non-linearity is seen in the high dose region from 30 Gy. The ERR is small for low LET and low doses, compared to that for low LET and high doses. In the low and intermediate dose region, mutation induction is dominated by the cell killing mechanism, due to which we observe higher risk for high LET compared to low LET values. In the high dose region, for high LET, the cell killing mechanism dominates over the mutation induction, as a result the risk decreases and tends to zero. However in the low LET region, mutation induction over takes the cell killing at high doses leading to high risks. We notice that the ERR approaches zero for all values of LET after a threshold dose, indicating a reduction in cancer risk which is due to cell over kill.

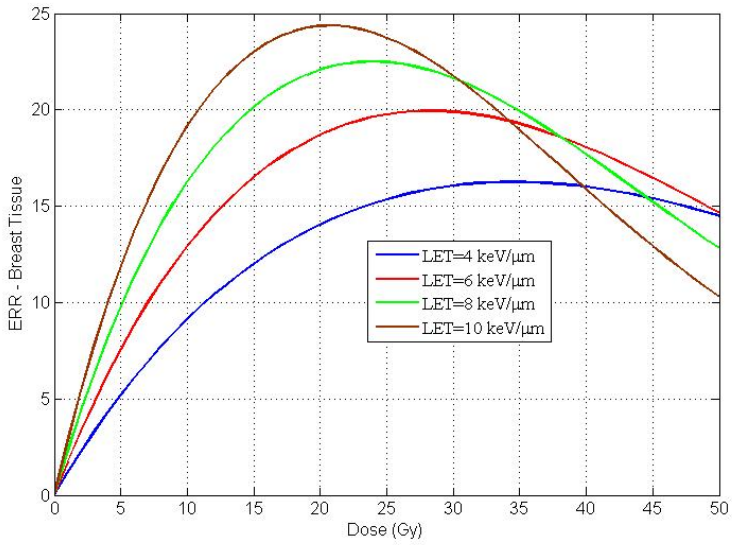

Figure 4.7: ERR vs. Proton LET. Parameters: $\lambda = 0.4(1/\text{day})$,$r = 0.76$, α_P is linear model, $\gamma_{proton} = \gamma_0 = 0.189 \times 0.1307\,\mu\text{m}(\text{keVGy})^{-1} \times \text{LET} \times 10^{-5}$, $N = 10^6$, $B = 1.2$.

4.3.3 Protons vs. Alpha particles

There have been several (in-vitro) experimental investigations carried out comparing protons and alpha particles of similar LET. Although a physical comparison between protons and alpha particles is well established in the physics literature, the comparisons of various biological end points of these two particles at the same LET value have not been addressed. Although this is considered to be an artefact, and not observed clinically, we still wish to model this biological phenomenon due to an increase in alpha particle therapy to treat micro metastases. Pioneering work in this domain was carried out by Belli et al. [104] and Folkard et al. [105], and they reported that low energy protons have higher biological effectiveness compared to alpha particles of a similar LET value. From a physical point of view, it is clear macroscopically that for the same value of LET, the number of ionizations and the energy deposition per unit path length is the same. However, it has been shown that the cellular inactivation and initiation rates for the two charged particles differ using mono-energetic beams on V79 cell lines [102]-[103]. The authors showed that protons have a higher biological effectiveness compared to alpha particles, due to their dense concentration of ionization clusters in the LET range of 20-25 (keV/μ m). The cell killing parameters for protons and alpha particles with 20.3 (keV/μm) are reported to be 0.42 (1/Gy) and 0.25 (1/Gy) respectively; and for an LET of 23 (keV//mu m) , cell kill parameter values are given by 0.30 (1/Gy) and 0.21 (1/Gy), respectively [102]. The mutation induction frequencies for both protons and alpha particles are quite different, which is presented in Figure 4.8.

We clearly observe that protons are more effective at inducing mutations compared to alpha particles with the same energy. We have used the extended IIP model to estimate the second cancer risks caused by protons and alpha particles at the same LET, and the

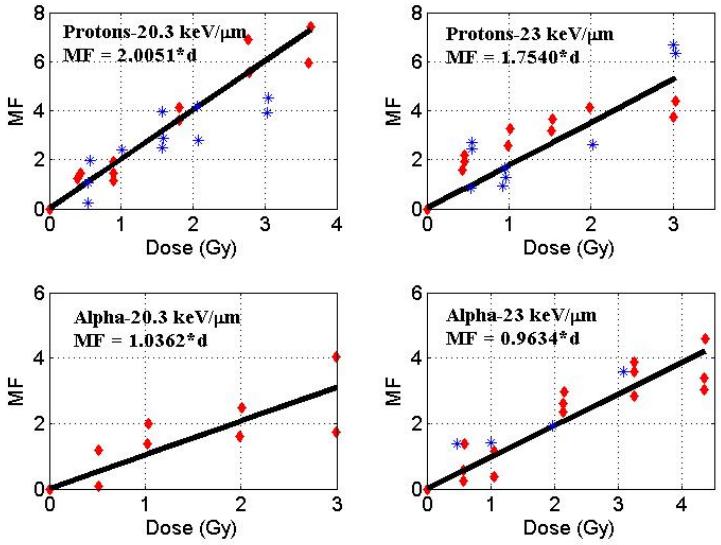

Figure 4.8: HPRT mutation induction due to mono-energetic proton beams. Points denote the experimental data [39] and black line resembles a linear fit for the (mutation frequency (MF) $\times 10^{-5}$).

results are presented in Figure 4.9. We notice that protons have an associated higher risk compared to alpha particles in the lower dose region. As discussed in [102]-[103], protons have higher biological effectiveness compared to alpha particles as a result of which we observe that protons have a higher mutation induction frequency than alpha particles in the low dose region. Mutations dominate the cell kill mechanism in the lower dose region, resulting in higher risks. As we move into the high dose region, we observe a lower risk for protons due to a higher cell kill rate compared to alpha particles (i.e., cell inactivation dominates mutation induction in the higher dose region). In addition, it is interesting to note that the risk is almost equal at 22 Gy and 35 Gy at LET of 20.3 (keV/μm) and 23 (keV/μm) respectively.

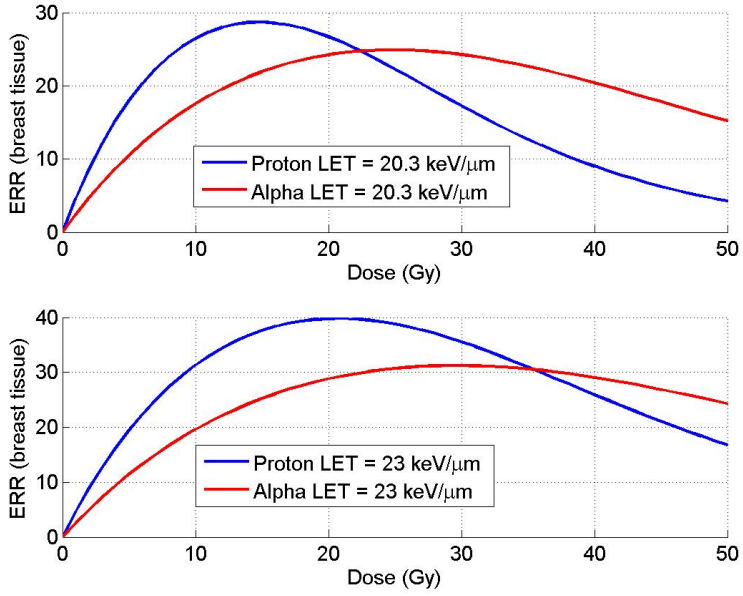

Figure 4.9: ERR vs. Dose. Parameters: $\lambda = 0.4(1/\text{day}), r = 0.76$, $\alpha_{P20.3} = 0.42(1/\text{Gy})$, $\alpha_{P23} = 0.30(1/\text{Gy})$, $\alpha_{A20.3} = 0.25(1/\text{Gy})$, $\alpha_{A23} = 0.21(1/\text{Gy})$, $N = 10^6$, $B = 1.2$, γ_0 is taken from Figure 4.8.

4.3.4 Heavy Ion ERR vs. Dose

This section presents results for ERR for heavy ions in various dose regimes. Figure 4.10 is a plot of ERR against dose for a fixed LET for Carbon and Neon ions. Although the LET's are close enough for both ions, we observe different behaviors. In the lower dose region, the cancer risk due to Carbon ions is higher compared to Neon ions. A possible reason might be due to the fact that there is a higher mutation induction rate by Carbon ions compared to Neon ions. In the high dose region and at high LETs, heavy ions have a highly dense ionization track structure. This is because mutation induction is dominated by cellular inactivation, which in turn can result in decreased ERR values. It is interesting

to note that the cancer risk for the two ions is equal at approximately 18 (Gy).

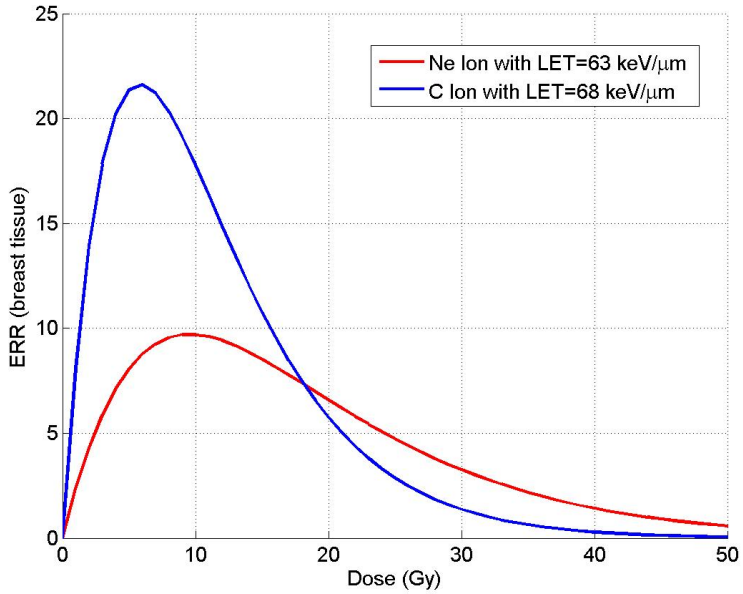

Figure 4.10: Heavy Ion ERR vs. Dose. Parameters: $\lambda = 0.4(1/\text{day}), r = 0.76$, α_i is linear model, $\gamma_C = \gamma_0 = 0.01 \times 15.6704\,\mu\text{m}(\text{keVGy})^{-1} \times \text{LET} \times 10^{-5}$, $\gamma_{Ne} = \gamma_0 = 0.01 \times 4.2796\,\mu\text{m}(\text{keVGy})^{-1} \times \text{LET} \times 10^{-5}$, $N = 10^6$, $B = 1.2$.

4.4 Short Summary

The present work is an effort to investigate the *ERR* associated with various radiation therapies PT and HIT (particularly, Carbon and Neon ions). We have extended the existing IIP model to include the effects of LET on the radio-biological parameter α and also on the mutation frequency γ. Non-linear behavior was observed for low LET protons in all dose regions. Another interesting observation is that the ERR is small and almost linear

for low LET and low doses, compared to low LET and high doses. Protons and alpha particles of varying energies that have the same value of LET are compared for various dose regions. We notice that, in the lower dose region, proton therapy has higher associated risks compared with alpha particles. However, in the high dose region, we observe smaller risks for protons compared to alpha particles. Additionally, we also estimated the ERR's for Carbon and Neon ions. Since heavy ions have a highly dense ionization track structure at high LET's, we notice that radiation induced mutation is dominated by the cell kill mechanism, resulting in a decreased cancer risk. Overall, this study demonstrates the importance of including LET dependence in the estimation of second cancer risk.

Although, our theoretical risk predictions are noticeably high, the biological end points should be tested experimentally for multiple and mixed treatment fields. Our findings demonstrate the need to include radiation quality features into radiotherapy treatment planning as one of the optimization parameters to model second cancer risks.

Chapter 5

Effect of Treatment Strategies on Second Cancer Risks

5.1 Introduction

Clinically, the combination of various treatment strategies might result in a greater tumor control, however, there are several long term complications associated with these treatment strategies. One of the major challenges in clinical oncology is to prescribe an efficient treatment regimen that can maximize tumor control and minimize second cancer risks. As discussed in the previous chapter, radiotherapy (RT) is one of the leading causes of secondary malignancies in most cancer survivors.

Several clinical studies have shown that chemotherapy may also act as a potential carcinogen. Chemotherapeutic agents which are used to kill tumor cells also interact with the systemic healthy tissue of the target volume (along with other organs of the body), leading to potential radio-biological damage. Clinical studies suggests that chemotherapy

is one of the leading causes of secondary leukemia within 5 years following primary treatment. The combination of chemotherapy and radiotherapy is considered to be the primary therapeutic interventions in current clinical practice (which includes pediatric oncology also). Numerous case control and cohort studies have suggested that various combinations of chemotherapy and radiation therapy (CRT) might reduce, or, increase the risks of secondary malignancies. CRT therapeutic strategy can be of several types, namely, adjuvant therapy (chemotherapy administered after radiation), neo-adjuvant therapy (radiation administered after chemotherapy) or concurrent therapy (chemotherapy and radiation given simultaneously). For a given CRT modality, it has been observed that there is a possible increased risk associated with a few drugs, for example doxorubicin, and other alkylating agents such as procarbazine. It should also be noted that these risks may be tissue specific. For example, alkylating agents appear to increase the risk of a subsequent gastrointestinal cancer, but decrease the risk of breast cancer by affecting endogenous estrogen production [106]-[107].

Looking at the number of cancer patients receiving CRT modality, it is therefore important to understand the potential complications associated with CRT treatment. At the same time, it is necessary to consider the potential effects of sequencing a treatment strategy in order to maximize tumor control with minimal damage to the healthy tissue.

Several mathematical models have been discussed in the previous chapters to estimate radiation-induced second cancer risks at clinically relevant doses. Similarly, numerous mathematical approaches have been proposed in the literature to address the cell kill effects of chemotherapy drugs [108]-[109]. However, these models have not been applied to evaluate the potential risk of secondary malignancies. In this present work, we intend to extend the IIP formalism described in chapter 4. Our main goal is to develop a generalized mathematical model that incorporates CRT treatment modality, and to address key ques-

tions related to sequencing of treatments that can potentially minimize second cancer risks. It should be noted that, our model ignores the pharmacodynamics feature of chemotherapeutic agents, and their interaction with ionizing radiation. More importantly, we do not consider the potential physiological effect of these treatments on organs outside the irradiated volume that might have downstream effects on second cancer risk (for example, ovarian function). We discuss the effect of dosage and scheduling of chemotherapy (single) and as a combined modality (with RT) on second cancer risks. In addition, we also discuss an efficient sequence that may potentially reduce CRT induced secondary cancer risks.

5.2 Mathematical Formalism

We rewrite the discrete model of IIP formalism in terms of it's continuous version. Let $n(t)$ and $m(t)$ represent the number of normal and pre-malignant stem cells at time t. Although this framework can be extended to include stem cell hierarchy in normal tissue, but in order to reduce the number of parameters, we simplified the model to a single phenotype. Then, the continuous model that tracks the evolution of normal and pre-malignant cells is given by the following coupled equations:

$$\begin{aligned}
\frac{dn}{dt} &= \lambda n\left(1-\frac{n}{N}\right) - \alpha_R d\sum_{i=1}^{K} f_\tau(t-iT)n - \gamma_R d\sum_{i=1}^{K} f_\tau(t-iT)n \\
\frac{dm}{dt} &= r\lambda n\left(1-\frac{n}{N}\right) - \alpha_R d\sum_{i=1}^{K} f_\tau(t-iT)m + \gamma_R d\sum_{i=1}^{K} f_\tau(t-iT)n
\end{aligned} \tag{5.1}$$

where the first term on the right hand side denotes the proliferation mechanism; the second term denotes cellular inactivation due to dose rate and the third term denotes radiation induced cell initiation due to the dose rate. Here, $f_\tau(t)$ is a step function that represents the fractionated dose d administered in K fractions. It should be noted that, all three terms

are active during the irradiation time, and only the first term is active during between fractions, and after the last dose till the normal cell reaches steady state.

We apply a similar continuous version to understand the effect of chemotherapy on the risks of secondary malignancies. The effect of the chemotherapy dosage is done by replacing $d\sum_{i=1}^{K} f_\tau(t-iT)n$ (that denotes a unit step function of fractionated radiotherapy regimen) with $D_C \sum_{i=1}^{K_C} H(t-t_i)\exp(-\alpha_d t)$ where K_C denotes the number of chemotherapy cycles and $H(t-t_i)$ is the Heaviside function. Table 5.1 consists of all the parameters and their interpretation.

Parameters	**Interpretation**
$K_R = 20$	Number of fractions
K_C	Number of chemotherapy cycles
D_C	Total chemotherapy dosage
$\lambda(1/\text{day})$	Proliferation rate of normal cells
$r\lambda(1/\text{day})$	Proliferation rate of PM cells
$\gamma_R(1/\text{Gy})$	Radiation-induced mutation
$\gamma_C(1/\text{Dose})$	Chemotherapy-induced mutation
$\alpha_R(1/\text{Gy})$	Radiation-induced cell kill
$\alpha_C(1/\text{Dose})= 1$	Chemotherapy-induced cell kill
$\alpha_d(1/\text{day})$	Decay rate

Table 5.1: Summary of parameters and interpretations

5.3 Results

In the current study, we consider the critical structure to be one of organs which are proximal to the tumor volume. As before, we assume that second cancer risk ERR is proportional to the number of pre-malignant cells.

Before we proceed with results, we would like to establish the equivalence of the discrete and continuous versions that model radiation-induced cancer risk. Figure 5.1 displays a plot for a fixed radiation dose of 40 Gy given in 20 fractions.

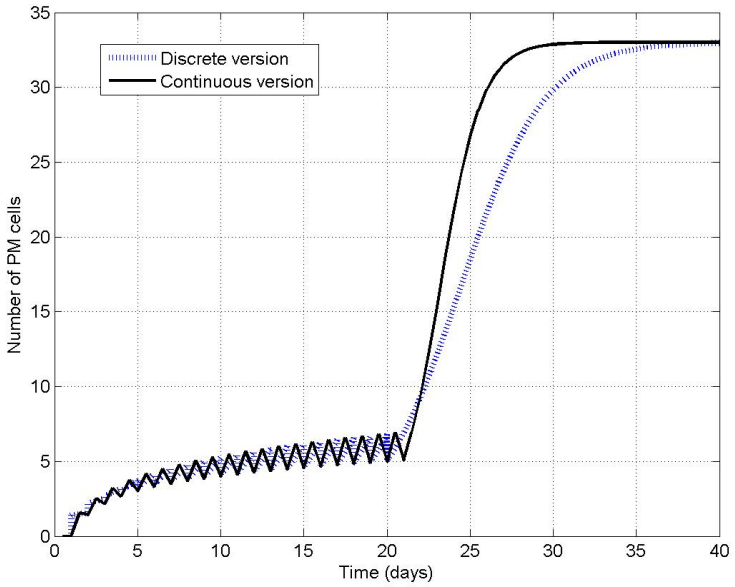

Figure 5.1: Equivalence of discrete and continuous models. Parameters: $D = 40\,\text{Gy}$, $K_R = 20$, $\lambda = 0.4(\text{per day})$, $r = 0.96$, $\gamma_R = 10^{-6}(\text{per Gy})$, $\tau = 30\,\text{minutes}$.

We assume that the irradiation time is approximately 30 minutes per fraction. The number of pre-malignant cells obtained from discrete and continuous models is approx-

imately 33.001 and 32.96 respectively, resulting in almost identical risk values. For the rest of the work, we apply the IIP continuous formalism to estimate second cancer risks induced by chemotherapy and also for the combination of various treatment strategies.

5.3.1 Effect of Chemotherapy only

In this section, we present results related to the effect of chemotherapy (alone) on the number of pre-malignant cells. For the purpose of fair comparison, we normalize all the curves (with respect to the dosage). And, D_C has the unit of drug concentration, and $\gamma_C D_C$ is dimensionless in this work.

The effect of the strength of cell kill due to chemotherapy alone is presented in Figure 5.2. We chose various levels of cell kill and normalized the dose with a proportionality

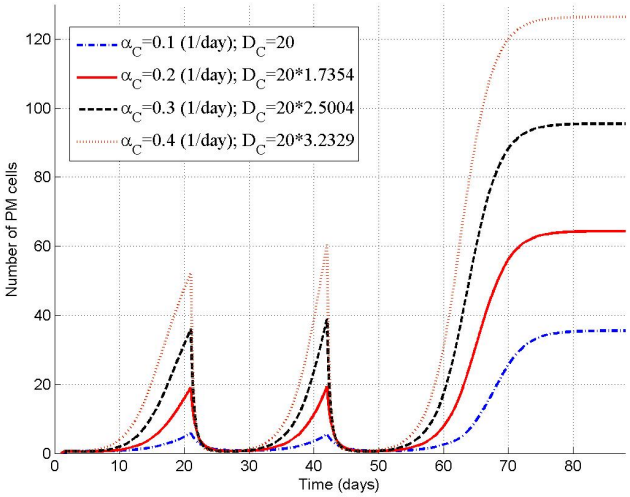

Figure 5.2: Effect of chemotherapy (only) cell killing on PM cells. Parameters: $\lambda = 0.4$, $r = 0.76$, $D = 40\,\text{Gy}$, $K_C = 3$, $\alpha_C = 1$, $\gamma_C = 10^{-6}$, Length of each cycle $= 21\,\text{days}$.

factor. Three chemotherapy cycles with 21 days per cycle are administered to the patient. It is quite interesting to see that, as we increase the cell kill term the number of pre-malignant cells increases. One of the main reasons for this scenario is because of the decrease in the number of normal cells in the system, which take time to repopulate back to their steady state number. As normal cells take time reach their steady state, the initiated pre-malignant cells proliferate during the same time period, and increase in number. The variations in cell kill rates are tissue-specific, denoted by α_C. For example, clinical investigations have shown that breast tissue cell kill rate is less than that for bone marrow. From our analysis, smaller cell kill rates result in lower second cancer risks when compared to higher cell kill rates. Smaller values of α_d can be interpreted as chemotherapy drugs having small cell kill rates, whereas larger values correspond to high cell kill rates. Therefore, chemotherapy induced second cancer risks strongly depend on particular tissues under consideration.

The effect of the number of chemotherapy cycles on pre-malignant cells is shown in Figure 5.3. For this purpose, we fix the strength of the cell kill and the length of each cycle to be 21 days. Intuitively, we expect an increase in the number of pre-malignant cells as the number of chemotherapy cycles is increased (Figure 5.3). It is interesting to note that there is a jump in the number of pre-malignant cells from the 3rd to 4th cycle, and this stays almost constant for the rest of the cycles. The number of pre-malignant cells against the length of chemotherapy cycle is displayed in Figure 5.4. It is clearly seen that as we increase the cycle length, the number of pre-malignant cells increases leading to an increase in the second cancer risks, which is expected intuitively. Hence, as the length of the chemotherapy cycles increase, the proliferation mechanism of the resultant increase in mutated cells leads to an increase in the corresponding second cancer risks. From our analysis (see Figures 5.3 and 5.4), we suggest that an optimal strategy would be

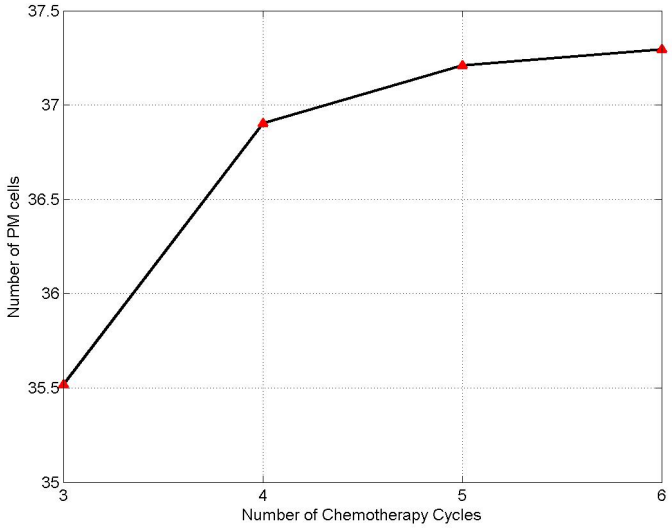

Figure 5.3: Effect of chemotherapy (only) cycle number. Parameters: $\lambda = 0.4$, $r = 0.76$, $D = 40\,\text{Gy}$, $\gamma_C = 10^{-6}$, $\alpha_C = 1$, Length of each cycle $= 21\,\text{days}$.

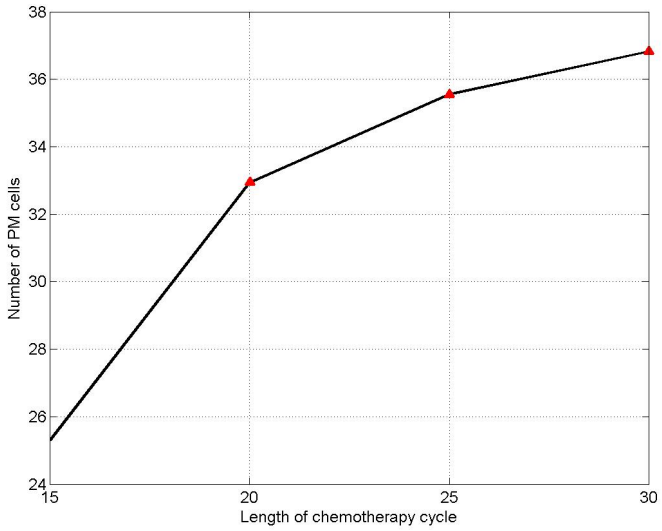

Figure 5.4: Effect of chemotherapy (only) cycle length. Parameters: $\lambda = 0.4$(per day), $r = 0.76$, $D = 40\,\text{Gy}$, $K_C = 3$, $\alpha_C = 1$, $\gamma_C = 10^{-6}$.

to administer a chemotherapy regimen with minimum number of cycles along with shorter chemotherapy cycle length. This result is consistent with the clinical observation that the chemotherapy agent etoposide increases the risk of chemotherapy-induced leukemia when given over a longer time frame [110]-[111].

Clinical investigations have supported the fact that several chemotherapeutic agents can potentially increase or decrease second cancer risks. For example, a chemotherapy agent doxorubicin is known to increases the risk of secondary leukemia [112], and an alkylating agent procarbazine is known to have tissue-specific effects, which also increases stomach cancer risk. There have been several experimental studies on tissue specific mutation rates on human cell lines [113]-[114]. One of the important findings from [114] is that the number of mutations in self renewing tissues positively correlates with the diagnosis age of the patient. Therefore, the mutation rate depends on the particular tissue which correlates with the patient age. We now explore the effect of chemotherapy-induced mutation rates on second cancer risks. As the mutation rate increases, the number of pre-malignant cells increase, leading to an increase in second cancer risks, which is displayed in 5.5. Therefore, our model shows that chemotherapy induced second cancer risks are tissue-specific, due to the variations in the mutation rates.

5.3.2 Combination of treatments

There are several combined modality treatments that are used in current clinical practice, namely, adjuvant therapy (chemotherapy followed by radiation), neo-adjuvant therapy (radiation followed by chemotherapy) and concurrent therapy (chemotherapy and radiation administered simultaneously). Figures 5.6 and 5.7 present plots of a comparison of adjuvant and neo-adjuvant therapies for two scenarios: $\gamma_R < \gamma_C$ and $\gamma_R > \gamma_C$ respectively.

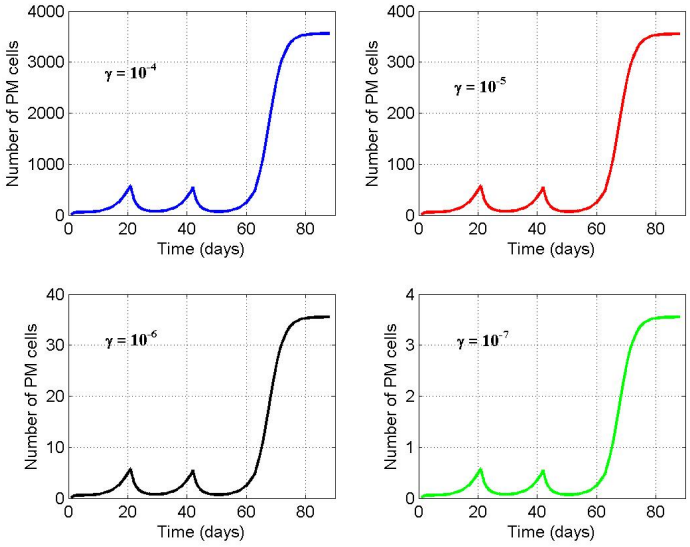

Figure 5.5: Effect of chemotherapy induced mutation rate on PM cells. Parameters: $\lambda = 0.4$, $r = 0.76$, $D = 40\,\text{Gy}$, $K_C = 3$, Length of each cycle= 21, days, $\alpha_C = 1$, $D_C = 20$.

When $\gamma_R < \gamma_C$ (see Figure 5.6), the number of pre-malignant cells at the end of adjuvant treatment is smaller in number compared to those after neo-adjuvant therapy. For the neo-adjuvant therapy case, although the number of pre-malignant cells induced by radiation therapy is small in number, they increase in number during the administration of chemotherapy due to a higher mutation induction rate. Since the chemotherapy induced mutation rate is high compared to the radiation induced mutation rate, our results suggest that radiation therapy should be followed by chemotherapy, in order to reduce the risks of second cancer. In a similar manner, when $\gamma_R > \gamma_C$, the number of pre-malignant cells at the end of neo-adjuvant treatment is smaller in number compared to those after adjuvant therapy. This suggests that chemotherapy should be followed by radiation therapy, in

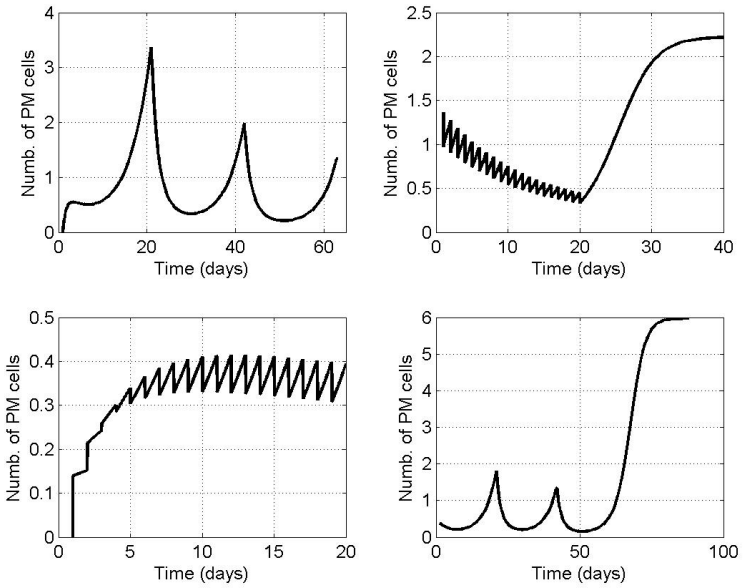

Figure 5.6: Adjuvant vs. Neo-adjuant therapies. Parameters: $\lambda = 0.4$(per day), $r = 0.76$, $K_C = 3$, Length of each cycle= 21 days, $D_C = 20$, $\gamma_C = 10^{-6}$, $D_R = 40$ Gy, $\gamma_R = 10^{-7}$ (per Gy), $K_R = 20$.

order to reduce second cancer risks. Our analysis clearly indicates that, administration of adjuvant or neo-adjuvant therapy should be administered depending on the corresponding mutation induction rates in the context of secondary malignancies.

In the case of concurrent therapy, we assume that three cycles of chemotherapy (with 21 days per cycle) are administered along with radiation therapy in any one of those cycles with equal mutation rates for both chemotherapy and radiotherapy. Figure 5.8 presents a plot of concurrent therapy, where radiation is administered in various cycles. We obtain almost the same number of pre-malignant cells, resulting in almost identical risks. This suggests that the cycle in which radiation is administered in the concurrent therapy regimen

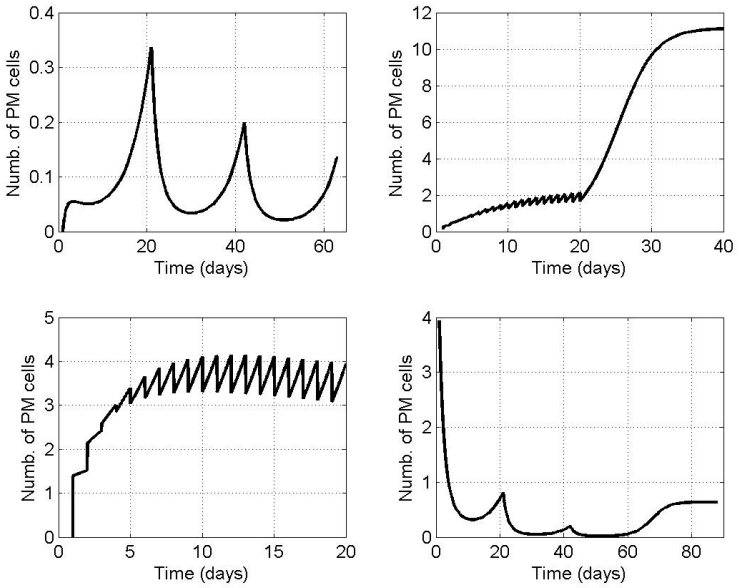

Figure 5.7: Adjuvant vs. Neo-adjuant therapies. Parameters: $\lambda = 0.4$(per day), $r = 0.76$, $K_C = 3$, Length of each cycle= 21 days, $\alpha_C = 1$, $D_C = 20$, $\gamma_C = 10^{-7}$, $D_R = 40$ Gy, $\gamma_R = 10^{-6}$ (per Gy), $K_R = 20$.

does not have a major impact on the risk when the mutation rates are equal. Figure 5.9 presents a plot for $\gamma_C < \gamma_R$ scenario. We intuitively expect that, radiation given in the first cycle of chemotherapy has smaller associated risks compared to radiation administered either in second or third cycles. Radiation-induced mutation rates are in general larger compared to chemotherapy-induced mutation rate, this implies that if radiation is given in the first cycle the number of initiated cells turn out to be small, resulting in lower risks. However, in the case of HL patients, a clinical observation is that chemotherapy shrinks the tumor size so that the irradiated volume becomes smaller (see Figure 5.9). It should be noted that, if radiation is administered in the last chemotherapy cycle, the number of pre-malignant cells increase due to the combination of chemotherapy and radiation-induced

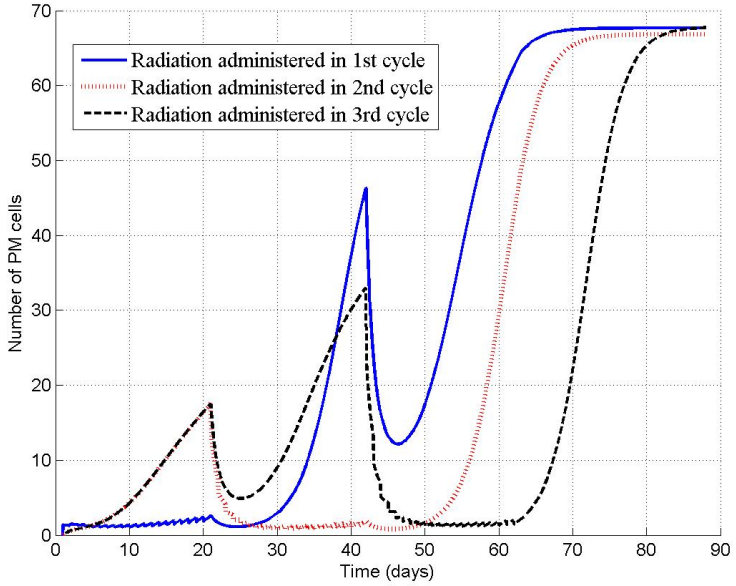

Figure 5.8: Concurrent therapy. Parameters: $\lambda = 0.4$(per day), $r = 0.76$, $K_C = 3$, $\alpha_C = 0.25$, Length of each cycle= 21 days, $\alpha_C = 1$, $D_C = 20$, $\gamma_C = 10^{-6}$, $D_R = 40$ Gy, $\gamma_R = 10^{-6}$ (per Gy), $K_R = 20$.

mutation rates. Figure 5.10 presents a plot when $\gamma_R < \gamma_C$, we observe that when radiation is given either in first or second cycle, this results in an increased risk of second cancer compared to the case when radiation is administered in the last cycle of chemotherapy. This is because, all the pre-malignant cells induced by chemotherapy get killed during the radiation (given in the third cycle), resulting in a reduction of second cancer risks.

We also compared adjuvant, neo-adjuvant and the concurrent therapies assuming equal mutation rates for both chemotherapy and radiation therapy. Results are displayed in Figure 5.11. We observe that neo-adjuvant therapy has lower associated risks compared to adjuvant and concurrent therapies (if radiation is given either in second or third cycles).

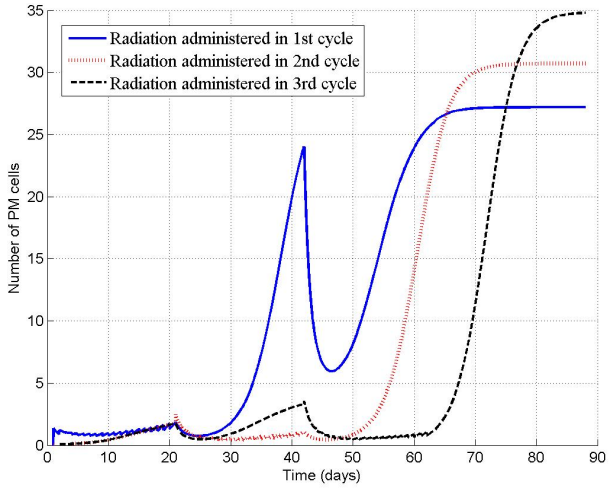

Figure 5.9: Concurrent therapy. Parameters: $\lambda = 0.4$(per day), $r = 0.76$, $K_C = 3$, Length of each cycle= 21 days, $\alpha_C = 1$, $\alpha_d = 0.25$, $D_C = 20$, $\gamma_C = 10^{-7}$, $D_R = 40$ Gy, $\gamma_R = 10^{-6}$ (per Gy), $K_R = 20$.

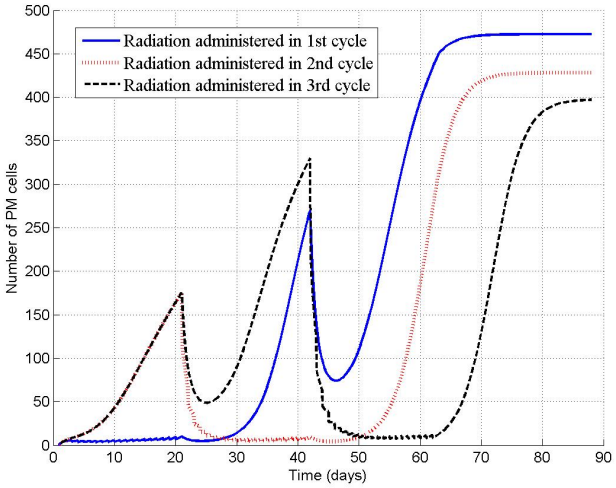

Figure 5.10: Concurrent therapy. Parameters: $\lambda = 0.4$(per day), $r = 0.76$, $K_C = 3$, Length of each cycle= 21 days, $\alpha_C = 1$, $\alpha_d = 0.25$, $D_C = 20$, $\gamma_C = 10^{-5}$, $D_R = 40$ Gy, $\gamma_R = 10^{-6}$ (per Gy), $K_R = 20$.

And, the risks associated with neo-adjuvant and concurrent (if radiation is given in the first cycle) therapies are almost the same.

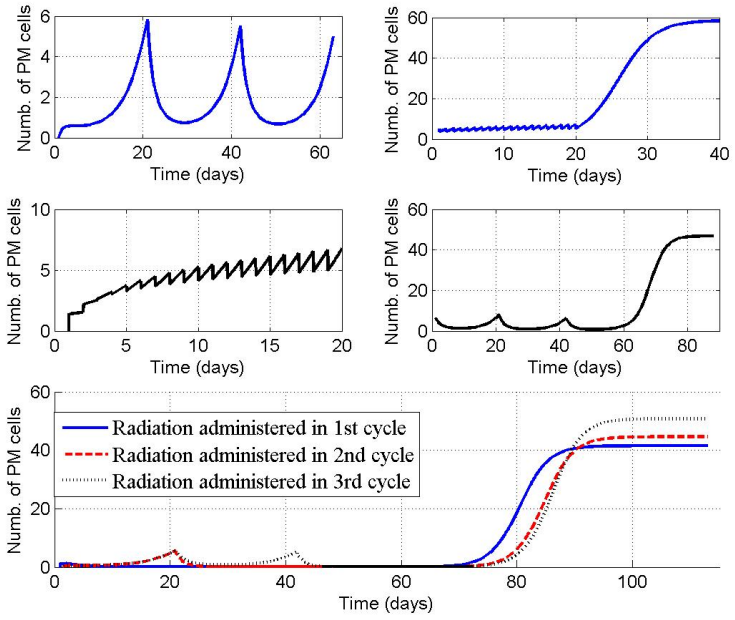

Figure 5.11: Comparison of Adjuvant, Neo-adjuvant and Concurrent therapies. Parameters: $\lambda = 0.4$(per day), $r = 0.76$, $K_C = 3$, Length of each cycle= 21 days, $\alpha_C = 1$, $\alpha_d = 0.25$, $D_C = 20$ (D_C has the unit of drug concentration, and $\gamma_C D_C$ is dimensionless), $\gamma_C = 10^{-6}$, $D_R = 40$ Gy, $\gamma_R = 10^{-6}$ (per Gy), $K_R = 20$.

5.4 Short summary

Several clinical and epidemiological studies have shown that chemotherapy and ionizing radiation are potential carcinogens for secondary malignancies. In this study, we have developed a generalized mathematical model that incorporates the effects of chemotherapy

and radiation therapy on second cancer risks. Our preliminary study demonstrates the importance of estimating second cancer induced risks for various treatment strategies, which can also be used as a tool in designing efficient sequencing of therapies that can minimize second cancer risks without hindering treatment to the gross tumor volume. Additionally, these theoretical predictions can also be used to understand the effect of dose timing on second cancer risks. More importantly, this study suggests that second cancer risks cannot be generalized for any organ of interest (or, critical structure), and are highly tissue dependent. This model can be further extended to include the pharmacodynamics of chemotherapeutic drugs and their interaction with ionizing radiation. This framework can be used to provide insight into the design of efficient therapy sequencing that can lower second cancer risks without impairing treatment to the primary tumor.

Chapter 6

Effect of Dose Escalation on Second Cancer Risks

6.1 Introduction

Clinically, it is observed most of the patients undergo radiation therapy as a primary or combined modality (namely, adjuvant, neo-adjuvant or concurrent) treatment. In all of the current radiotherapy paradigms, treatment volumes are often irradiated with a heterogeneous dose distribution (which is observed in a DVH). The probability that all clonogenic tumor cells are removed from the system immediately post-treatment is known as the tumor control probability (TCP) [115]. The therapeutic index of any treatment protocol and the efficacy of any regimen can be deduced (to some extent) from the TCP values. Although a heterogeneous dose (and volume) distribution for any treatment regimen to the tumor volume might locally control the disease to a larger extent, there are several shortcomings associated with all these protocols. As discussed in previous chapters, ion-

izing radiation acts as a double edged sword, and there are several side effects associated with radiotherapy.

These side effects can be classified based on the time scale of manifestation, i.e. side effects that appear on a shorter time scale include local irritation of skin, mucosa, or irradiation of tissues within adjacent structures. The late toxicities of radiation appear as a secondary malignancy which has (already) been discussed in previous chapters. It should be noted that several clinical studies have reported tumor recurrence or relapse within a span of 5 years, and late toxicities in the form of secondary malignancies within 5-20 years post-irradiation. These clinical investigations have been carried out on several types of tumors across a variety of treatment regimens. All these studies have indicated that tumor relapse along with radiation-induced secondary cancers are two of the leading causes of death in childhood cancer survivors.

Several pre-treatment variables such as age at diagnosis, gender, type and stage of tumor may impact tumor relapse. Also, relapse probability and time may vary depending on the treatment protocol, i.e. administration of chemotherapy alone, or radiotherapy alone, or a combined regimen (both chemotherapy and radiotherapy simultaneously). For simplicity, we consider the effect of only radiotherapy on TCP along with analysis of time to relapse. Due to recent advancements in functional imaging techniques, the biological variations in the tissue can be obtained and used to design an efficient heterogeneous dose description, in the form of dose painting. Escalating the dose to the tumor volume can be for several reasons, such as to increase tumor control probability, decrease the aggressiveness of a tumor, decrease proliferation and eliminate radio-resistant cells in the hypoxic region. This dose prescription might have an impact on the relapse time (either very long in the ideal case, or an increase in the recurrence time) depending on the radiation regimen. Moreover, introducing dose escalation will affect the risks of secondary malignancies to the critical

structures (if the same dose is received by the healthy tissue), however, the degree to which it increases these risks remains to be determined.

Additionally, several clinical and epidemiological investigations have shown that patients may face short-term relapse (within 5 years of treatment), or long-term relapse (5-10 years) post irradiation [116]. Although there is a probability of late relapse in some patients (which occurs in 5-10 years) and/or a second malignancy within 5-20 years post irradiation, clinicians have yet to determine which of these predominates, in practice. For example, a tumor relapse can occur 20 years later following initial treatment in HL patients, as reported in [116]. At the same time, it is well known that the manifestation of secondary solid tumors also occurs within 10-20 years post irradiation for HL survivors. Therefore, it is of significant importance to explore possible fractionation protocols that can maximize local control of the disease, increase disease free survival (i.e. increase in relapse/recurrence time) and reduce second cancer risks. It is therefore critical to minimize radiation dosage and schedule radiation doses such that there is minimal impairment to the primary treatment volume, a probable increase in the relapse time (or, with a long relapse time ideally), but also with the goal in mind of reducing the risk of a second cancer.

The main objective of this work is to develop a generalized mathematical formalism that can incorporate recurrence dynamics into a TCP model in conjunction with a second cancer model. This is carried out to understand the effects of dose escalation on recurrence and second cancer risks. Our simplified model also proposes an efficient radiation regimen that may provide insights to be confirmed by future clinical investigations.

6.2 Mathematical framework

The survival fraction of cells after radiation therapy is given by equation Equation (3.1). Tumor control probability (TCP) is a clinical measure used to estimate the probability to eliminate clonogenic tumor cells, and also used to compare various fractionation protocols that are used in current clinical practice. Assuming a Poisson formalism, the tumor control probability is given by:

$$TCP = \exp(-N_0 S). \tag{6.1}$$

where N_0 is the total number of clonogens in the system and S is the survival function of cells after a given acute dosage D.

Clinically, it is not always possible to eradicate all the tumor cells from the system. Biologically, there is always a small number of residual cancerous cells that are not eliminated (either they survive the effects of irradiation, or escape the irradiation itself). These remaining tumor cells clonally expand post-irradiation, to cause a relapse or recurrence of the primary tumor after a period of time. The recurrence dynamics of a tumor is developed by assuming logistic growth, with the same exponential growth parameter as in the pre-treatment phase, such that the number of cells in the system reaches a critical threshold. Let n_r be the number of residual cancerous cells at the end of the treatment. Then the relapse dynamics is given by:

$$\frac{dn_r}{dt} = \lambda n_r \left(1 - \frac{n_r}{N}\right). \tag{6.2}$$

The initial condition for the relapse dynamics framework is determined by the output from the TCP model. We then determine the time that elapses post-treatment to recurrence. We incorporate the TCP model with relapse dynamics of the tumor, and estimate the corresponding second cancer risks for various fractionation protocols. Clinically, it is

important to eliminate the cancerous cells completely (or reduce them to a possible minimum), such that recurrence is either zero, or the time for relapse is increased. Practically, this can be done by increasing the dose to the tumor volume such that the value of the TCP is near 1 with a possible increase in the recurrence time. It should be noted that at the same time, concomitant second cancer risks to the critical structures are increased (assuming the same dose is received as the tumor volume) due to the escalation of dose to the tumor. Thus radiation in this case is considered to have both positive and negative effects on the patient, i.e. increasing local control of disease and an increase in the survival time (assuming some cancer cells still remain in the system post treatment) but at the cost of an increase in the second cancer risks.

6.3 Results

It should be noted that in the results presented, the radio-sensitivity parameter β was determined to be very small, and was neglected in all computations (both for TCP and second cancer risks). Table 6.1 summarizes the protocols used in our work, and hyper fractionation is defined as 2 fractions administered on the same day, with a time interval of 6 hours between inter-fractions

We first present our investigations on TCP, recurrence and second cancer risks individually. This is done in order to explore an efficient best protocol that can increase TCP and recurrence time. We also evaluate radiation-induced second cancer risks for each of these fractionation schemes used for the TCP and recurrence models. This is carried out in order to determine the risks associated with each of these individual protocols. As previously discussed dose escalation can improve local control of disease, increase disease free survival (or, ideally result in a recurrence time longer than the remaining lifetime of the individ-

Protocol	**Fractionation Scheme**
Conventional	30 fractions with 2 Gy per fraction
Hypo-fraction	20 fractions with 3 Gy per fraction
Hyper-fraction1	20 fractions with 2 Gy per fraction ($d = \frac{2}{3}d + \frac{1}{3}d$)
Hyper-fraction2	20 fractions with 2 Gy per fraction ($d = \frac{1}{3}d + \frac{2}{3}d$)

Table 6.1: Summary of fractionation schemes

ual) and an increase in secondary malignancy risks. Dose escalation is carried out for a fixed number of fractions, or when there is an increase in the total number of fractions. In the later part, we present our results related to dose escalation which maximizes the TCP and increases recurrence time, as well as the relative change in second cancer risks. This analysis is carried out to identify various radiation regimens that can (potentially) be administered in order to minimize the occurrence of secondary malignancies.

Table 6.2 summarizes parameters that are used in our mathematical model. All radiation therapies are given 5 days per week (i.e. accounting for the weekend breaks).

6.3.1 TCP, relapse and second cancer risk calculation

The computation for the TCP was based on the mathematical model describing the dynamics of cellular proliferation within the tumor. The average number of cells in the tumor volume at any given time is modeled deterministically, and because the true number of cells is a stochastic quantity distributed around this mean, we may approximate the probability of tumor control as the Poisson probability that there are zero clonogens remaining in the

Parameters	Interpretation	Values
N_0	Initial number of cells	10^6
t_{rad} (minutes)	Irradiation time	15
α (per Gy)	LQ model parameter	0.3
t_{double} (days)	Doubling time of cancer cells	80
λ (per day)	Proliferation rate of normal cells	0.4
$r\lambda$ (per day)	Proliferation rate of PM cells	0.75
γ (per Gy)	Radiation-induced mutation	10^{-6}

Table 6.2: Summary of model parameters, interpretations and values [53], [181]

system, with a given average number of cells, given by Equation 6.1, which is the Poisson probability that, given there are $N(t)$ cells on average, at time t, the tumor volume has zero cancerous cells remaining in the system.

Relapse of a primary tumor is defined to have occurred after a critical number of cells, 10^6, has been reached. We then determine the time point at which the tumor population level reaches a threshold of 99% of 10^6 (as it only approaches the limit of logistic growth, i.e. reaching 10^6 asymptotically). We then regard this as the time post-treatment to recurrence. Figure 6.1 displays TCP and recurrence curves for various fractionation protocols used in current clinical practice for a fixed dosage of radiation.

From Figure 6.1, we observe that the TCP curves perform best for conventional and hypo-fractionation protocols, which are followed by the hyper-fractionation1 regimen, and the hyper-fractionation2 protocol which performed poorly. This poor effect is a clear indicator in the relapse curves presented in the same plot. The differences in TCP are reflected in the recurrence curves, which show that starting from different initial values for the residual

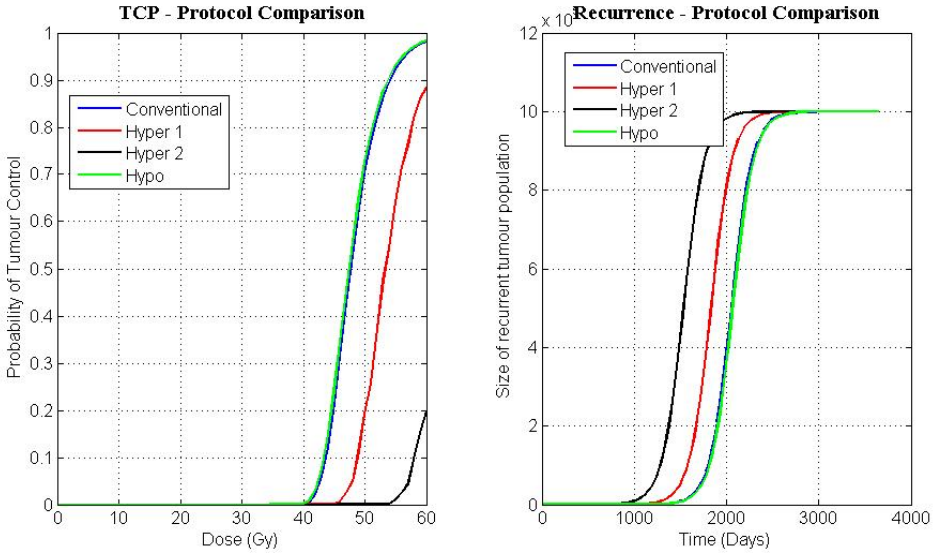

Figure 6.1: TCP vs. dose and Relapse vs. dose for various fractionation protocols (It should be noted that blue and green curves are overlapping).

tumor cells post irradiation leads to different times to reach a logistic growth threshold of nearly 10^6 cells, indicating a relapse. From this plot, it is clear that time for relapse is longer for a fractionation regimen whose TCP value ends closer to 1, simply because there is a higher probability that there are few cancerous cells remaining within the tumor volume at the end of the treatment.

We now consider the effect of fractionation on second cancer risks. For this, we assume the critical structure to be one of the healthy organs irradiated in the neighborhood of the tumor volume. As discussed in previous chapters, we assume that ERR is proportional to the number of radiation induced pre-malignant cells remaining at the end of the treatment. Figure 6.2 displays a plot comaparing various fractionation regimens, between dose and the corresponding number of pre-malignant cells. It should be noted that the numbers of

pre-malignant cells are calculated under the assumption that the healthy tissue receives 100% of the dose received by the tumor.

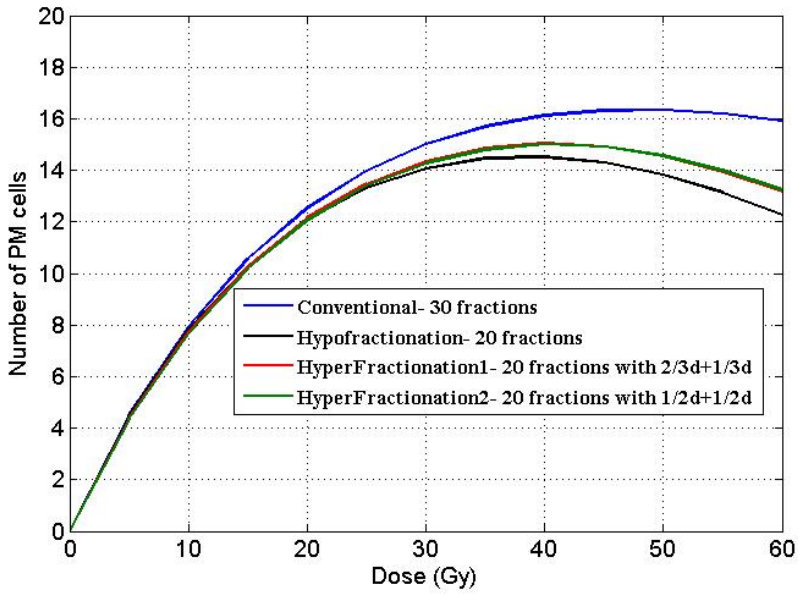

Figure 6.2: Effect of various fractionation protocols on the yield of pre-malignant cells.

From our calculations, we deduce that hypo-fractionation is a more theoretically efficient protocol in the reduction of second cancer risks, which is consistent with clinical results [117] (in the treatment of sarcoma and carcinoma). Intuitively, due to the high dose per fraction, from a biological point of view the cell kill mechanism dominates the proliferation term, leading to a reduction in the risks of second cancer compared to the other regimens. For large doses, the cell kill mechanism dominates mutation induction, which causes a decline in the second cancer risks. Therefore, from the perspective of reduction in second cancer risks, we observe that hypo-fractionation is a theoretically more efficient regimen when compared to the other schemes, (notably even conventional radiotherapy). Although there are several ongoing discussions on the effect of fractionation on

second cancer risks, these theoretical risk predictions cannot be generalized for every critical structure, or tissue type. Recent clinical studies have reported that hypo-fractionation appears to be a better option to treat carcinoma of the prostate [118] and breast cancer in elderly patients [119]. More recently, Schneider [117] found that hypo-fractionated therapy reduces second cancer risks for carcinomas and sarcomas. Tumor control probability, relapse time and the corresponding number of PM cells (which is proportional to the second cancer risks, ERR) associated with a specific protocol (for a fixed total dose of 60 Gy) are presented in Table 6.3.

Protocol	**TCP**	**Recurrence** (days)	**Number of PM cells**
Conventional	98.21	2841.7	15.9
Hypo-fraction	98.41	2878.6	12.2
Hyper-fraction1	88.38	2633.7	13.1
Hyper-fraction2	19.87	2322.7	13.2

Table 6.3: Summary of TCP, recurrence and second cancer risks for a fixed total dose of 60 Gy.

From Table 6.3, we observe that the TCP and relapse time are almost the same for conventional and hypo-fractionated regimens, but second cancer risks induced by hypo-fractionation regimen are reduced by 22% in comparison to the conventional protocol. Our analysis indicates that hypo-fractionation appears to be a stronger regimen in terms of improvement in local disease control, increase in disease free survival time and a reduction in second cancer risks compared to the conventional regimen.

6.3.2 Efficacy of dose escalation

One of the main reasons for dose escalation is to eliminate all cancerous cells from the system, i.e. to increase primary tumor control and decrease the relapse rate (i.e., ideally, having a zero recurrence time, or increasing the relapse time to more than life time of the patient). Clinically, escalating the dose to the target volume can be carried out in several ways, either by increasing dose per fraction or increasing the overall treatment time. This process will have an impact on the TCP values, which in turn changes the average number of residual cancerous cells that remain post irradiation. The effect of these changes on the remaining number of tumor cells then changes the relapse time for the cancer, and a sensitivity of the recurrence time can be calculated for a given increase in radiation dose. Therefore, dose escalation will have a predominant effect not only on local control of disease but also on the relapse time, which is displayed in Figure 6.3 for a conventional regimen. The effect of dose escalation (by 2 Gy per fraction, i.e. by increasing the overall treatment window by 4-5 days) on the relapse dynamics are illustrated in Figure 6.3 for a conventional protocol.

Tables 6.4-6.7 present an analysis on the effect of dose escalation for various treatment regimens used in current clinical practice, with respect to TCP, recurrence time and second cancer risks.

It is interesting to study the changes in TCP, recurrence time and second cancer risk behavior for various dose escalation protocols. Dose is escalated from 60 Gy to 72 Gy according to the definitions of the corresponding fractionation regimens. For a conventional protocol when the dose is escalated by 12 Gy (i.e. from 60 Gy to 72 Gy), TCP increased by only 1%, relapse time increased by 365 days, and second cancer risks are reduced by 6%. However, in the case of the hypo-fractionated regimen, we notice that when the dose

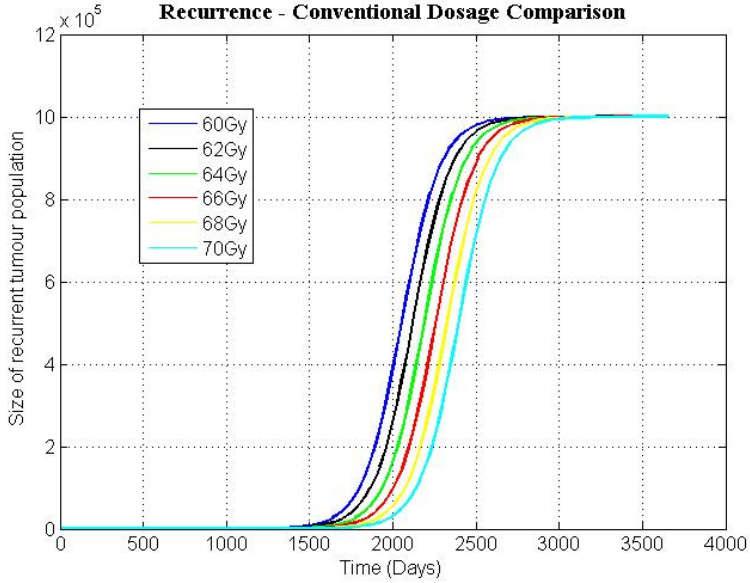

Figure 6.3: Effect of dose escalation on recurrence time for conventional regimen.

Dose (Gy)	**TCP**	**Recurrence** (days)	**Number of PM cells**
60	98.21	2841.7	15.9
62	99.00	2930.5	15.7
64	99.45	2977.0	15.5
66	99.69	3069.5	15.3
68	99.83	3107.7	15.1
70	99.91	3206.8	14.9

Table 6.4: Effect of dose escalation using conventional regimen.

is escalated by a similar amount (i.e. by 12 Gy), we observe that relapse time increased by 380 days and there is a corresponding reduction in second cancer risk of 20.8%. The effect of dose escalation on (both the) hyper-fractionation schemes is much less effective

Dose (Gy)	**TCP**	**Recurrence** (days)	**Number of PM cells**
60	98.41	2878.6	12.2
63	99.34	2958.8	11.6
66	99.73	3053.1	11.0
69	99.89	3171.7	10.3
72	99.96	3258.9	9.7

Table 6.5: Effect of dose escalation using hypo-fractionation regimen.

Dose (Gy)	**TCP**	**Recurrence** (days)	**Number of PM cells**
60	88.38	2633.7	13.1
63	94.50	2697.2	12.6
66	97.48	2825.4	12.0
69	98.86	2900.1	11.3
72	99.48	2995.8	10.7

Table 6.6: Effect of dose escalation using hyper-fractionation1 regimen.

when compared to other protocols. This is because the increase in recurrence times is observed to be greater for conventional and hypo-fractionated protocols, but is reduced in hyper-fractionated protocols. Additionally, second cancer risks do not show a significant reduction with hyper-fractionated schemes. Our analysis therefore suggests that the hypo-fractionation scheme is an efficient regimen during dose escalation and has a very significant effect on recurrence time and also on second cancer risks. Therefore, increasing the overall treatment time (by dose escalation) may theoretically increase the survival time of patients by approximately one year (or more) and may also concomitantly reduce second cancer

Dose (Gy)	**TCP**	**Recurrence** (days)	**Number of PM cells**
60	19.87	2332.7	13.2
63	43.08	2420.7	12.7
66	64.97	2499.3	12.1
69	80.19	2567.7	11.5
72	89.31	2619.2	10.8

Table 6.7: Effect of dose escalation using hyper-fractionation2 regimen.

risks. This analysis therefore may provide a theoretical justification for further clinical trials comparing efficacy of dose escalation and second cancer toxicities between conventional and hypo-fractionated radiotherapy protocols.

6.4 Short summary

In this chapter, we discussed short term and long term effects associated with radiation therapy. Short term toxicities include relapse of the primary tumor, and long term complications occur as a result of secondary malignancies in one of the neighboring organs of the target volume. We investigated the effect of various protocols on TCP, relapse time and the corresponding second cancer risks. We observed that TCP and relapse time are identical for both conventional and hypo-fractionated regimens. But, the second cancer risks induced by hypo-fractionation were reduced by 22% compared to the conventional protocol.

Additionally, we also explored the effect of dose escalation on TCP, recurrence time and second cancer risks by lengthening the overall treatment window. These changes have

affected the recurrence time by 300-400 days, approximately, which can represent a significant treatment gain from a clinical perspective. Also, the hypo-fractionated regimen appears to be sensitive to dose escalation and the corresponding impact on tumor recurrence time, and reduction in second cancer risk. The reduction in second cancer risk is approximately 20% when the dose is increased from 60 Gy to 72 Gy in a hypo-fractionated protocol.

From our analysis, we conclude that the radio-biological benefit from hypo-fractionation is higher compared to other regimens from the point of view of TCP, relapse time and second cancer risks. Therefore, hypo-fractionation may be a more efficient regimen in the context of TCP, recurrence time and second cancer risks. Overall, this study demonstrates the importance of including a second cancer risk model in conjunction with TCP and relapse dynamics framework to design an efficient regimen. This theoretical analysis might provide a basis for future clinical trials testing hypo-fractionation and conventional protocols on TCP, relapse and second cancer risks.

Chapter 7

Evolutionary Dynamics of Cancer

7.1 Introduction

Radiation induced second cancers are thought to arise as a result of multiple mutations of healthy cells post irradiation of the primary tumor. As discussed in the literature on primary cancer age incidence modeling [120]-[121], the manifestation of a second cancer may occur as a result of a two-hit process. Anti-cancer therapies such as radiation (or even, chemotherapy), introduce a first hit to some of the normal cells in the vicinity of the tumor volume. This introduces a sub-population of radiation induced cells in the system [53], the so called pre-malignant cells. The detailed biological mechanisms such as initiation and progression of pre-malignant cells resulting from radiation exposure are still not well understood. It has also been suggested that radiation therapy can introduce chromosomal and genomic instabilities, and thus makes the second hit mutations more effective and unpredictable in nature [122].

On the other hand, the carcinogenesis and evolutionary dynamics of two-stage mod-

els of cancer progression have been discussed extensively in the literature. These works quantify the (fixation) dynamics of how an advantageous mutant (for example, a radiation induced mutated cell) can outgrow a background population of normal cells and upon a second (malignant) mutation can result in a malignant niche and eventually lead to a full blown malignancy. Additionally, these formalisms have also been successfully applied to describe chromosomal instability [154]-[155]. It has also been proposed that second cancers may arise due to the creation of residual pre-malignant cells which can proliferate during treatment and eventually grow post irradiation [53]. It is very important (and also clinically relevant) to model the changes of radiation induced risk over time. However, in this work, we estimate the life time risk of secondary cancers due to various treatments and the survival probability of radiation-induced pre-malignant cells to take over a small niche.

Many biological problems can be described by deterministic equations, but this approach fails to capture some important aspects like randomness in micro-environment, invasion probability, fixation time, etc. Hence, we require a stochastic formulation to analyze the dynamics. The dynamics of cells is often described by a stochastic process such as a simple birth-death process. One approach that has been widely used in different applications, including progression of primary cancer [123], dynamics of metastasis [124], dynamics of tumor suppressor gene inactivation [125] and in other areas such as language evolution [126] is the Moran process. Before describing the mathematical framework, we will discuss the basic principles of the Moran process that govern the dynamics like selection, mutation and genetic random drift. Selection occurs when different types of individuals compete with each other for resources. When the duplication of DNA or RNA (ribonucleic acid) goes away, it might lead to mutations. The frequency of alleles with the same fitness may change at random through time in a process known as genetic drift.

In order to describe the selection dynamics in models with stochasticity, birth-death

models such as the Moran process has been proposed in the literature [123]. The Moran process is in a sense, the simplest birth-death or one-step process with constant total population, in which at each time step one cell reproduces and another cell dies so that the total number of cells is constant [127]. Consider a constant population of N cells (under homeostatic control in the tissue), consisting of two types of reproducing cells A and B. For birth, one of the N cells is chosen at random proportional to fitness. This gives rise to its lineage subject to possible mutation. For death, one of the N cells is chosen at random. The total population size, N, is strictly constant at time t. Time is measured in units of cell divisions. Fitness of a cell represents the reproductive rate. It is assume that cell division follows an exponential distribution with average $1/r$. A fitness rate $r = 1$ is assigned for type A cells and type B cells have a fitness rate equal to r. At time $t = 0$, all N cells are of type A. After some time, a single mutant cell of type B will be generated. This cell will lead to a lineage of type B cells that will either become extinct or proceed to fixation (i.e. until the system consists of type B cells only). The probability that a single type B cell takes over the whole system is termed the fixation probability. Figure 7.1 illustrates the Moran process in a space free system. Suppose type A has a fitness rate $r_A = 1$ and type B has fitness rate $r_B = r$. If the fitness rate r>1, then selection is in favor of B; if r<1, then selection is in favor of A; and if r=1, selection is neutral. Suppose all the individuals in the population are identical. The probability that a type A cell reproduces an A is $1 - u$; a type A cell mutates to B with probability u (per cell per generation); and type B cells always reproduce B cells again. If i is the number of B cells denoted by n_B and $(N - i)$ is the number of A cells denoted by n_A. The probability that a new cell of type A is reproduced is given by

$$p_{A+} = \frac{r_A n_A}{r_A n_A + r_B n_B}(1 - u) = \frac{N - i}{N - i + ri}(1 - u).$$

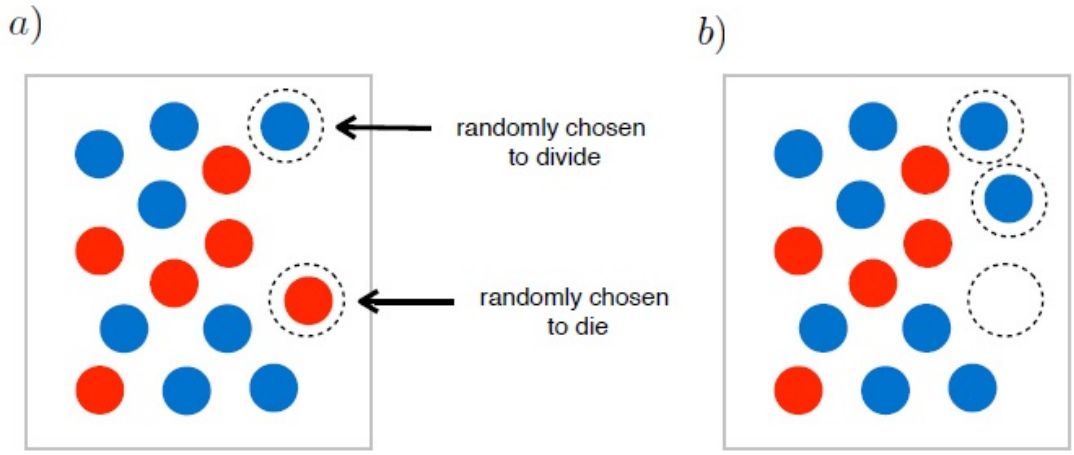

Figure 7.1: Moran process in a finite population.

The probability that a new cell of type A dies out is given by

$$p_{A-} = \frac{n_A}{N} = \frac{N-i}{N}.$$

The probability that a new cell of type B is reproduced is given by

$$p_{B+} = \frac{r_A n_A}{r_A n_A + r_B n_B} u + \frac{r_B n_B}{r_A n_A + r_B n_B} = \frac{N-i}{N-i+ri} u + \frac{ri}{N-i+ri}.$$

The probability that a new cell of type B dies out is given by

$$p_{B-} = \frac{n_B}{N} = \frac{i}{N}.$$

The Moran process is then defined on the state space $i = 0, ..., N$. The transition matrix

of moving from state $n_B = i$ to $n_B = j$ is given by

$$T_{ij} = \begin{cases} \dfrac{(N-i)u + ri}{N-i+ri}\dfrac{N-i}{N}, & j = i+1 \\ \dfrac{(N-i)(1-u)}{N-i+ri}\dfrac{i}{N}, & j = i-1 \\ 1 - T_{i,i+1} - T_{i,i-1}, & j = i \\ 0, & \text{otherwise} \end{cases}$$

When mutations are rare i.e. $u \to 0$ (mutations are rare in the time scale of selection, i.e. the average time it takes to take over the whole system), then the transition matrix is given by

$$T_{ij} = \begin{cases} \dfrac{ri}{N-i+ri}\dfrac{N-i}{N}, & j = i+1 \\ \dfrac{N-i}{N-i+ri}\dfrac{i}{N}, & j = i-1 \\ 1 - T_{i,i+1} - T_{i,i-1}, & j = i \\ 0, & \text{otherwise} \end{cases}$$

Suppose ρ_i denotes the fixation probability, i.e. the probability that i number of type B cells will take over the whole system. Then the fixation probabilities for the absorbing states is given by $\rho_0 = 0$ and $\rho_N = 1$. We now derive the fixation probability for all the transient states.

$$\rho_i = T_i^- \rho_{i-1} + (1 - T_i^- - T_i^+)\rho_i + T_i^+ \rho_{i+1}$$

which can be rewritten as:

$$T_i^+(\rho_{i+1} - \rho_i) - T_i^-(\rho_i - \rho_{i-1}) = 0$$

Let $\theta_i = \frac{T_i^-}{T_i^+}$, and let $\alpha_{i+1} = \rho_{i+1} - \rho_i$, $\alpha_i = \rho_i - \rho_{i-1}$. Using recurrence relations between the fixation probabilities, and by assuming $\alpha_{i+1} = \theta_i \alpha_i$, we obtain a set of recurrence equations as follows:

$$\begin{aligned} \alpha_1 &= \rho_1 - \rho_0 = \rho_1 \\ \alpha_2 &= \rho_2 - \rho_1 = \theta_1 \rho_1 \\ &\vdots \\ \alpha_N &= \rho_N - \rho_{N-1} = \rho_1 \Pi_{i=1}^{N-1} \theta_i \end{aligned}$$

Clearly, $\sum_{k=1}^{N} \alpha_k = 1$. But, $\sum_{k=1}^{N} \alpha_k = \sum_{k=1}^{N} \rho_1 \Pi_{j=1}^{k-1} \theta_i$ (from the above set of equations). Therefore, the fixation probability of a system comprised of $N-1$ type A cells and one type B cell is given by:

$$\rho_1 = \frac{1}{1 + \sum_{i=1}^{N-1} \Pi_{j=1}^{k} \theta_j}. \tag{7.1}$$

7.2 Spatial modeling

7.2.1 Background

Spatial effects on finite populations can be divided into two categories. One type of spatial effect arises from the structure of the network or the graph, which has a predominant influence on the fixation probability. The second type of spatial effect arises from a random fitness distribution of mutants on a given network structure or a graph. There are numerous real world populations associated with finite populations on complex spatial structures and random distributions of mutants, such as in biological and ecological networks, information theory, etc. Taking these into consideration, and from a Moran process perspective, the

species might have a higher chance to interact with those located in its neighborhood rather than with those located far away. Hence, spatial effects on evolutionary dynamics are considered by assuming that the species are distributed randomly over a spatial domain interacting with their nearest neighbors. The generalization of the space-free Moran model to a graph is not unique. There are several types of updating rules on spatial networks, which can be considered an extension of the space free Moran model. Some of the most common updating strategies on spatial structures are for an invasion process (IP), i.e a birth-death process, and voters model (VM), i.e. death-birth process [142]. In an IP framework, we assume a birth-death model where an individual is first chosen (based on its fitness) for reproduction. Then, an offspring is replaced proportional to the weight of the link connecting to its neighbors. The updating rules get reversed in a VM formalism. In a VM model, one chooses a random individual to die, which is then replaced by one of its neighbors based on their fitness and the weight of the links connecting them. Depending on the nature of the graph, both these updating strategies yield different values of the fixation probability.

7.2.2 Fixation probability on graphs

We present a brief review of the literature incorporating spatial effects (related to the network or structure of a graph) in evolutionary processes. This might give us some insight on the dependence of cancer evolution on spatial structure as well as on the evolving spatial patterns. The introduction of space into an evolutionary model has been generally formulated using a grid-based approach such as a cellular-automata model on a lattice or as an unstructured mesh, or as a network representing the connections between locations or individuals. These networks can vary from a simple graph to a very complex structure.

For the past three decades, there have been several attempts made to understand the process of fixation in spatially homogeneous systems. It was found that many spatially structured models such as lattice models have little or no effect on the selection process [148]–[150]. More recently, Lieberman et al. [151] generalized this to arbitrary graphs and found the exact symmetry conditions under which the fixation probability for an advantaged mutant, evolving on a graph, is the same as that for a mixed population model. Houchmandzadeh et al [152] demonstrated that fixation probability of a beneficial mutation in a geographically structured population is almost the same (or, slightly smaller) compared to the unstructured population for a Voter framework.

A graph is a collection of nodes which are connected by edges (which can be either unidirectional or bidirectional). Recently, the evolution of populations whose spatial structure is given by a graph has been considered in [138], Here it is shown that certain types of structures amplify the fixation probability of a mutant that is introduced into the system. The individuals occupy the vertices of a graph, and the edges denote interactions between species. In each time step, an individual cell is selected with a probability proportional to its fitness; the weights of the outgoing edges determine the probabilities that the corresponding neighbor will be replaced by the offspring. The process is described by a stochastic matrix W, where w_{ij} denotes the probability that a lineage from individual i will replace individual j. In a more general setting, at each time step, an edge ij is selected with a probability proportional to its weight and the fitness of the individual at its tail. The Moran process is the special case of a complete graph (a graph in which every pair of nodes is connected with unique edges) with identical weights. Interestingly, on a complete graph (i.e. where every node is connected to everyone else and the offspring of each species can replace any other species with equal probability, the fixation probability under an invasion process updating strategy is equivalent to that of the Moran process

fixation probability ([123]):

$$\rho_{\text{Moran}} = \rho_{\text{IP}} = \frac{1 - \frac{1}{r}}{1 - \frac{1}{r^N}}. \tag{7.2}$$

Consider a homogeneous population of size N. At each time step an individual is chosen for reproduction with a probability proportional to its fitness. The offspring replaces a randomly chosen individual. In this Moran process, the population size remains constant. Suppose all the resident individuals are identical and one new mutant is introduced. The new mutant has relative fitness r, as compared to the residents, whose fitness is 1. The fixation probability of the new mutant is given by Equation (7.2). The population structure is introduced in the following manner. Individuals are labeled $i = 1, 2, ...N$. The probability that individual i places its lineage into position j is given by w_{ij}. Thus the individuals can be thought of as occupying the vertices's of a graph. The matrix $W = w_{ij}$ determines the structure of the graph. If $w_{ij} = 0$ and $w_{ji} = 0$ then the vertices i and j are not connected. In each iteration, an individual i is chosen for reproduction with a probability proportional to its fitness. The resulting lineage will occupy vertex j with probability w_{ij}. Here, W is a stochastic matrix, which means that all its rows sum to one. The fixation probability of a randomly placed mutant is then calculated. If W is symmetric, $w_{ij} = w_{ji}$, then the fixation probability is always ρ_1. The individuals that are arranged on a spatial lattice can be triangular, square, hexagonal, the value of ρ remains unchanged and it is equal to ρ_1. Leiberman et al. [151] proved that some graphs (such as stars, super stars) have different fixation probabilities.

We have discussed the subgroup of graphs that have the same fixation probability as the conventional space-free Moran model, which are known as isothermal graphs. Generally, isothermal graphs include all regular graphs (constant number of neighbors at each vertex) and more generally symmetric (undirected) graphs. Typically random number of neighbors

or boundaries (where the number of neighbors inevitably change) can make good examples for non-isothermal graphs. Although, the IP model is equivalent to the Moran fixation probability, but in strict sense, a general voter model does not follow isothermal theorem. This scenario is discussed in the next section for a one dimensional case.

7.2.3 Fixation probability on 1D

The first spatial (1-D) generalization of the Moran process was described in [139], where both one-hit and two-hit mutant fixation processes are considered. A death-birth updating strategy is implemented to calculate the fixation probability. A 1-D spatial generalization of a constant population Moran process has been studied by [139], on the role of spatial dynamics in carcinogenesis. The structure is designed in the following manner: cells are aligned along a regular grid at locations $1, 2, ..., N$ assuming the total number of cells does not change. Cells are randomly chosen for death. Each cell death is followed by a cell division of one of its two neighboring cells, which places its daughter cell at the empty slot. Cell death occurs randomly and division rate is proportional to the relative fitness of the cells.

Let us assume two types of species A and B coexist with corresponding populations $n_A = N - i$ and $n_B = i$, which add up to a constant population N. Suppose the fitness of type B individuals is r and fitness of type A species is assumed to be unity. Then, at each time step (taken to be $\sim \frac{1}{N}$), one individual is chosen to die (the death rate of both species is assumed to be the same). Another individual is chosen to reproduce proportional to its

fitness. Then the transition probabilities are given by:

$$p_{i,i-1} = \lambda_i = \frac{ri(N-i)}{(N+ri-i)N}$$
$$p_{i,i+1} = \mu_i = \frac{m(N-i)}{(N+ri-i)N}$$

Suppose ρ_i denotes the fixation probability, i.e. the probability that i number of type B cells will take over the whole system. We can write down the recurrence equations as follows:

$$\begin{aligned}
\pi_i &= \lambda_i \pi_{i+1} + \mu_i \pi_{i-1} + (1 - \lambda_i - \mu_i)\pi_i \\
\pi_1 &= \lambda_1 \pi_i + (1 - \lambda_i - \mu_i)\pi_1 \\
\pi_N &= 1
\end{aligned}$$

where λ and μ are birth and death rates. The solutions of the above equation are the same as the conventional Moran model with the exception that the ratio of birth and death rates is not always equal to the fitness rate, i.e.

$$\frac{\lambda_1}{\mu_1} \neq \frac{1}{r}. \tag{7.3}$$

Let us denote the ratio $\frac{\lambda_1}{\mu_1} = \gamma_0$, then the solution for the fixation probability is given by:

$$\begin{aligned}
\pi_1 &= \frac{1}{1 + \sum_{j=1}^{N-1} \Pi_{k=1}^{N-2} \frac{\mu_k}{\lambda_k} \gamma_0} \\
&= \frac{1}{1 + \left(\frac{1 - (\frac{1}{r})^{N-1}}{1 - \frac{1}{r}} \right) \gamma_0}
\end{aligned} \tag{7.4}$$

It should be noted that if $\gamma_0 = \frac{1}{r}$, we recover the fixation probability of the Moran process. For a complete graph,

$$\gamma_0 = \frac{\lambda_1}{\mu_1} = \frac{1/N}{\frac{r(N-1)}{N(r+N-1)}} = \frac{1}{r} + \frac{1}{N-1} \tag{7.5}$$

The value of γ_0 is slightly different from $1/r$. In general, we expect it to be proportional to the number of neighbors in the graph, thus one expects the most dominant effect to belong to the circle (or, 1D graphs). For a circle, the extinction probability is still the same ($= 1/N$), but the birth rate is given by:

$$\gamma_0 \;= \frac{\lambda_1}{\mu_1} = \frac{1/N}{\frac{2r}{N(r+1)}} = \frac{r+1}{2r} \tag{7.6}$$

Using the above proliferation and extinction rates, the fixation probability will now be reduced to a compact form (obtained in) [141], which is consistent with the result of Komarova [139]:

$$\pi_i = \frac{2r^{N-1}(1-r)}{1+r+r^{N-1}-3r^N} \tag{7.7}$$

One of the important observations from the above equation is that solutions for the fixation probability on isothermal graphs (such as a circle) are not identical to the fixation probability of a space-free model or for a complete graph. This is mainly due to the fact that the ratio of extinction probability and birth rate of a single individual B left in the system is different from the reciprocal of its fitness.

7.2.4 Effect of cellular motility on fixation probability on 2D

In this section, we introduce migration also known as cellular motility into the system. Cellular motility is a very important phenomenon that is observed in many biological systems. In particular, several experimental studies have suggested that in the later stages of carcinogenesis, cells undergo a transition and become more motile (termed as the Epithelial-Mesynchemal transition (EMT)), and this new phenotype with higher migration potential escapes from the system and colonizes a different organ. Thus, a pertinent question is to understand the interplay of migration potential and proliferation of mutants on various

structures and their impact on the fixation probability. It should be noted that the fixation probability is also referred to as the invasion probability throughout this chapter.

The derivation in the previous section (for the one dimensional case) does not apply to the corresponding two-dimensional scenario; however we can make an approximation on the case of 2D of regular graphs. Additionally, the presence of boundaries (i.e. reflective boundary conditions) along with randomness of the structure are very difficult to model analytically. To include the possible migrative potential of the two phenotypes, a second generalization of this model is introduced in [159], where a population of N cells consisting of cells of types A and B, is placed on a regular lattice (such that all grid points are filled with either of the phenotypes). Suppose r_A and r_B are the proliferative rates and m_A and m_B the migrative rates (cellular motility) of type A and B cells, respectively. Applying the space free Moran process formulation, at each time step a cell is chosen randomly to die. Then one of the following four events might occur: A divides, A migrates, B divides, B migrates. If a reproduction event of either A or B occurs, then the update is complete and the process is repeated again. Suppose that a migration event of either A or B occurs, then the empty spot is occupied by a migratory cell, leaving an another empty spot behind. Again, a new elementary event is considered till the empty spot is filled (i.e., until the occurrence of a birth event). The lattice is always filled up at the end of each update following the Moran process assumption that the whole population is constant at every iteration.

The model chooses the nearest neighbors around the empty spot taken to be a von-Neumann neighborhood (i.e. a cell surrounded by four neighbors). Suppose n_A and n_B are the numbers of type A and B cells around the empty spot respectively, then the

probabilities of each elementary event are given by:

$$\begin{aligned} P_{\text{A div}} &= \frac{n_A r_A}{\Delta}, \\ P_{\text{B div}} &= \frac{n_B r_B}{\Delta}, \\ P_{\text{A mig}} &= \frac{n_A m_A}{\Delta}, \\ P_{\text{B mig}} &= \frac{n_B m_B}{\Delta}, \end{aligned} \tag{7.8}$$

where $\Delta = n_A(r_A + m_A) + n_B(r_B + m_B)$. Introducing dimensionless variables, the above equations can be rewritten as:

$$\begin{aligned} P_{\text{A div}} &= \frac{n_A}{\hat{\Delta}}, \\ P_{\text{B div}} &= \frac{\lambda n_B}{\hat{\Delta}}, \\ P_{\text{A mig}} &= \frac{n_A k_A}{\hat{\Delta}}, \\ P_{\text{B mig}} &= \frac{\lambda n_B k_B}{\hat{\Delta}}, \end{aligned} \tag{7.9}$$

where $\lambda = r_B/r_A$, $\hat{\Delta} = (1 + k_A) + n_B\lambda(1 + k_B)$ with $k_X = m_X/r_X$ (for $X = A, B$). For the spatial model outlined above, the simulations in [159] were performed on a square grid with periodic boundary conditions.

It was shown that migration is a key regulator of the fixation probability. Fixation probability is reported to be smaller on a lattice (for advantageous mutants) with zero migration (for both host and mutants) compared to a space-free system. As migration increases, the fixation probability is shown to increase and stays almost constant for higher migration rates. One of the reasons for the saturation can possibly be that migration has less impact compared to proliferative mechanism. Even in the presence of host cell

migration, the fixation probability increases and stays constant. An increased migration potential of mutants increases their ability to invade the system. But for smaller migration potentials, mutants tend to concentrate in a small island, resulting in an expansion only at the boundary of that region. In the case of larger migrative potentials, mutants move around in the space reaching everywhere in the system. In the 2D case it was shown that cellular motility has a direct positive impact on the ability of a single mutant to invade a the whole system.

7.3 Summary

In this chapter, we discussed a mixed population (space free) Moran process framework and presented the background for spatial systems in evolutionary dynamics. Although there are several types of updating rules on networks and graphs, we adopt the death-birth process or the VM strategy for the rest of our work. Generally, spatially heterogeneous systems have two distinct components, one component defines the spatial structure of the network (only), and the second component encapsulates the randomness of resources and fitnesses of host and mutants within the system (for a fixed network). In the next two chapters, we investigate the effect of unstructured and random meshes on the invasion (or, fixation) probability in the presence and absence of migration. Additionally, we also explore the site dependent random fitness of mutants and host cells on a lattice (in the presence and absence of migration) and its effect on the invasion probability.

Chapter 8

Spatial Structure Impact on Invasion Probability

8.1 Introduction

The following chapter has been taken from our published paper. [1] Carcinogenesis can be viewed as an evolutionary process, where a collection of pre-neoplastic cells acquire genetic and epigenetic changes over a period of time [153]. During the process of carcinogenic evolution, it is commonly believed that mutant cells gain a fitness advantage and take over a small neighborhood of host cells through a selection process and initiate a clonal area, leading to invasion into the neighborhood tissue. The fitness rates of pre-neoplastic cells are affected by a mutation-selection mechanism and various micro-environmental factors. This

[1] Manem VSK, Kohandel M, Komarova NL, Sivaloganathan S, Spatial invasion dynamics on random and unstructured meshes: Implications for heterogeneous tumor populations, J Theor Biol 349 (2014) 66-73.

results in a high level of heterogeneity at the cellular level in a tumor. Both tumor initiation and progression stages have been proposed to follow an evolutionary stochastic model and different authors have observed the effect of a fitness advantaged mutant introduced into the system and the probability that this takes over a finite compartment of the cellular tissue. In recent years (see [154]–[160]), these models have been successfully applied to both one-hit and two-hit mutation-selection processes. During the final stages of malignancy, the mutant phenotype gains a relative advantage through cellular motility. The evolutionary theory of these complex phenomena has not yet been addressed in the literature.

The spatial dynamics of cancer invasion has been studied by several authors using several approaches which include cellular automata, partial differential equation models, and hybrid models (combining discrete and continuous) including multi-scale modeling techniques [162]—[165]. Although, it is possible to encapsulate progressively more complex cellular mechanisms and biological phenomena into these models, we however adopt a simpler approach. In an attempt to understand and analyze the dynamics of invasion, we focus on only two cellular forces, namely, proliferative and migrative potentials which may well dictate the inherited genetic behavior of mutants. Our approach builds on spatial evolutionary modeling of cancer discussed in the previous chapter.

The main objective of this study is to develop a better quantitative analysis of the invasion probability, by avoiding the rigid framework imposed by a regular grid (i.e. lattice). Although a tissue is considered to be a three-dimensional mesh, but from the point of view of computational efficiency we assume a two-dimensional grid. We introduce a stochastic death-birth model for the spatial evolutionary system (described in the previous chapter). In order to circumvent the rigidity of a regular grid, we use two different methods. In the first construction, we start with a regular square lattice in which neighbors are modified (i.e. added, or removed) in a random way. The background square lattice can

be either a Moore neighborhood type (i.e., a grid point surrounded with 8 neighbors), or, von-Neumann neighborhood (i.e. a grid point surrounded with 4 neighbors. The important feature of this construction of the connectivity graph is the notion that we construct the number of neighbors for each of the nodes on the lattice (where each node is occupied by either a normal or a mutant cell). The connectivity of the graph is a mixture of both directed and undirected links, i.e., some nodes and their neighbors are bi-directional and some are uni-directional.

Generally speaking, any regular grid assumes that the number of neighbors around each cell is homogeneous at every location in space. This is not a realistic assumption for modeling biological tissue architectures. Therefore, we approximate a real tissue architecture by an unstructured mesh (closer to a real tissue in terms of the number of neighbors around a point), where the number of neighbors around each nodal position is a random variable. This suggests our second construction, where we consider an unstructured mesh which is defined as a random neighborhood graph with longer ranges of connectivities versus the previous case. The important feature that distinguishes is compared to the previous construction however, is the fact that the unstructured mesh does behave symmetrically between the two type of species in terms of the connectivity graph and the number of neighbors. The contrasting feature in the unstructured mesh construction is that every node and its corresponding neighbors are bi-directional compared to the previous scenario (which are either uni-directional or bi-directional).

Here, we are mainly concerned with the question of fixation (or, invasion) probability in the presence of a migration potential (or, cellular motility) for either only the mutant cell or for both the normal and mutant cells. We address the effects of a random environment (in the context of heterogeneous structure) and migration potential on the fixation probability. The effect of boundaries on the value of the fixation probability is briefly discussed at the

end.

8.2 Random neighborhoods on a lattice

It is clearly evident that the set of equations (7.9) are dependent on the number of neighboring cells of type A and B, which is fixed in the approach described in [159]. We now generalize the model to include random sets of neighbors at each nodal position. This leads to changes in n_A and n_B for each node, that in turn might affect the cellular dynamics of the whole system. We explore the possible consequences of this change in two different numerical experiments. The algorithm outlined in the previous chapter is applied for all the computations in this work by running 5 sets of simulations of $10,000$ iterations each, and each iteration is performed until, for a fixed neighborhood, the system reaches one of the absorbing states (either zero, or all mutants) and we estimate the invasion probability. The uncertainty is obtained using the definition of standard deviation and plotted along with the mean.

As discussed earlier, the isothermal theorem for graphs [151] states that, if each node of a graph has the same number of neighboring nodes, i.e. a symmetric bidirectional graph, then the invasion probability is equivalent to that of the fixation probability of the traditional Moran process in the absence of migration. This clearly suggests that the invasion probability obtained from symmetric graphs provides no further insight into the complex features of the tissue architecture. As a result of this, we examine the variation in the invasion probability for two different experiments by introducing randomness so that it specifically introduces asymmetry into the lattice.

8.2.1 Static random neighborhoods

In the first scenario, we investigate the invasion dynamics resulting from a random number of neighbors chosen from a fixed distribution at each node on a regular lattice. This simulation is carried out by fixing the mean number of neighbors and varying the width of the distribution. The neighborhood size for each grid point is assumed to be a random, integer-valued variable distributed uniformly over a given interval. We varied this distribution from a delta-function to a relatively wide spread distribution. This experiment is carried out to investigate the correlation between the invasion probability and the distribution width. We considered a regular, square lattice comprised of $21 \times 21 = 441$ cells with reflecting boundary conditions. Random numbers of neighbors are generated from a uniform distribution, in such a way that the average number of neighbors is always 4, but the corresponding width varies.

The algorithm used for the experiments can be summarized as follows. The following construction is implemented in such a way that the delta distribution follows a background mesh, i.e., a lattice with four neighbors. For each nodal point on the grid, we generate a random set of neighbors from a given distribution, say $D = [2, 6]$. The number of neighbors for each node will then be $2, 3, \ldots,$ or, 6. Distances are then computed from every node to all other nodes on the lattice. The nearest set of neighbors for a particular node is then considered depending on the nodes that are located closest to the parent node. If two or more nodes are located at the same distance from the given node, then we randomly pick a node. In this way, the construction introduces a mixture of both directed and undirected links between a node and its neighbors (i.e. some nodes and their neighbors may be symmetric (bi-directional), while others will be asymmetric (uni-directional)). The set of neighbors generated for each node on the lattice is fixed throughout the experiment.

For a distribution with zero width (on a lattice), the fixation probability of the mutant highly depends on its proliferative and migrative potentials. Simulations were carried out by applying the algorithm outlined in the previous chapter with reflecting boundary conditions for advantaged mutants. We obtain a similar figure with approximate values of invasion probability captured in Figure 1 in the paper [159]. Additionally, if the number of neighbors is uniformly increased or decreased, i.e., each node still consists of the same number of neighbors, we can intuitively assume that this may not change the invasion probability.

We now introduce a variation on the number of neighbors at each nodal position on the grid, which can be attributed to the asymmetry of the lattice. At the start of each simulation one type B cell is introduced at a randomly chosen position in the lattice, where the remaining cells populating the lattice are type A cells. Simulations are run, and each iteration is performed until, for a fixed neighborhood, the system reaches an absorbing state, and we estimate the fixation probability.

In the first scenario, simulations were carried out for advantaged mutants ($\lambda = 1.5$) assuming zero migration for both types of cells. The effect of the width of the distribution on the invasion probability is captured in Figure 8.1 for a migration free system. It is clearly evident that the invasion probability decreases with the width of the distribution.

Secondly, the simulations were run only for advantaged mutants (for instance, $\lambda = 1.5$) assuming the migration of A cells is zero, i.e. $k_A = 0$. This experiment is done in order to understand the impact of migration on the invasion probability. The effect of the width of the distribution on the invasion probability is plotted in Figure 8.2, where zero width corresponds to the results reported in [159]. From the figure, we clearly observe that the invasion probability is negatively correlated with the width of the distribution, i.e., as we increase the width of the distribution the invasion probability decreases. In the presence

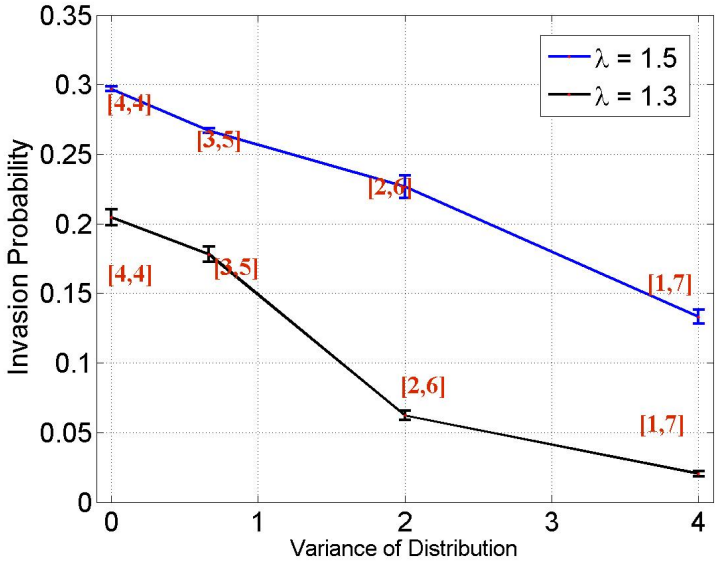

Figure 8.1: Invasion probability of mutants as a function of varying distribution width with static random neighborhood in a migration free system. Parameters: lattice size $= 21 \times 21$,$\lambda = 1.5, 1.3, k_A = k_B = 0$.

of migration which is captured in Figure 8.2, we do not observe a significant change in the invasion probability for the distribution $[3, 5]$ compared with a migration free system. However, for distributions $[2, 6]$ and $[1, 7]$, migration suppresses the invasion probability, due to the chaotic architecture. The invasion probability drops to the order of 10^{-3} when neighbors are selected from the distribution $[1, 7]$.

The invasion probability decreases with increasing distribution width. One of the main reasons for this decline in the fixation probability is that the randomness of the architecture pushes the generated random mesh far away from the isothermal graph (whose invasion probability is equivalent to that of the Moran process fixation probability). This has been earlier studied on scale free networks [166]. For a high variance of the distribution of

neighbors, we can possibly have several clusters of cells which are very poorly connected to each other (due to the unidirectional construction of the random mesh). These poorly connected clusters increase as the variance increases, leading to mutant extinction implying a smaller invasion probability.

8.2.2 Dynamic random neighborhoods

The second numerical experiment is similar to the one described above, except that we generate a new random set of neighbors at every iteration. This experiment is carried out to examine the effect of the change in tissue geometry after every iteration. Simulations were run, and each iteration is performed until, for a fixed initial neighborhood, the system reaches one of the absorbing states and we estimate the invasion probability. The effect of the width of the distribution on the invasion probability is similar to the plot presented in Figure 8.1 for a migration free system. Intuitively, averaging over a dynamic random neighborhood gives a static random neighborhood. In order to understand the effect of migration of B cells on the invasion probability, we assumed the migration potential of type A cells to be equal to zero, i.e. $k_A = 0$. The simulations were run only for advantaged mutants ($\lambda = 1.5$) and for $k_B = 5.0$. The invasion probability is then computed for varying distribution widths, which is presented in Figure 8.2.

To summarize the above two experiments, the first simulation is carried out on a static neighborhood, i.e., the number of neighbors are static throughout the whole set of iterations, which can be thought of as a fixed set of neighborhood clusters over time for every node. In the second experiment (dynamic neighborhood) the number of neighbors changes for every iteration, i.e., this can be understood as the change in the neighborhood size over time. Although the neighborhood change over time might not look realistic in nature,

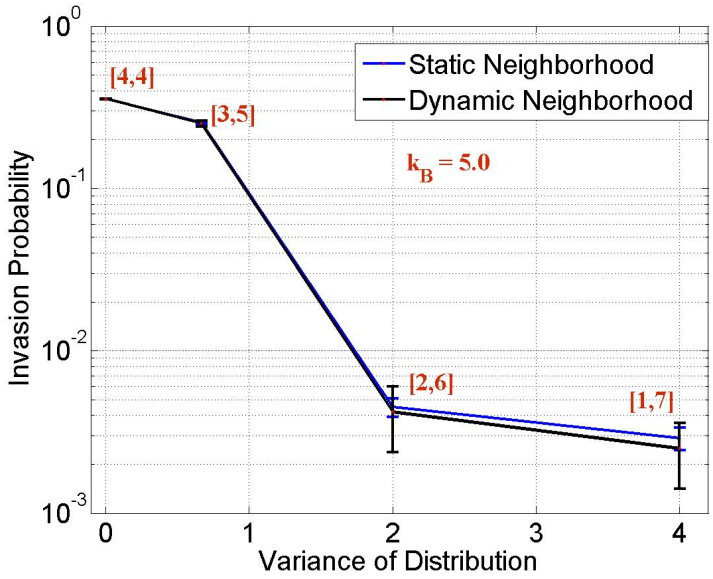

Figure 8.2: Invasion probability of mutants as a function of varying distribution width with static and dynamic random neighborhood. Parameters: lattice size = 21×21,$\lambda = 1.5, k_A = 0; k_B = 5$.

however, this might be interesting to understand at the behavior of the system numerically. In order to analyze the effect of varying distribution width of neighbors on the invasion probability, we consider the following fair comparison, the case of zero migrative potentials of both phenotypes, i.e., when $k_A = k_B = 0$. For a space free Moran process, the fixation probability is given by 0.3333 for an advantageous mutant with $\lambda = 1.5$. In the case of the lattice model with a fixed grid, corresponding to the zero-width distribution, $[4, 4]$, the invasion probability of an advantageous mutant with $\lambda = 1.5$ is given by 0.2969. This conveys that spatial structures have an effect on the fixation probability, which is consistent with other works in the literature. However, when we use a random neighborhood model and increase the distribution width to that of $[2, 6]$, the fixation probability drops

to 0.2267. This clearly indicates that for a migration free system, the increase in the width of the distribution inhibits the proliferative mechanism, thereby decreasing the invasion probability. Another interesting observation from Figure 8.2 is that, for the distribution $[1, 7]$ the invasion probability is of the same order as the invasion probability of a neutral mutant (whose fixation probability is given by $\rho_{\text{neutral}} = 1/N = 0.0022$). This suggests that an increase in the distribution width can eliminate the advantage given by a 50% increase in the proliferative potential. By increasing the width of the distribution, the invasion probability decreases rapidly and approaches the invasion probability of mutants with neutral drift.

From the biological perspective, the alterations in the neighborhood for each node can be attributed to tissue type (for instance morphological changes in a breast tissue is high compared to other tissues), tension, stress, and several other micro-environmental factors (such as hypoxic or acidic conditions) that fluctuate both spatially and also temporally. These results strongly suggest that the geometry of the neighborhood (either static/dynamic) plays an important role in the invasion probability under constrained boundaries, both in the absence and also in the presence of migration.

8.2.3 Unstructured mesh

We now examine the invasion dynamics of pre-cancerous cells on an unstructured mesh (where an unstructured mesh is a two-dimensional mesh with variable number of neighbors at each grid point). The construction of an unstructured (or, a Voronoi) mesh is completely different from the construction of the static and random neighborhood lattices in the previous section. An unstructured mesh is constructed using QHull in Matlab software. Recall that in the static (and also in the random neighborhood experiments), the connectivities

between a node and its neighbors are either unidirectional or bi-directional. In the case of unstructured meshes the links between a node and its neighbors are bidirectional. It is well known that on an unstructured grid, the number of neighbors at each location can vary greatly. The effect of the migration potential on the invasion probability is analyzed and compared with the corresponding results on a regular grid for two different scenarios. In the first scenario, we assume that the migration potential of mutants is $k_B > 0$ and the migration ability of A cells is chosen to be $k_A = 0$. In the second scenario we consider migration potentials of both types of cells to be $k_A, k_B > 0$.

Randomly, one mutant cell is introduced into the mesh whilst the rest of the cells populating the mesh are type A cells. Our system is now composed of $N - 1$ type A or host cells and a single mutant cell. The algorithm outlined in the previous chapter is applied with reflecting boundary conditions, again until one of the cell types becomes extinct, i.e. the system reaches one of the absorbing states. For all three cases of mutants, we observed that the invasion probability is much smaller when compared to the corresponding results on a lattice. The simulations were run for advantaged mutants ($\lambda = 1.5$), neutral mutants ($\lambda = 1.0$) and disadvantaged mutants ($\lambda = 0.9$). And, the effect of the migration potential on the invasion probability is plotted for each value of k_B. Simulations are run, and each iteration is performed until, for a fixed initial neighborhood, the system reaches fixation and we estimate the invasion probability. Figure 8.3 is a plot of the invasion probability against the migration potential of type B cells assuming zero migration potential for type A cells, $k_A = 0$.

To understand the behavior of the variations in λ, we then changed the values of λ for several migration potentials k_B, and plotted these against the average invasion probability. A contour plot is presented in Figure 8.4, clearly indicating that the proliferative potential plays an important role along with the migration potential. Another interesting and salient

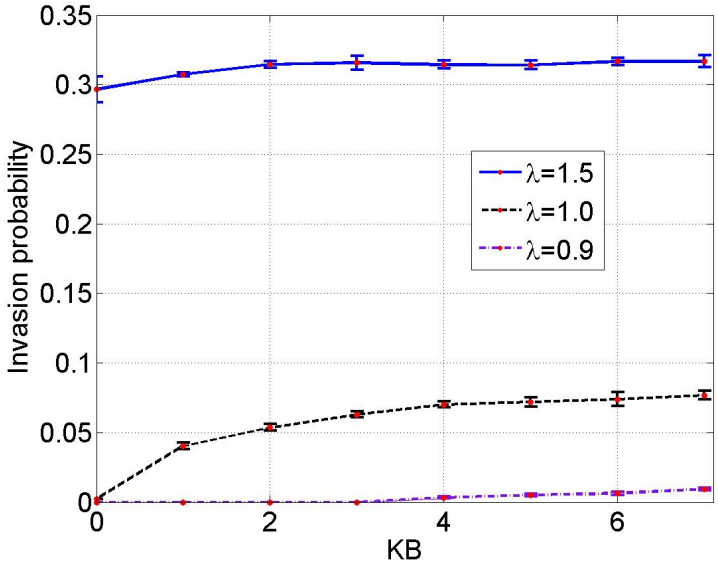

Figure 8.3: Invasion probability of various mutants as a function of migration potential of type B mutant on an Unstructured mesh. Parameters: lattice size $= 21 \times 21$,$\lambda = 1.5, 1.0, 0.9, k_A = 0$.

feature is that, for a fixed migration potential and varying proliferative potential, the invasion probability increases and stays almost constant.

We now assume non-zero migrative potential for type A cells. Figure 8.5 displays the invasion probability against the migration potential of type B cells assuming that the migration potential of type A cells is non zero, $k_A > 0$. As before, the simulations were run for advantaged mutants ($\lambda = 1.5$), neutral mutants ($\lambda = 1.0$) and disadvantaged mutants ($\lambda = 0.9$). Additionally, a significant change was not observed in the invasion probabilities of mutants with either zero, or lower migrative potential of type A cells (results not shown here). This indicates that lower migration potentials of type A cells does not have a predominant impact on the fixation probability.

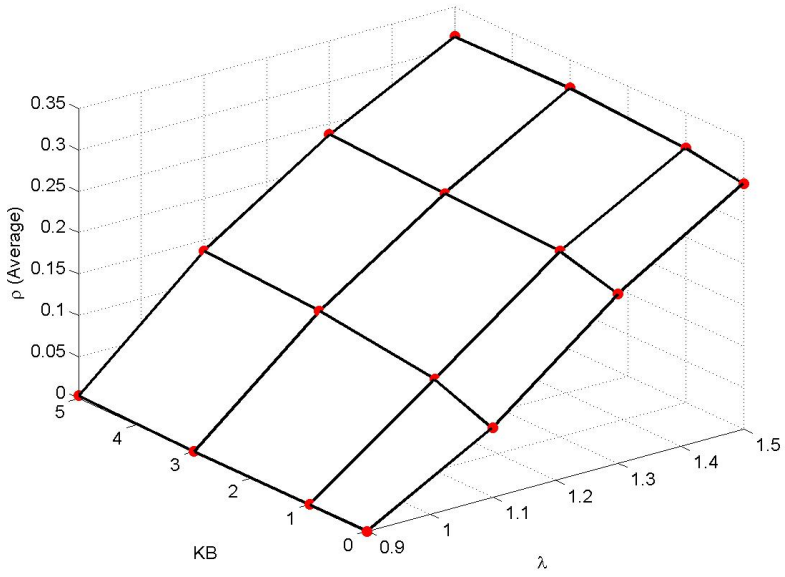

Figure 8.4: Contour plot of average invasion probability of various mutants against migration potential of type B mutant and proliferative potentials λ on an unstructured mesh. Parameters: lattice size $= 21 \times 21, k_A = 0$.

From Figures 8.3 and 8.5, we observe that in the absence of migration, i.e. when $k_A = 0$ and $k_B = 0$, the invasion probability is 0.2969, which is close to the fixation probability of the classical Moran process 0.3333. The small change can be attributed to either computational errors or to the geometry of the mesh. Also, the nodes located at the boundary may play an important role because of lesser number of neighbors (which can be interpreted as connectivities) associated with these. Another interesting observation is with respect to the neutral mutants. In Figures 8.3 and 8.5, for the scenario $\lambda = 1.0$, i.e., when $r_A = r_B$ and for $k_A = k_B$, the invasion probability is almost equivalent to (i.e., the value is of the same order as) the fixation probability for a system (in the absence of boundary effects) with neutral drift which is $\rho_{\text{neutral drift}} = 1/N = 0.0022$. From Figure 8.5, the

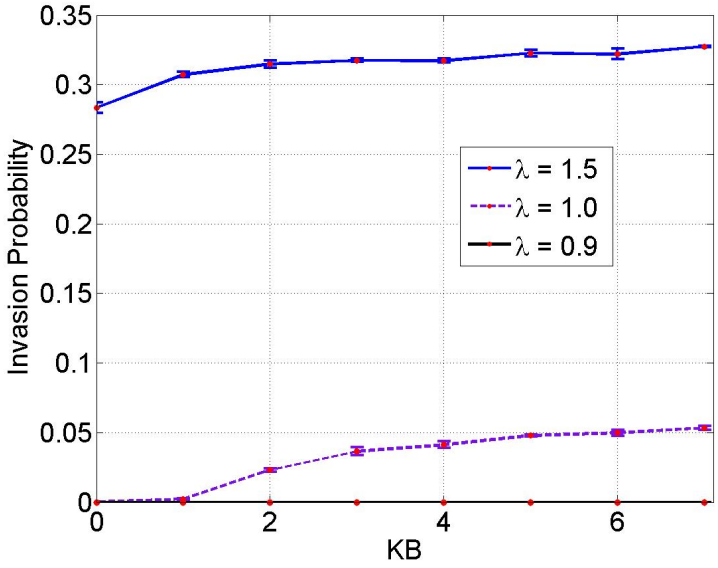

Figure 8.5: Invasion probability of various mutants as a function of migration potential of type B mutant on an unstructured mesh. Parameters: lattice size $= 21 \times 21$,$\lambda = 1.5, 1.0, 0.9, k_A = 1.0$. Notice that invasion probability is very small when $k_B \leq k_A$, and it is also vanishingly small in the case of disadvantaged mutant $\lambda = 0.9$.

change in the invasion probability is clearly observed around the point $k_A = k_B = 1.0$, for a neutral mutant (i.e., $\lambda = 1.0$). Clearly, we observe the two regimes for a neutral mutant, i.e $k_B < 1.0$ and $k_B > 1.0$. For $k_B < 1.0$, the invasion probability is very small and close to zero, while we observe a non-zero invasion probability in the regime $k_B > 1.0$. Thus, the change in the invasion probability around neutral mutant is very much apparent from the figures. The aforementioned changes in the fixation probability can be associated to the asymmetric nature of migration rates between type A and B cells. This suggests strongly that migration affects the system unless there is a higher rate of migration advantage to the mutant cell as compared to the host cell. The invasion probability is vanishingly small

for disadvantaged mutants in the presence of migration of type A cells, which is captured in Figure 8.5.

In order to compare the results with a 21×21 lattice that has 441 nodes, we designed an unstructured mesh consisting of 441 elements. In order to make a fair comparison with a lattice, we estimated the average number of neighbors for an unstructured mesh that has 441 elements. A set of sample realizations for an unstructured mesh was taken to obtain the average number of neighbors for a node, which was approximately 6. We took this number 6 as the nearest number of neighboring locations for each nodal point on a lattice on which a cell can give birth or migrate. The geometry of the neighborhood of a node on the lattice is the von-Neumann neighborhood along with 2 diagonal nodes. Figure 8.6 displays a comparison of the invasion probabilities on an unstructured mesh and on a lattice with parameters $\lambda = 1.5$ and $k_A = 0$. Although the difference between the invasion probabilities of lattice and mesh are not significantly different, however, this plot indicates that the lattice results overestimate the invasion probability. It is clearly evident that the difference in fixation probability grows with the migration parameter k_B. It should be noted that for a high fitness advantaged mutant ($\lambda = 1.5$), the cluster expansion of mutants is increased, resulting in a non-significant or minimal effect of migration potential on the invasion probability, i.e., the migration mechanism is dominated by the proliferation mechanism. Therefore, we observe that the migration potential of mutants has a very minimal effect on the invasion probability for high fitness advantages. Figure 8.7 displays the evolution and invasion of one type B cell to an absorbing state, i.e. containing all type B cells on an unstructured mesh. A blue color (dark in black and white) indicates normal or type A cells and a red color (light in black and white) denotes pre-cancerous or mutant cells (i.e. type B cells).

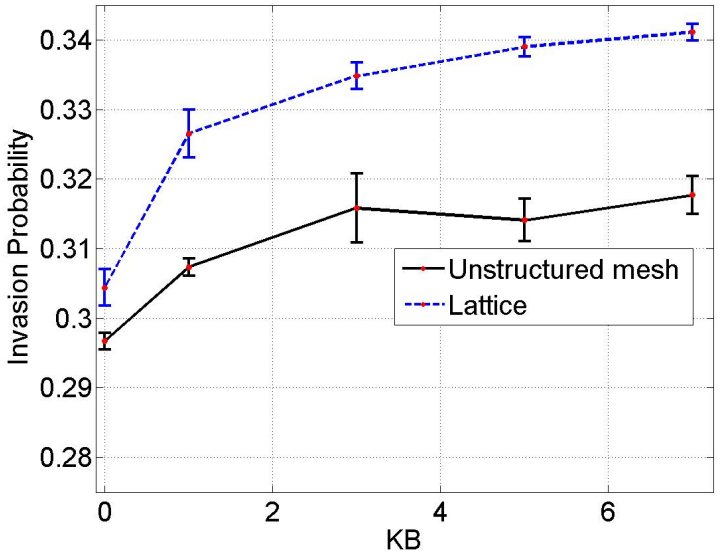

Figure 8.6: Comparison of Invasion probabilities: Unstructured mesh vs. Lattice. The average number of neighbors for the lattice are chosen to be approximately 6, i.e., the von-Neumann neighborhood along with diagonal nodes. Parameters: lattice size $= 21 \times 21$,$\lambda = 1.5, k_A = 0$.

8.2.4 Lattice boundary effects on invasion

We now explore the boundary effects on the invasion probability. This experiment is carried out by first constructing a 21×21 regular square grid. Instead of randomly placing a pre-cancerous cell on the grid, we fix its position on the boundary. Our system is now filled with 440 type A or host cells placed at every location and one type B cell placed on the boundary. The algorithm outlined in previous chapter is applied using reflecting boundary conditions, and each iteration is performed until, for a fixed initial neighborhood, the system reaches fixation and we estimate the invasion probability.

The variation in the invasion probability as a function of the initial location of type B

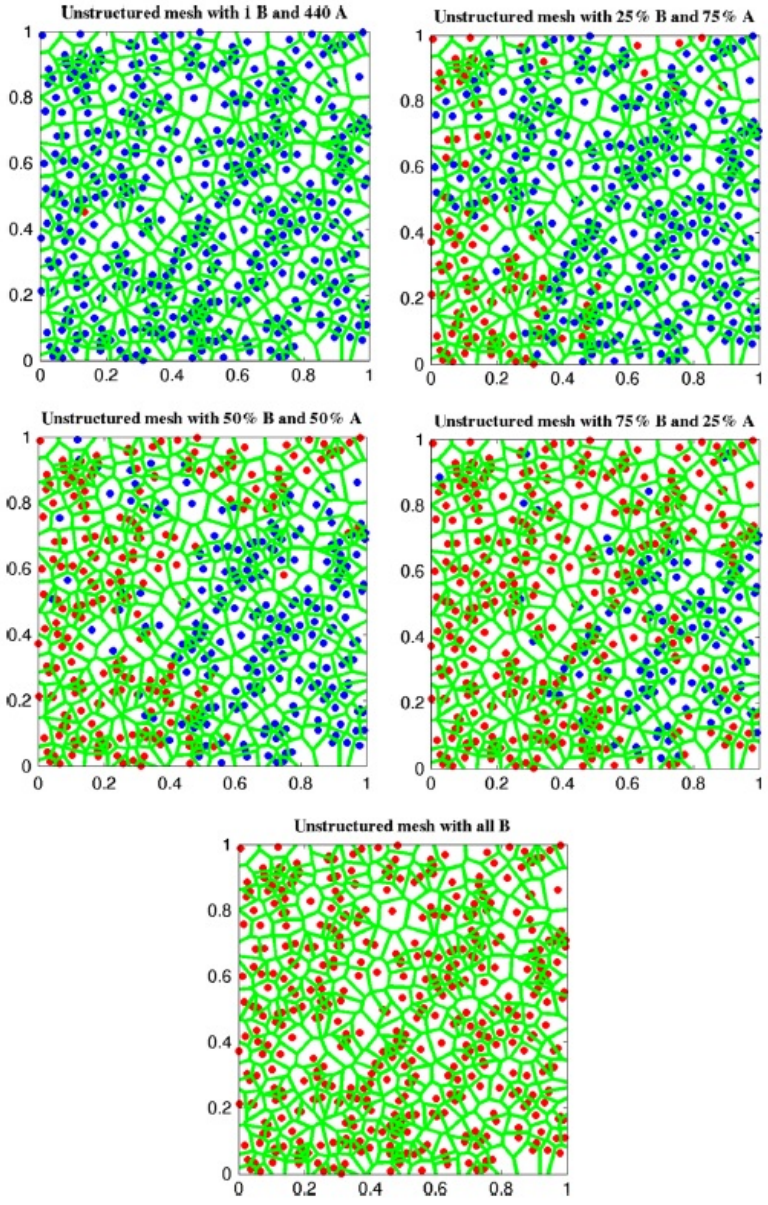

Figure 8.7: Spatial evolution of mutants on an unstructured mesh.

cell, in particular, at the boundary is investigated. A lattice of 21×21 cells was constructed in such a way that the position of the type B cell was fixed at $(i, i) = (1, 1)$, while the rest

of the lattice was filled with type A cells. We then changed the initial position of the B cells along the diagonal, i.e. $(i, i) = (2, 2), \ldots, (11, 11), \ldots, (21, 21)$. A sample scenario in which migration of A cell is zero, i.e. $k_A = 0$, and $\lambda = 1.5$ is chosen for this experiment. We observe that the invasion probability is much smaller when compared to that at the center of the lattice. It should be noted that there is a sharp increase in the invasion probability when the initial position of the B cells is changed from $(1, 1)$ to $(2, 2)$, which remains almost constant as the initial position is moved to the center of the system $(11, 11)$. Additionally, it follows an identical pattern as observed in the previous case till it reaches $(21, 21)$. Figure 8.8 displays the boundary effect for advantaged mutants and for various values of initial position of mutants in the system. Other scenarios with neutral and disadvantaged mutants, $k_A > 0$, were also investigated and similar behavior was observed for the invasion probability. This clearly suggests that boundary effects have a predominant influence on the invasion probability. This is in agreement with the earlier $1D$ results reported in [**?**].

8.3 Short summary

One of the less understood and the most intriguing phenomena is the invasion mechanism of pre-neoplastic lesions, that invade to its proximal tissue or to distant organs (termed as metastasis). The biological mechanisms that govern invasion probability of a mutant phenotype are still unclear due to the variations in tissue properties that effect the cells. Also, several important factors are over shadowed by other forces in the system, due to which some of the questions are still unanswered. In order to understand the invasive potential of mutants better, we consider only two genetic factors that predominantly effect the invasiveness of a cell which are proliferation and migration.

We have presented a computational approach to investigate an important but poorly

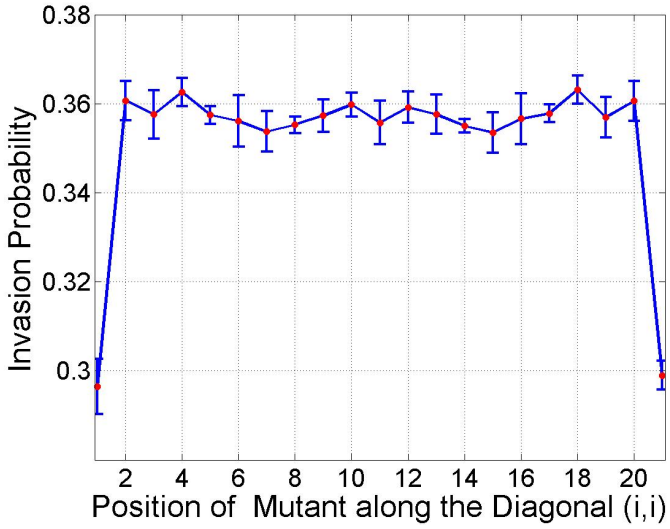

Figure 8.8: Boundary effect on a Lattice: Invasion probability against the position of B mutant. Parameters: lattice size $= 21 \times 21$,$\lambda = 1.5, k_A = 0$.

understood phenomenon, phenotypic heterogeneity, which appears to be highly prevalent during various stages of tumor growth. The existence and adaptability of pre-cancerous cells with different fitness rates in human tissues is still far from an established fact. Thus, we formulated a simplified scenario and investigated mutant dynamics with only two phenotypes in our system under a confined tissue geometry. We have attempted to understand the effect of tissue geometry on the invasion probability by generating a random set of neighbors for each node on a regular grid. Also, we have focused on the use of unstructured meshes that we believe captures features of real tumors that structured meshes fail to do, and have analyzed the resulting invasion dynamics of mutants. Our model is a generalized version of existing models and better captures the results on invasion dynamics.

We obtain some insight into the effects of the randomness of neighborhood sizes on the invasion probability in a migration free system. As noted previously, the invasion

probability is negatively correlated with the width of the distribution of neighborhood size. An increase in the distribution width of the neighborhood size can completely eliminate the advantage given by an increased proliferative potential of mutants, making them behave as if they were neutral mutants. These results provide further justification for us to conjecture that tissue geometry plays an important role in the invasion dynamics of pre-cancerous cells within a confined region.

The resulting graphs from this experiment confirm that the invasion probability is much smaller on unstructured meshes compared to a regular grid. Interestingly, for the scenarios in which $k_A = 0$ and $k_A = 1.0$, and for a given $\lambda = 1.5$, we observe minimal effect on the invasion probability. This indicates that smaller migration potentials of the host cells has a smaller effect on the invasion probability. For a neutral mutant, we notice a significant change in the invasion probability for the scenarios $k_A = 0$ and $k_A = 1.0$. However, when the ratio of the proliferative potentials is altered for various migration potentials, there is a huge effect on the invasion probability.

One of the results worth highlighting is the effect of the boundary on lattices. This is done by fixing the position of a B cell in the system at $(i, i) = (1, 1)$ and varying its position along the diagonal. This resulted in the invasion probability being smaller when compared to the invasion probability of a B cell placed at the center of the system. As the position of the B cell is moved inwards from the boundary, the invasion probability increases.

We anticipate that our results can be used to better understand some fundamental mechanisms in carcinogenesis. This includes the effect of the tumor micro-environment, which can affect the reproductive and migrative potentials of cancer (and pre-cancerous) cells. Our model can be extended to include the randomness of fitness and migration potentials, as a result of heterogeneous tumor micro-environment and for distinct cell

phenotypes (which is addressed in the next chapter). Additionally, several biological studies support the fact that the epithelial-mesenchymal transition (EMT) is a critical stage in metastasis, when cells acquire migrative potential [1]. Our computational methodology may be applied to address questions related to this biological phenomena. For instance, we have shown that the invasion probability depends on the width of the distribution of neighbors. This computational study can be validated experimentally by inducing cells to undergo EMT, and measuring the invasion probability for various tissue architectures (i.e. using different cell lines). In addition, we have observed that increasing migration potential (for example, due to EMT) has a significant effect if proliferative potential is around the neutral drift. This prediction can be tested by again inducing the cells to undergo EMT in different micro-environmental conditions (for example, under normal and hypoxic or acidic conditions). Finally, our results confirm that distortion of the tissue architecture and control of migration potential of pre-cancerous cells can reduce tumor progression to some degree (which can be applied in the study of anti-cancer therapies induced secondary malignancies). The invasion of pre-cancerous cells may be controlled by a therapeutic intervention that can control the geometry of the tissue architectures. For instance, several experimental studies have suggested that morphological changes in the breast tissue promotes (breast) cancer to some extent. This change in tissue can be controlled by an agent that can inhibit the metabolic pathways that change tissue architecture.

Chapter 9

Effect of Site Dependent Fitness on Invasion Probability

9.1 Introduction

The effect of spatial structure and heterogeneity is known to be of significant importance in evolutionary models, including evolutionary biological models and social networks (see [167]-[168]) and references therein). The structure of the network might have subtle effects on the dynamical properties and salient features of the model. One of the most important results obtained from these models is the fixation (also called invasion) probability. Invasion probability is defined as the probability that a species (for example, a mutant) can take over the whole population in the system. Depending on the structure of the graph, the invasion probability can either be suppressed or enhanced and amplified. The question of how the structure of the network affects fixation has been the subject of much research. Maruyama showed that, on regular graphs the fixation probability is the same

as on unstructured model [148]-[149]. Lieberman et al. [151] generalized this observation to a more general set of graphs known as isothermal graphs. Many authors discussed heterogeneity of the spatial structure and its impact on the fixation probability (see Manem et al [170], Sood et al [168], Houchmandzadeh et al [152]). Sood et al. [168] showed that upon introduction of randomness in a scale-free random graph the fixation probability is significantly suppressed. Other papers have suggested particular configurations in fact enhance the fixation probability [151]. Recent work by Thalhausser et al.[159] and Manem et al. [170] on structured and unstructured meshes and random graphs showed that spatial structure influences the fixation probability to a greater extent for mutants with migration potential. Although a great deal of research has been devoted to heterogeneity of networks, less effort has been devoted to a study of heterogeneity due to spatial fitness distribution and environmental stress and its effect on the invasion probability. Spatial variation of fitness, however, is a critical parameter in modeling biological and social systems as the fitness of species strongly depends on the micro-environmental parameters which cannot be ignored. For example in models of bacterial growth, fitness can be a function of spatial distribution of nutrients, in social networks it can represent the geographical biases (see [171] for models of election). In the evolutionary dynamics of cancer, tumor progression is known to be strongly affected by the tumor micro-environment. In this paper, we focus our attention on modeling the tumor micro-environment during cancer progression although we shall point out other practical applications in other contexts, as well.

In cancer a single mutated cell proliferates and evolves into a neoplasm which progresses and develops into a tumor. New mutant cell types appear as a result of intrinsic genetic instabilities and environmental pressure from tumor the micro-environment that stimulate epigenetic changes and are believed to play a major role in cancer progression into metastasis [1]. Genetic changes (mutations) that occur spontaneously during DNA replication and

result in a change in the genetic code. Epigenetic changes are those changes that can be attributed to the variations in the functionality of its genome. Micro-environmental factors that contribute to these changes can be lack of resources, as well as the micro-environment such as it's acidity, hypoxic state and vascular heterogeneity. The micro-environment can act as a refugee for some species (i.e. permit co-existence of various species), or can facilitate fixation of a single species. The evolutionary dynamics of such a population in a highly diverse environment is very complex, and does not follow traditional explanations using equilibrium or quasi-equilibrium approaches. The changes in the environment reflect the diversification of the morphology. Depending on the variations in the spatial heterogeneity, there might be several scenarios that can be exhibited by the system, namely, zero absorbing state, or fixation by the dominant species, or co-existence.

Phenotypic heterogeneity is a key regulator in cancer and is highly prevalent during carcinogenesis, too. Several systematic investigations have suggested that the morphological diversity within a tumor can be due to metabolic functions, availability of nutrients (such as oxygen, etc) or, micro-environmental stresses. A highly heterogeneous micro-environment leads to a population comprised of diverse pre-cancerous phenotypes. The fitness of various cancerous phenotypes is dictated by genetic, epigenetic factors and in particular, the host environment. Various selection forces confer a selective fitness advantage to a particular mutant phenotype compared to other sub populations in the tissue. These selection forces change spatially and also temporally during the evolution of tumors. There are several modifications that might occur in various therapeutic interventions, (namely, chemotherapy agents and nano-drug delivery). Due to non-homogeneous distribution of drug delivery, cells spontaneously may adapt to the drug and become therapy resistant. This also dictates the existence of diverse species and the variations in the division rates. Although migration potential is important, all of the above situations can arise in a migration free

system too.

In cancer biology, migration is considered to play a vital role in the invasion of neighboring tissue as well as in metastasis. Although cellular motility and cell migration are not (quite) identical terminologies, in this work we assume both are equivalent. Also, numerous experimental investigations have suggested that in the final stages of carcinogenesis, cells undergo a transition to become more motile (the so called the Epithelial-Mesynchemal transition (EMT) [1]), and this new phenotype with higher migration potential escapes from the system and colonizes a different organ. Thus, a relevant and interesting challenge is to understand the interplay of migration potential and heterogeneous (fitness) distribution of mutants. However, as far as the authors are aware this problem has not been addressed in any evolutionary graph theoretical model of evolution to date. This scenario is also addressed in the later part of this work. We show that the interplay of spatially distributed fitness and the capability of individual migration leads to non-trivial results for the invasion probability.

In this section, we address several challenging questions related to the interplay between different types of spatial random fitness distributions such as uniform, triangular, bi-modal (in the presence and absence of migration) on the fixation probability. It should be noted that we have explored the invasion dynamics only for spatially heterogeneous systems which are independent of time.

Many authors have studied the spatial dynamics of cancer invasion using cellular automata models [162]—[165], and have incorporated progressively more complex cellular mechanisms. In these types of models, it is very likely that the effects of some forces on the underlying invasion dynamics are obscured by other dominant forces. In an attempt to understand and analyze the underlying dynamics, we consider only two forces that influence the inherited genetic behavior of a pre-cancerous cell. This is an extension of the work

of Komarova et al. [159], which focused on the invasion dynamics of pre-cancerous cells on a structured lattice in the framework of Moran processes. This work was later extended by Manem et al. [170] who investigated the effect of migration (on random and unstructured meshes) on the invasion probability, which had not been investigated in previous modeling efforts to understand cancer progression on more realistic tissue architectures. The authors also investigated the fixation probability as a function of the width of the distribution used to construct the random graph and observed that the fixation probability decreases as the width of randomness increases. The problem of fixation in random spatial structures has been discussed in detail in the literature, nut most of the existing models, rely on a weak selection limit of a voter model (see [168] for example).

Authors in [159] found that the fixation probability of the motile phenotype is enhanced, and is critically important near the neutral limit. The work reported in [170] confirmed the above findings on random structures and analyzed how the randomness of the graph, and the migration potential of mutants compete with each other. Our model shows a lot of resemblance to the phenotype switching model, in which replicative and migrative phenotypes stochastically switch between each other [172].

9.2 Results

9.2.1 Effect of randomness (with zero migration)

In this section, we investigate the effect of randomness of mutants (instead of random spatial architectures) in a system, i.e. when one or both of the two phenotypes has random fitnesses from a given distribution, which is considered to be more realistic scenario. As discussed in the previous section, our focus is on the spatial fitness distribution. The effect

of temporal random fitness has been discussed previously in the literature on population genetics (see [173]).

Our model in this section, however, assumes that the variation in the fitness rates is due to a quenched randomness spread over the spatial structure, which does not have any dynamics. This can represent cases where environmental effects such as the distribution of nutrients (or, any other agent for instance resistance to chemotherapeutic drug) can affect the local fitness of an individual phenotype. For example, in the absence of some hormones (growth factors) which are distributed spatially, cells might enter quiescent states thus indicating a lower fitness. In the case of cancer cells it is believed that spatially distributed oxygen and acidity might affect the aggressiveness of cancer cell phenotypes. In models of bacterial growth, this can be due to the lack of nutrients in local habitats.

We investigate the effect of random proliferation of A and B cells, separately, on the invasion probability for zero migrative potentials (for both types of cells). We explore various types of random fitness distributions. Figure 9.1 displays different types of fitness distributions chosen for the numerical experiments: uniform, triangular ($D = [0.9, 1.25]$, $D = [0.75, 1.1]$) and bi-modal. The critical question in this experiment is to analyze if the selection dynamics depends on the shape of the fitness distribution (i.e. uniform, triangular and bi-modal). We use the algorithm outlined in the previous section and run 5 sets of simulations of 10000 iteration each. Each iteration is performed until the system reaches one of its absorbing states (either all B's or zero B's).

9.2.2 Random fitness of mutants

In this section we investigate the effect of variance of the fitness of the mutant cells (B cells) on the invasion probability. This is carried out by assuming a fixed fitness for type A cells,

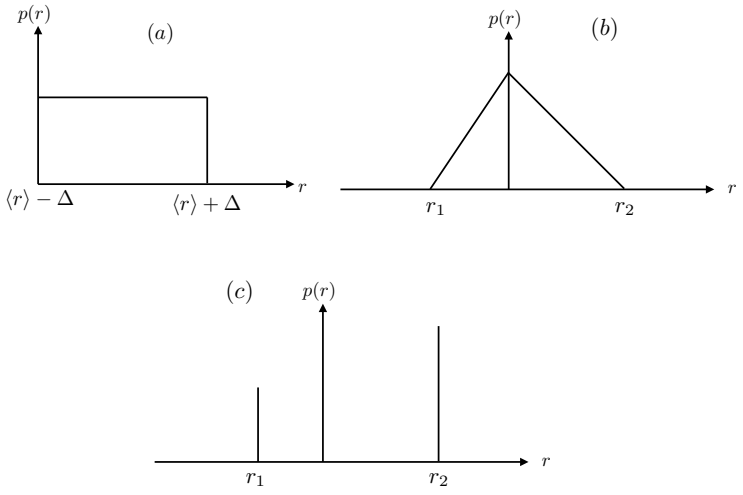

Figure 9.1: Different forms of random fitness distributions: a) Uniform b) triangular c) bi-modal.

which does not depend on the environment (lattice sites). Also, we take the type A cells fitness as the reference fitness (by assuming it to be equal to 1). As indicated in Fig.9.1 (a) fitness of B cells in this case, follows a uniform distribution where $\langle r_B \rangle - \Delta < r_B < \langle r_B \rangle + \Delta$.

For this, we construct a regular grid consisting of $21 \,\mathrm{x}\, 21 = 441$ elements with reflecting boundary conditions, and fix the fitness rate of A cells, i.e. $r_A = 1.0$. We then randomly generate fitness rates for B cells at each nodal point on the lattice such that the average value is $r_B = 1.5$ for advantageous mutants and $r_B = 1.0$ for neutral mutants, and fix this fitness matrix for all the iterations. We fill the lattice with type A cells at each nodal point on the grid, and randomly place a mutant in the system (by deleting an A cell). So, the system is now comprised of $N-1$ type A cells and 1 type B cell. The algorithm outlined in the previous section is applied with reflecting boundary conditions until the system reaches one of its absorbing states. Figure 9.2 shows the effect of varying the distribution width of r_B on the invasion probability for advantageous mutants.

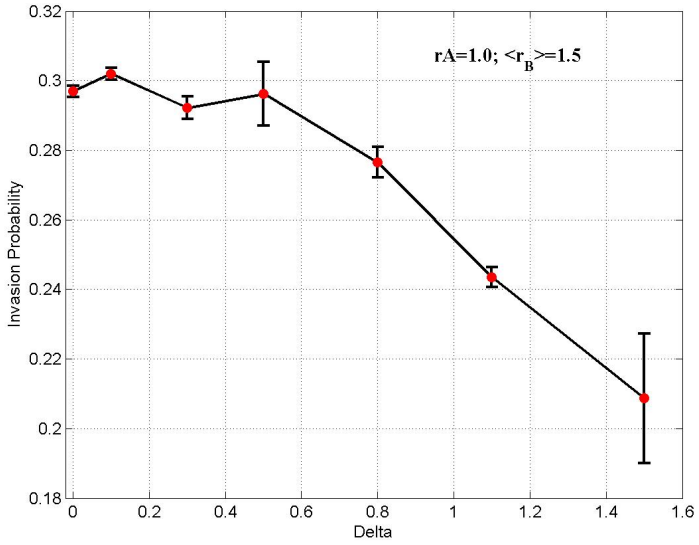

Figure 9.2: Invasion probability of mutants as a function of varying distribution width of fitness r_B. Parameters: Lattice size=21 x 21; $r_A = 1.0$, $\langle r_B \rangle = 1.5$, $m_A = m_B = 0$

From Figure 9.2, we observe that the invasion probability negatively correlates with the width of the distribution, i.e., as the width of the fitness distribution of type B cells, $\sim \Delta$, increases, the invasion probability decreases for advantageous mutants. In Figure 9.2, we do not observe a huge impact on the invasion probability till the value of Δ is 0.4-0.5. Once the Δ value increases across the threshold of 0.4-0.5, i.e. relatively small width, we notice a decline in the invasion probability. At the lower end of the uniform distribution, i.e. $\langle r_B \rangle - \Delta$ reaches $r_A (= 1)$ one can see that the fixation probability begins to decrease at a much more significant pace. This indicates that as the number of sites where B cells are *disadvantaged* is introduced in the system, the fixation probability decreases accordingly. (Notice that the drop has almost a linear form but this may well be an artifact of the finite size of the system used in the simulation.)

For a high variance of distribution width, we can intuitively imagine the existence of various types of B cells (with different fitness rates) which are competing against each other, and also against type A cells in the system. Due to the intense competition between various type B cells, and also against type A cells, it becomes hard for mutants to survive, resulting in a sharp decline in the invasion probability for higher variance of r_B. There have been several experiments on random migration from the context of metastasis [182], however these results can act as a pathway for further biological investigations into the effect of random fitness of mutants on the invasion probability.

The system with zero fitness width can be understood as a well oxygenated and well suited environment for proliferation of mutants at each point in the tissue. The increase in the variance of the distribution can be interpreted as the system having harsh micro-environmental conditions (for instance scarcity of resources, spatial and temporal changes in nutrients). Due to varying fitness rates at each point, several mutants (with different fitness rates) arise in the system and compete against each other, and also with the host cells, to take over the whole tissue. Increasing the variance implies increasing the number of different mutant phenotypes in the system competing against each other to take over the whole tissue, and thus results in a decline in the invasion probability.

Figure 9.3 displays a plot of varying distribution width of r_B on the invasion probability for neutral mutants.

For a zero distribution width, we obtain a value of the invasion probability approximately equal to the value of the space free fixation probability ($\rho = 1/N = 0.0022$). Although the simulations were run for a large number of iterations, we do observe an increase in the invasion probability for $\Delta \sim 0.1$ and 0.2, which can be attributed to numerical errors in the simulations. As the variance of the distribution increases, we notice a decrease in the invasion probability which quickly approaches zero for a Δ of 0.4-0.5. Biologically,

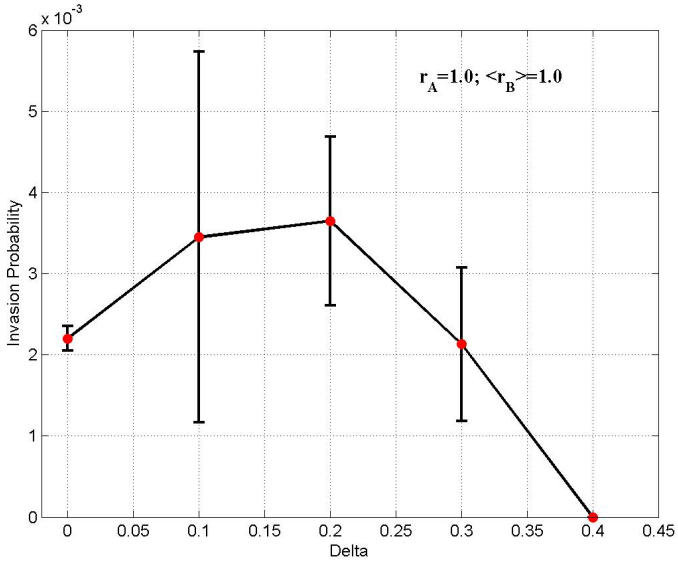

Figure 9.3: Invasion probability of mutants as a function of varying distribution width of fitness r_B. Parameters: lattice size=21 x 21; $r_A = 1.0$, $\langle r_B \rangle = 1.0$, $m_A = m_B = 0$

if a tissue is comprised of various types of B phenotypes having an average value of 1.0, then these phenotypes have to fight against each other along with the neutral host cells. This competition to invade the whole tissue declines as the number of type different B phenotypes in the system increases (with the increase in variance).

9.2.3 Random fitness of host cells and mutants

In this section, we investigate the effect of random fitness distributions for both types A and B cells. We chose the fitness distribution width for type A cells to be $D = [0.9, 1.1]$ with average value to be $r_A = 1.0$, and varied the distributions for type B cells. Figure 9.4 displays a plot of invasion probability against the variance of r_B for advantageous mutants whose average value is 1.5. We notice that as the variance of type B cells increases, the

invasion probability decreases. Although, it is interesting to note that from Figures 9.2 and 9.4, for a Δ-value of 1.5, the value of $\rho = 0.2087$ and $\rho = 0.2165$ for non-random and random fitness rates of type A cells, respectively. For a distribution width of 0.1 away from the average fitness value of A cells, we do not observe a huge change in the invasion probability when compared to non-random fitness rate of A cells (see Figure 9.2). Probably, the effect of random fitness rates of type A cells on the invasion probability

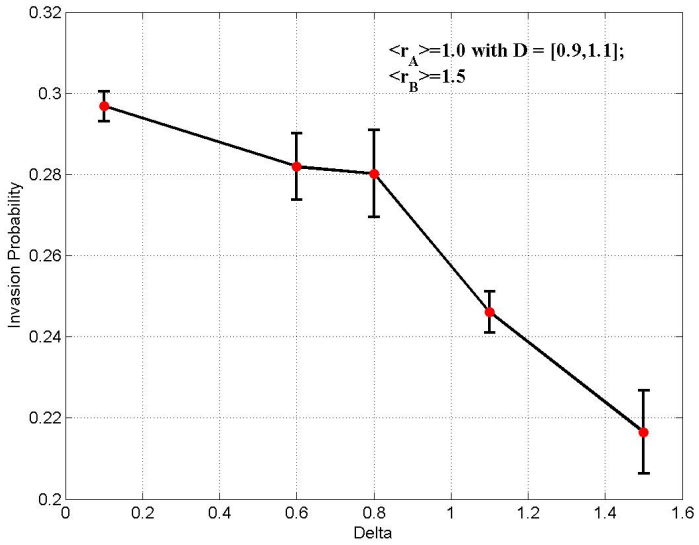

Figure 9.4: Invasion probability of mutants as a function of varying distribution width of fitness r_B. Parameters: Lattice size=21 x 21; $\langle r_A \rangle = 1.0$, $\langle r_B \rangle = 1.5$, $m_A = m_B = 0$

might be clearly observed if the width is increased to a larger value. The randomness of types A and B cells in the system can be taken to characterize normal and pre-cancerous cells, whose fitness rates change at each point in the tissue. From our results, we observe that a small change in the fitness rate distribution of host cells does not have much impact on the invasion probability.

Another interesting observation is that even though one intuitively expects that as the distribution of A cells broadens towards a more advantageous states and as the distribution of B cells broadens towards a less advantageous state, the point at which we observe a change in regime (bending of invasion probability) should be when the two distributions begin to overlap. As a matter of fact, this is not the case, and points to the fact that the underlying mechanisms are more sophisticated and non-trivial.

Figure 9.5 displays a plot of the invasion probability against the variance of r_B for neutral mutants whose average value is 1.0. As in the previous cases, we observe a negative

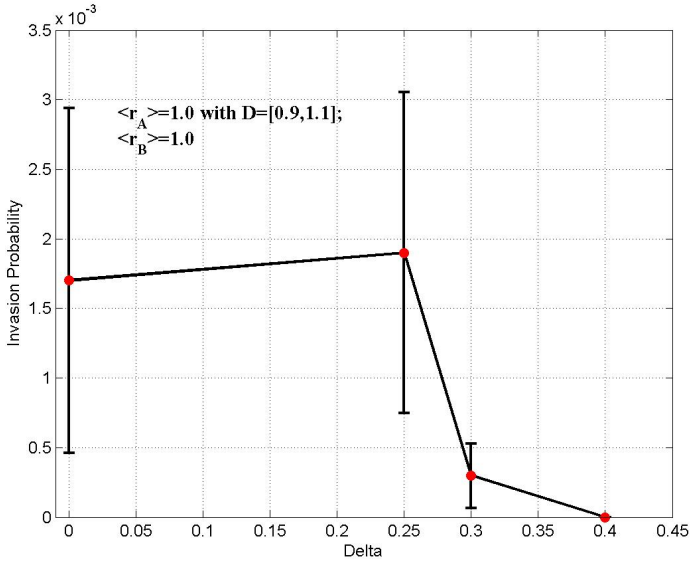

Figure 9.5: Invasion probability of mutants as a function of varying distribution width of fitness r_B. Parameters: Lattice size=21 x 21; $\langle r_A \rangle = 1.0$, $\langle r_B \rangle = 1.0$, $m_A = m_B = 0$

correlation of the distribution width of mutants with the invasion probability even in the presence of random fitness of host cells. It is also interesting to compare Figures 9.3 and 9.5, for a Δ-value of 0.3. We notice that the presence of random fitness of host cells

pushes the invasion probability (see Figure 9.5) to a smaller value compared to the absence of randomness of host cells (see Figure 9.3). This can be attributed to the competition between various types of host cells as well as with other mutants, resulting in a decline in the invasion probability. This is again due to the fact that the fraction of disadvantaged (i.e. $r_B < r_A$) type B cells increases in the system.

9.2.4 Special Case: neutral drift

In this section, we choose the fitness distribution width of neutral mutants to be a triangular distribution, and investigate its effect on the invasion probability. The fitness of type A cells is fixed to be $r_A = 1.0$. The choice of a triangular distribution lets us fix the mean value of both A and B cells to be the same (i.e. $r_A = r_B = 1$), while the median value of B can be greater than unity. We tested two scenarios to investigate if a neutral mutant can be pushed to an advantageous or a disadvantageous state for two sets of triangular distributions. We choose the triangular distributions in such a way that the average value of r_B equals that of r_A (although numerically it is close to but not exactly equal to 1.0).

The values of ρ for the two types of triangular distributions D1 and D2 are around 0 and 0.045767 respectively. This clearly indicates that a neutral mutant can be pushed either to an advantageous mutant state (if D= $[0.9, 1.25]$), or, to a disadvantageous mutant (if D= $[0.75, 1.1]$). The value of ρ in a space-free system is $\rho = 1/N = 0.0022$, and, on a structured grid $\rho \approx 0.00224$. However, if the system has fitness rates from a triangular distribution D2, then the invasion probability is increased by almost 95%. At the same time, if the fitness distribution is from D1, then the mutant loses its neutral drift and becomes a disadvantaged mutant, leading to zero invasion probability. As can be seen the effects are minor, but still observable in our simulations. These results can provide can

pave a way to some biological studies on random resources and their effect on the invasion dynamics.

Biologically, it is possible that fitness distributions may not always be uniformly distributed in the tissue. From our computational analysis, neutral mutants cannot be pushed to become advantageous mutants for a uniform fitness distribution. However, if the distribution is slightly changed to triangular, (i.e., the resources and nutrients vary according to the triangular distribution), then a neutral mutant can turn into an advantageous mutant. This is one of the plausible reasons why we might (or, might not) observe the invasion mechanism under harsh micro-environmental conditions for neutral mutants.

9.2.5 Bi-modal distribution

In this section, we focus on the existence of only two types of mutant phenotypes in the system along with host type cells, and their impact on the invasion probability (i.e. when the fitness response of the system to the environmental factors is binary). For example, cells can transition into a quiescent state in response to lack of nutrients, or due to a harsher environment (hypoxia, acidity, drug concentration in the case of cancer) thus reducing cell cycle times and fitness significantly. For this purpose, we choose the fitness distribution of mutants from a bi-modal distribution $D = \{0.5, 1.5\}, D = \{0.8, 1.2\}$ (with average 1.0), and fix the fitness of host type cells to be equal to 1.0. We construct the fitness matrix for mutants in such a way that the system is comprised of x per cent ($0 \leq x \leq 1\%$) mutants with advantageous fitness rate, r_2, and the rest with disadvantageous fitness rate, r_1. Figure 9.6 displays the plot of invasion probability against the percentage of mutant phenotypes with an advantageous fitness rate.

As seen from Figure 9.6, the invasion probability for the mutants is a function of the

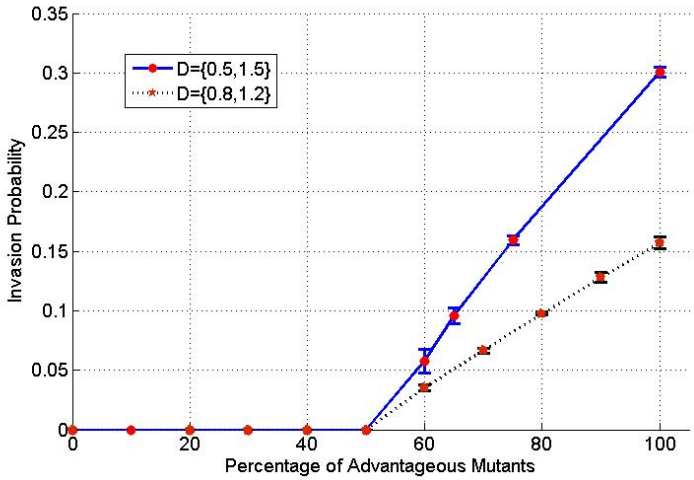

Figure 9.6: Invasion Probability against the Percentage of advantageous mutants. Parameters: Lattice size=21 x 21; $r_A = 1.0$, $m_A = m_B = 0$

percentage of advantageous mutants ($r_2 = 1.5$, or $r_2 = 1.2$), and is zero until the bimodal distribution reaches a point where more than half of the points in the lattice confer advantageous fitness. This can be understood by assuming a uniform and even distribution of the two fitness values (say, $r_B = 0.5$ and $r_B = 1.5$) on a square lattice (i.e. checkerboard distribution). Now, every advantaged mutant is merely one lattice site away from a fellow advantaged mutant, and upon one division event this gap is filled which gives (almost) connected regions of advantage to the mutants. A much lower abundance of sites with advantaged fitness values leads to separated islands inside which the average value of fitness would confer a fitness advantage for the mutants there. However, due to the distance between them, the chance to capture the whole system A system refers to a small niche (with a finite and small number of cells) would be extremely small.

In other words, a successful invasion of the system is possible if all different islands with advantaged fitness sites are tightly connected. Due to the construction of the death-birth

model the regions with on-site advantaged fitness can be one cell away from each other and still lead to a successful invasion. The fact that all the regions with advantageous fitness, (i.e. r_2 in Figure 9.1) should not be separated or found far from each other is illustrated in Fig.9.7 a. The ideal checkerboard distribution where every other site has an advantageous value of fitness for B cells is depicted in Fig.9.7 b.

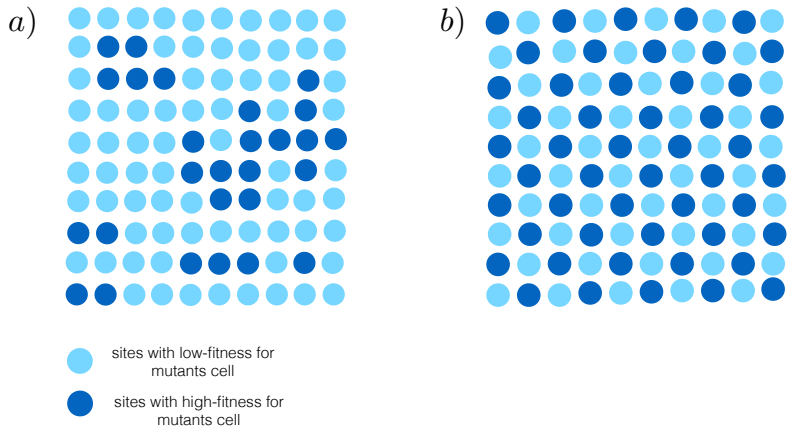

Figure 9.7: (a) Random distribution of two types of sites with high and low fitnesses for mutant cells. (b) Evenly distributed high and low fitness sites with equal ratios (ideal case). This is the onset of successful fixation.

In the case of a bi-modal distribution we can use a simple approximation especially in the weak selection limit. When r_1 and r_2, in the bi-modal distribution, are positioned at the same distance from $\langle r_B \rangle$, then the average value of the fixation probability can be replaced by the following Moran model formula:

$$\begin{aligned} \rho_{\mathrm{bi-modal}} &\sim 1 - \frac{1}{\langle r \rangle} \qquad (\Delta r \ll 1) \\ &\sim 1 - \frac{1}{r_2 x + r_1 (1-x)}, \end{aligned} \tag{9.1}$$

where r_1 and r_2 are the values of fitness, and x is the fraction of r_2 sites, i.e. disadvantageous sites. Figure 9.8 displays the comparison of invasion probabilities between analytical approximations and the simulated result. As can be seen for the case of $r_1 = 0.5, r_2 = 1.5$ where $\langle r_B \rangle = 1.5 \neq r_A$, the above simple approximation breaks down and the difference in error increases. We have also simulated for the scenario: $r_1 = 0.2, r_2 = 2.8$ (not shown here), and in this case we observed that the analytical approximation is no longer valid,

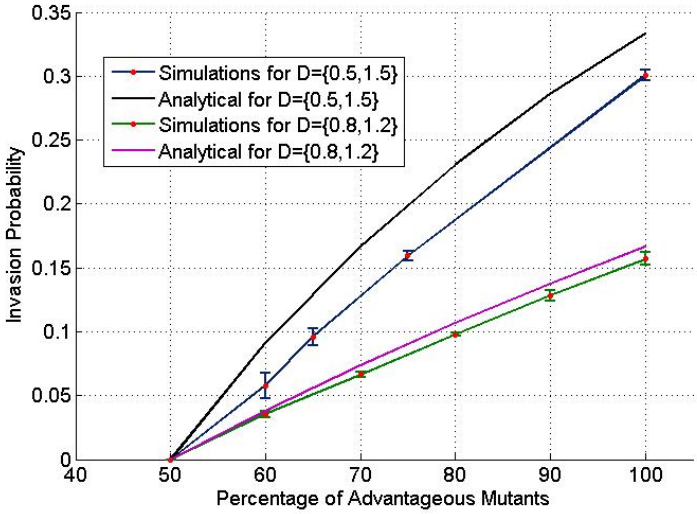

Figure 9.8: Comparison of invasion probabilities- Analytical and Simulated for various distributions

and the error increases between simulated and analytical values. This clearly indicates that as the width of the distribution increases, the average value $\langle r \rangle$ cannot be replaced by $r_2 x + r_1(1 - x)$, and computational simulations are required to estimate the invasion probability

During the early stages of carcinogenesis, host type cells can be interpreted as healthy cells, and the two types of phenotypes (from the Bi-modal distribution) can be character-

ized as two types of pre-malignant cells in the system. The existence of these two types of pre-malignant cells are based on several micro-environmental factors including acidity, hypoxia, epi-genetic or genetic changes. These two types of cells are understood to have two different fitness rates in the tissue. It is clearly evident from our analysis that the invasion probability will always be zero until the system reaches a particular threshold of advantageous mutants. Therefore, under harsh micro-environmental conditions, when the system is comprised of mostly disadvantageous mutants, the invasion probability is always zero. Hence, we conclude that there is a very minimal chance of mutants invading the neighboring tissue under these conditions.

9.2.6 Effect of Randomness: With Migration

In this section, we investigate the effect of migrative potential of mutants on the invasion probability for a random fitness distribution width of type B cells. This experiment is carried out in order to try and ascertain if migration reduces or amplifies the invasion probability. The migrative potential of host cells is assumed to be $m_A = 0$, while the migration potential of mutants is chosen to be $m_B = 1.0$ (low migrative potential) and $m_B = 5.0$ (high migration potential). Migration potential can be considered as 1/average migration time, and units of migration can be defined as the number of steps a cell movies per unit time. The algorithm outlined in Section 2 is carried out with reflecting boundary conditions, until the system reaches one of its absorbing states. Figure 9.9 displays the plot between the variance of distribution width of mutants against the fixation probability in the presence of migration.

From our computational analysis, it is clear that the migration potential of mutants amplifies the invasion probability. In Figure 9.2, we notice that in the absence of migra-

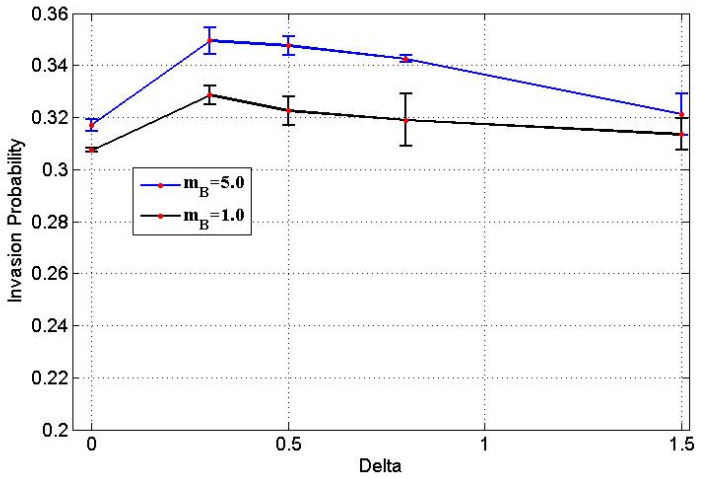

Figure 9.9: Invasion probability of mutants as a function of varying distribution width of fitness r_B. Parameters: Lattice size=21 x 21; $r_A = 1.0$, $\langle r_B \rangle = 1.5$, $m_A = 0$

tion, the invasion probability decreases as the variance increases, which is the opposite of Figure 9.9, wherein the invasion probability increases in the presence of migration. Invasion probability increases as the variance increases, but almost stays constant for larger variances.

This corresponds to an interesting biological phenomena in real tumors. Many authors have experimentally claimed that migration and proliferation are two sides of the same coin, and they counteract one another in the system [183]. In some solid tumors such as in-situ tumors, where the migration potential of cells is close to zero, the invasion probability decreases under harsh micro-environmental conditions (see Figure 9.2). However, during carcinogenesis, as mutants or pre-malignant cells acquire migrative potential, the invasion probability is amplified even under severe micro-environmental conditions (see Figure 9.9).

A similar experiment is carried out for neutral mutants, by varying the distribution

width of mutants in the presence of migration. Figure 9.10 displays a plot of invasion probability against the variance of fitness distribution of type B cells. A similar behavior is observed as in the previous plot. The invasion probability is amplified in the presence of migration even for neutral mutants, and stays almost constant for an increasing distribution width. This suggests that under harsh micro-environmental conditions wherein the supply of oxygen and nutrients is limited, (i.e., all mutants in the system have fitness rates around the neutral drift), migration plays an important role in the invasion of the adjacent tissue or even in EMT phenomena (in which cells metastasize to distant sites).

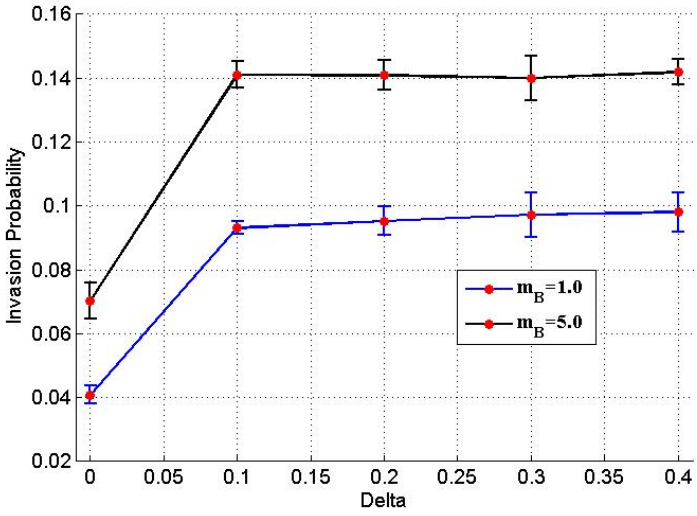

Figure 9.10: Invasion probability of mutants as a function of varying distribution width of fitness r_B. Parameters: Lattice size=21 x 21; $r_A = 1.0$, $\langle r_B \rangle = 1.0$, $m_A = 0$, a) m_B=1.0 and 5.0.

9.3 Short summary

We have presented a computational framework to understand the effect of the tumor micro-environment on the invasion probability of pre-malignant cells. A biological phenomenon that is not well understood is phenotype heterogeneity during the process of carcinogenesis. Several experimental studies have suggested that tumor growth dynamics is quite different in a heterogeneous micro-environment compared to a homogeneous environment. In a heterogeneous environment, the tumor growth (either in the early or later stages) is affected by several factors such as nutrients, oxygen concentration, acidity, extra-cellular matrix (ECM), etc. This clearly indicates the importance of studying the invasion dynamics, (i.e. either invasion to neighboring tissue or metastasis), under harsh micro-environmental conditions. We have considered cellular automata rules based on biological assumptions, and not imposed them in order to obtain interesting salient features of the model. Thus, we have developed a simplified model that has two types of phenotypes in the system, namely host cells and mutants. The reproductive rates of both host cells and mutants might differ due to several micro-environmental conditions. For example, the division rate of a phenotype can be reduced due to the rigidity of the tissue, or due to lack of nutrients at that position. Also, the division rates for both the host cells and mutants can be quite different in real tumors. Our computational model encapsulates these into a spatially distributed random fitness of mutants as well as the host cells in the presence and absence of migration, to examine their impact on the invasion probability.

We have also investigated the effect of random fitness distribution widths of advantageous and neutral mutants (in the absence of migration) on the invasion probability. We observed that the invasion probability decreases as the variance of fitness distribution increases. A fitness distribution with zero width (which can be characterized as a well oxy-

genated system) has a higher invasion probability (which can be understood intuitively) compared to a non-oxygenated system. However, as the variance of the fitness distribution increases, (i.e. under harsh micro-environmental conditions) the invasion probability decreases. This is justifiable due to the intense competition between various mutants (that emerge due to changes in the environment), and also competition with the host cells to invade the system.

We also focused on the impact of the invasion probability, due to a random fitness distribution of both the host cells and also mutants, on a migration free system. As noted in the previous scenario, the invasion probability negatively correlates with the fitness distribution width of the mutants. It is also quite interesting to note that there is no significant difference between the invasion probabilities in the presence and absence of random fitness of host cells. This can be attributed to less randomness (with width one away from the average value) of host cells in the system, which behave in a similar fashion to a distribution of zero width.

Several biological experimentalists have suggested that the harsh micro-environmental conditions can facilitate an increase or a decrease in the invasion mechanism of mutants. This biological phenomenon is very crucial in the metastatic process. To understand this mechanism, we tried to investigate the conditions (if they exist) that amplify and weaken the invasion probability. For this purpose, instead of choosing the fitness matrix of mutants from a uniform distribution, we preferred a triangular distribution with average as neutral drift. It is quite interesting to note that for various distributions, the neutral mutant can be amplified to an advantageous mutant or weakened to a disadvantageous mutant. This is a significant change in the invasion probability of mutants which might/might not facilitate invasion into the proximal tissue under various micro-environmental conditions.

Moreover during carcinogenesis, it is quite possible for the existence of only two mu-

tant phenotypes with different fitness rates. We investigated this scenario by choosing a bi-modal distribution $D = \{0.5, 1.5\}$ to capture the invasion feature of mutants. It is interesting to note that the invasion probability is zero until the system reaches a particular number of advantageous mutants. The invasion probability is zero even when the system is filled with 50% of advantageous mutants. This zero invasion can be attributed to the competition between 50% of advantageous mutants and 50% of disadvantageous mutants, as well as against the host cells in the system. This suggests that under moderate (non-harsh) micro-environmental conditions, we observe the invasion probability to be zero until the system is dominated by advantageous mutants.

Due to several environmental stresses, it is quite possible that cells acquire migration potential, which is observed in metastasis. We investigated the effect of random fitness distribution widths (of mutants) on the invasion probability in the presence of high migration potential of mutants. From our analysis, we observe that migration amplifies the invasion probability as the variance increases for both advantageous and neutral mutants. In a migration-free system, the invasion probability is suppressed as the cells do not move in the system, due to which there is a higher chance of mutant extinction. However in the presence of migration, the extinction probability of mutants is small due to cell movement within the system. Hence, we observe an amplification of the invasion probability for both advantageous and neutral mutants.

We anticipate that our results can be used to understand the effects of heterogeneous tumor micro-environments on pre-neoplastic and neoplastic invasion of tissues. We emphasize that our cellular automata rules are based on existing biological assumptions within tumor micro-environments. We developed a computational framework to understand and analyze the importance of random fitness distributions (due to harsh environmental conditions) on the invasion mechanism of pre-malignant cells. Biologically, it is a known fact

that several environmental stresses (such as rigidity of tissue architecture and growth factors) can lead to the Epithelial-Mesenchymal-Transition (EMT), which is an important component of metastasis. From our analysis we have shown that under certain conditions, a neutral mutant can turn into an advantageous mutant (in the absence of migration), and that migration amplifies the invasion probability even in heterogeneous conditions. Our results can pave a way for further biological studies, and also to gain further insights into the effect of random fitnesses on the invasion probability. Although our computational model reflects a realistic heterogeneous scenario within a tumor micro-environment, we can always refine the model to make it work clinically (although this is very tough to achieve), by incorporating the fitness of a cell at a point on the grid as a function of various nutrients and oxygen supply that change temporally. Our model can be further extended to realistic tissue architectures through the study of invasion probability on unstructured meshes.

Chapter 10

Conclusions and future work

10.1 Contributions

In this thesis, we have contributed some novel approaches to clinical problems that lie at the interface of radiation oncology, radiation physics and mathematical oncology. The metamorphosis of extended field radiotherapy to involved node radiotherapy and various scientific advancements in chemotherapeutic drugs have substantially improved the survival rate of cancer patients. One important parameter that oncologists have to consider during treatment planning is the quality of life of the patient post treatment. In this context, various epidemiological, clinical and case control studies have reported that most cancer survivors are faced with the prospect of a high risk of a secondary malignancy due to anti cancer therapies.

Due to the growing body of evidence that ant-cancer therapies induced second malignancies, it has become vital to evaluate the risks associated with these therapies. Also, the shift in paradigm from photon therapy to particle therapies is currently under exten-

sive clinical investigations to maximize the local control of disease while sparing healthy tissue. Previous models in the literature have neglected the effects of radiation quality on the radio-biological and mutation induction parameters (which are considered to be the most significant) in evaluating second cancer risks. In this regard, we developed a generalized mathematical framework that incorporates an important radiation quality feature, the LET, and its dependence on the radio sensitivity parameters and mutation induction frequency. Although we have developed this for mono-energetic beams, this formalism has succeeded over other models by demonstrating the need and the importance of including radiation quality in evaluating second cancer risks.

Most anti-cancer regimens include a cocktail of treatments, particularly, a combination of chemotherapy and radiotherapy. It is of paramount importance to develop an efficient dose scheduling that can maximize tumor control and minimize second cancer risks. In this regard, we have developed a generalized mathematical model that incorporates chemotherapy and radiotherapy induced effects on second cancer risks. This model demonstrated the importance of evaluating the risks for combined modality protocols, which can also act as a potential tool to design an efficient regimen.

Several clinical studies are being carried out investigating dose painting to maximize the tumor control probability. Dose escalation is being carried out through chemotherapy alone or radiotherapy alone or as a combined regimen. In most treatments all the cancerous cells are not eliminated completely, and as a result there is a possibility of early or late stage relapse. At the same time, increasing the relapse time might require an increase in the dose, which may well result in elevated second cancer risks. We have developed a mathematical framework that incorporates relapse dynamics and the tumor control probability, along with a second cancer risks model and tested it using various fractionation schemes. Using this model, we have attempted to suggest a shift from conventional to hypo-fractionated

regimen, which may need further clinical investigations.

These comprehensive mathematical formalisms (extended IIP formalisms presented in Chapter 4, 5, 6) can be supplemented with experimental validations using patient specific data. This would greatly help radiation oncologists to gain access to individualized second cancer risks estimates, and help in developing efficient treatment regimens that can spare healthy tissue without impairing treatment to the primary tumor volume.

There has been considerable research effort focused on trying to understand the evolution of cancer using the framework of evolutionary dynamics, (both spatial and non-spatial). It is well known that some tumor initiator cells are produced during the course of the treatment. Since there is a possibility that these pre-malignant cells can become extinct, we have tried to investigate the probability of a pre-cancerous cell surviving and taking over a small population within a distorted tissue. We also investigated the heterogeneity of a given system post irradiation in two different scenarios, one with random architecture and the second with site dependent random fitness. It should be noted that these investigations have been carried out in the presence and absence of cellular motility, which up till now has not been addressed in the literature. We developed a computational approach and explored the effects of randomness of grids and meshes on the invasion probability of pre-cancerous cells; and also examined the impact of site (on a lattice) dependent random fitness of pre-malignant cells on the invasion probability. These results can provide an insight into the heterogeneity of various types of phenotypes during the tumor progression (both in primary and second cancers).

10.2 Future directions

All of the above models provide some fundamental insight into the estimation of second cancer risks induced by chemo-radio therapies. Some of most important insights are on temporal sequencing of combination of treatment strategies and the dependence of tissue specific second cancer risks. It might be more beneficial to refine the models presented in this thesis to increase the predictive capability of second cancer risks. Some of the potential refinements for these models are proposed below.

A major extension to the mathematical framework that incorporates radiation quality features would be one that includes parameters for mixed radiation fields with different energies. This would represent a major advance in theoretical predictions of second cancer risks for particle therapies. Since the anatomical structure varies between patients, it would be worthwhile developing the capability to include the dose volume histograms of each patient in order to be able to estimate the corresponding second cancer risks for individual patients. This would help radiation oncologists quantify the risks associated with various particle therapies and also be in line with current push towards personalized medicine in all branches of clinical medicine.

In Chapter 5, we presented a simple model that incorporates both chemotherapy and radiotherapy, and there are numerous extensions to this framework. It might be worthwhile to extend this to various fractionation regimens combined with chemotherapy in order to understand the effects of fractionation on second cancer risks. One possible extension is to include the interaction of ionizing radiation with chemotherapeutic agents (for instance, some agents may act as radiation sensitizers) along with the incorporation of the pharmacodynamics of chemotherapy drugs. This would enable us to get a better estimate of the effects of combined modality protocols. Moreover, there have been studies that suggest

showing that hormonal factors also play a significant role during treatment [15]. Another extension that might aid in a better understanding of second cancer risks (due to combined treatments) is to model hormonal factors like estrogen levels, etc during treatment.

It is a well known fact that hypoxic tumors are oxygen deprived and are often resistant to therapies, thus boosting the dose to the tumor might increase tumor control to some extent. Another potential direction, in the context of evaluating efficient regimens (discussed in Chapter 6), is to include the effects of oxygen tension on radio-biological parameters. This will enable oncologists to take into consideration micro-environmental effects on the radio-sensitivity parameters, and escalate the dose accordingly. It should be noted that the design of these protocols should be carried out by including recurrence dynamics in conjunction with second cancer risks models.

Biologically, it is known that a tissue consists of cells of different phenotypes such as normal stem cells, progenitor cells, differentiated cells. The radio-sensitivities vary depending on the particular phenotype. From the perspective of mathematical modeling, it would be interesting to incorporate a stem cell heirarchy in a model with a view to being able to evaluate different types of cytotoxic therapies administered individually (for instance, radiation therapy and chemotherapy can have different sensitivities) and as a combined modality treatment. Although the theoretical risk predictions might not change drastically, it would nevertheless be interesting mathematically and computationally to explore the fluctuations of various cells during the course of the treatment.

Evolutionary dynamics has played a major role in understanding the evolutionary mechanisms of cancer. In order to capture complex dynamics during carcinogenesis, we need to resort to evolutionary techniques. One of the most important and obscure phenomena is the role of cellular motility during carcinogenesis (and also in the case of in-situ breast carcinomas). A possible extension to the current work is to study the effect of random

migrative potentials on the fixation probability on spatial domains constrained by boundaries. Resistance of cells to treatments is also one of the more important clinical problems of current interest. Some of the intriguing questions related to the evolution of radiotherapy and chemotherapy resistance can be explored using the evolutionary dynamics framework. Several authors have developed multi-scale modeling techniques to investigate cancer progression. Following these approaches, it would be interesting to incorporate the effects of the micro-environment into the existing spatial framework. For instance, the proliferative (and/or the migrative) potential of a cell can be a function of oxygen concentration, nutrients, etc on the lattice. Several biological studies have supported the role of phenotype switching during cancer progression. From an evolutionary perspective, it would be interesting to examine the impact of phenotype switching on the fixation probability using a spatial evolutionary model. These results can shed some light on the EMT mechanism, which is one of the key stages in the process of metastasis.

Mathematical modeling is one of several ways through which an in depth understanding can be gained, by providing a robust in-silico framework in which to study anti-cancer therapies and their associated cancer risks. Mathematical oncology is beginning to take centre stage as one of the theoretical tools that can be used to tackle several clinical problems related to radiation science. Mathematical oncology is an interdisciplinary field, where the synergy of interaction between mathematics and oncology can provide a better understanding of cancer progression and enable the design of effective treatments to combat this.

References

[1] Weinberg RA, Biology of Cancer, Garland Science; 2 edition (May 16 2013).

[2] Hanahan D, Weinberg RA. The hallmarks of cancer. Cell 100, 5770, 2000.

[3] Hanahan D, Weinberg RA. Hallmarks of Cancer: The Next Generation, Cell 144, 2011, 646.

[4] Brenner DJ, Curtis RE, Hall EJ, Ron E, Second Malignancies in Prostate Cancer Patients After Radiotherapy Compared to Surgery, *Cancer*, Vol. 8, pp. 398-406, 2000.

[5] Travis LB, Curtis RE et al., Second malignant neoplasms among long-term survivors of ovarian cancer, *Cancer Res*, 56:15641570, 1993

[6] Beaty O III, Hudson MM, Greenwal C, et al. Subsequent malignancies in children and adolescents after treatment for Hodgkin's disease, *J Clin Oncol*, Vol. 13, pp. 603-9, 1995.

[7] Robinson LL, Mertens A, Second tumors after treatment of childhood malignancies, *Hematol. Oncol. Clin. North. Am.*, Vol. 7, pp. 401-415, 1993.

[8] Bhatia S, Robinson LL, Oberlin O, et. al., Breast cancer and other second neoplasms after childhood Hodgkin's disease, *New Engl. J. Med.*, Vol. 334, pp. 745-51, 1996.

[9] Travis LB, Gospodarowicz M, Curtis RE, et al., Lung cancer following chemotherapy and radiotherapy for Hodgkin's disease, *J Natl Cancer Inst*, 94:182192, 2002

[10] Travis LB, Hill DA, Dores GM, et al., Breast cancer following radiotherapy and chemotherapy among young women with Hodgkin disease. *JAMA* 290:465475, 2003

[11] Boice JD Jr, Engholm G, Kleinerman RA, Blettner M, Stovall M, Lisco H, et al., Radiation dose and second cancer risk in patients treated for cancer of the cervix, *Radiat. Res.*, Vol. 116, pp. 3-55, 1988.

[12] *International Commission on Radiation Units and Measurements*, Report 50, 1993, available at http://www.icru.org/index.php?option=com_content&task=view&id=72.

[13] Hodgson DC. Hematology Am Soc Hematol Educ Program. 323-329, 2011.

[14] Deniz K, O'Mahony S, Ross G, Purushotham A. Breast cancer in women after treatment for Hodgkin's disease. Lancet Oncol.2003;4:207-214.

[15] van Leeuwen FE, Klokman WJ, Van't Veer MB. et al. Effects of radiation dose, chemotherapy, and ovarian hormones on breast cancer risk following Hodgkin's Disease. Paper presented at: 8th International Conference on Malignant Lymphoma; June 12-15, 2002; Lugano, Switzerland.

[16] Weiguo Lu, Mingli Chen, Fluence-convolution broad-beam (FCBB) dose calculation, *Phys. in Med. and Bio.*, Vol. 55, pp. 7211-7229, 2010.

[17] Ahnesj A, Saxner M, Trepp A, A pencil beam model for photon dose calculation., *Med. Phys.*, Vol. 19(2), pp. 263-73, 1992.

[18] Ahnesjo A, Collapsed cone convolution of radiant energy for photon dose calculation in heterogeneous media, *Med. Phys.*, Vol. 16, pp. 577-92, 1989.

[19] Ye AH, Haijun S, Zhe C, Sumin Z, Fang-Fang Yin, Evaluation of an electron Monte Carlo dose calculation algorithm for electron beams, *J. App. Clin. Med. Phys.*, Vol 9(3), 2008.

[20] Agostinelli S, Allison J, Amako K, Apostolakis J, Araujo H, Arce P, Asai M, Axen D, Banerjee S, Barrand G, Behner F, Bellagamba L, Boudreau J, Broglia L, Brunengo A, et al. Geant4: A simulation toolkit. Nuclear Instruments and Methods A 2003, 506:250303.

[21] Chauvie S, Francis Z, Guatelli S, Incerti S, Mascialino B, Montarou G, Moretto P, Nieminen P, Pia MG. Monte Carlo simulation of interactions of radiation with biological systems at the cellular and DNA levels: The Geant4-DNA project. Radiation Research 2006, 166:652689.

[22] Villagrasa C, Francis Z, Incerti S. Physical models implemented in the GEANT4-DNA extension of the GEANT-4 toolkit for calculating initial radiation damage at the molecular level Radiat Prot Dosimetry. 2011 Feb;143(2-4):214-8.

[23] Goodhead DT Initial events in the cellular effects of ionizing-radiations: clustered damage in DNA Int. J. Radiat. Biol. 1994, 65 717.

[24] Goodhead DT Energy deposition stochastics and track structure: What about the target ? Radiat. Prot. Dosim. 2006, 122 315.

[25] Goodhead D T, Thacker J and Cox R Effects of radiations of different qualities on cells: molecular mechanisms of damage and repair Int. J. Radiat. Biol. 1993, 63 54356.

[26] Grosswendt B and Pszona S The track structure of alpha-particles from the point of view of ionization-cluster formation in nanometric volumes of nitrogen particles Radiat. Environ. Biophys. 2002, 41 91102.

[27] Grosswendt B, Pszona S and Bantsar A New descriptors of radiation quality based on nanodosimetry, a first approach biology Radiat. Prot. Dosim. 2007, 126 43244.

[28] McNamara AL, Guatelli S, Prokopovich DA, Reinhard MI, Rosenfeld AB. A comparison of X-ray and proton beam low energy secondary electron track structures using the low energy models of Geant4, Int J Radiat Biol. 2012 Jan;88(1-2):164-70.

[29] Brenner DJ, Ward JF. Constraints on energy deposition and target size of multiply damaged sites associated with DNA double-strand breaks. International Journal of Radiation Biology 1992, 61:737748.

[30] Bedford J S Sublethal damage, potentially lethal damage, and chromosomal-aberrations in mammalian-cells exposed to ionizing-radiations Int. J. Radiat. Oncol. Biol. Phys. 1991, 21 145769.

[31] Alloni D, Campa A, Belli M, Esposito G, Facoetti A, Friedland W, Liotta M, Mariotti L, Paretzke HG, Ottolenghi A. A Monte Carlo study of the radiation quality dependence of DNA fragmentation spectra. Radiat Res. 2010 Mar;173(3):263-71.

[32] Byrne HL, McNamara AL, Domanova W, Guatelli S, Kuncic Z. Radiation damage on sub-cellular scales: beyond DNA Phys Med Biol. 2013, Mar 7;58(5):1251-67.

[33] Prise K M, Schettino G, Folkard M and Held K D New insights on cell death from radiation exposure Lancet Oncol. 2005, 6 5208.

[34] Rodemann H P and BlaeseM A Responses of normal cells to ionizing radiation Semin. Radiat. Oncol. 2007, 17 8188.

[35] Shao C Targeted cytoplasmic irradiation induces bystander responses Proc. Natl Acad. Sci. USA 2004, 101 13495500.

[36] Paganetti H, Assessment of the risk for developing a second malignancy from scattered and secondary radiation in radiation therapy, *Health Phys*, 2012 Nov;103(5):652-61.

[37] Grosswendt B, Pszona S and Bantsar A New descriptors of radiation quality based on nanodosimetry, a first approach biology Radiat. Prot. Dosim. 2007, 126 43244.

[38] Garty G, Schulte R, Shchemelinin S, Grosswendt B, Leloup C, Assaf G, Breskin A, Chechik R and Bashkirov V First attempts at prediction of DNA strand-break yields using nanodosimetric data Radiat. Prot. Dosim. 2006, 122 451-4.

[39] Garty G, Schulte R, Shchemelinin S, Leloup C, Assaf G, Breskin A, Chechik R, Bashkirov V, Milligan J and Grosswendt B A nanodosimetric model of radiation-induced clustered DNA damage yields Phys. Med. Biol. 2010, 55 76181.

[40] Lazarakis P, Bug MU, Gargioni E, Guatelli S, Rabus H, Rosenfeld AB. Comparison of nanodosimetric parameters of track structure calculated by the Monte Carlo codes Geant4-DNA and PTra, Phys Med Biol. 2012, Mar 7;57(5):1231-50.

[41] Puck TT, Marcus PI, Action of X-rays on mammalian Cells, *J. Exp. Med.*, 103, pp. 653-666, 1956

[42] Chadwick KH and Leenhouts HP, A molecular theory of cell survival, *Phys. Med. Biol.*, 18, pp. 78-87 1973

[43] Annex F, http://www.unscear.org/unscear/en/publications/1993.html

[44] Nordling, CO, A new theory on the cancer inducing mechanism. Br J Cancer, 1953. 7: pp. 68-72.

[45] Armitage, P. and R. Doll, The age distribution of cancer and a multi-stage theory of carcinogenesis. Br J Cancer, 1954. VIII: pp. 1-12.

[46] Nilsson P, Thames HD, Joiner MC, A generalized formulation of the 'incomplete-repair' model for cell survival and tissue response to fractionated low dose-rate irradiation. Int J Radiat Biol, 1990. 57(1): pp. 127-42.

[47] Thames HD, An 'incomplete-repair' model for survival after fractionated and continuous irradiations. Int J Radiat Biol Relat Stud Phys Chem Med, 1985. 47(3): pp. 319-39

[48] Thames HD. and Henry JH., Fractionation in radiotherapy, Taylor and Francis Ltd, illustrated edition edition, July 1987..

[49] Dale RG, The application of the linear-quadratic model to fractionated radiotherapy when there is incomplete normal tissue recovery between fractions, and possible implications for treatments involving multiple fractions per day. Br J Radiol, 1986. 59(705): pp. 919-27.

[50] Curtis SB, Lethal and potentially lethal lesions induced by radiation-a unified repair model. Radiat Res, 1986. 106(2): pp. 252-70.

[51] Tobias CA, The repair-misrepair model in radiobiology: comparison to other models. Radiat Res Suppl, 1985. 8: pp. S77-95

[52] Sachs RK, et al., Second cancers after fractionated radiotherapy: Stochastic population dynamics effects. J Theor Biol, 2007.

[53] Sachs RK, Brenner DJ., Solid tumor risks after high doses of ionizing radiation, Proc. National Acad. Sci., Vol. 102, pp. 13040-13045, 2005.

[54] Shuryak I, Sachs RK, Brenner DJ, et. al., A new view of radiation induced cancer-integrating short-term and long-term processes-Part I, Radiat. Environ. Biophys., Vol. 48, pp. 263-274, 2009.

[55] Shuryak I, Sachs RK, Brenner DJ, et. al., A new view of radiation induced cancer-integrating short-term and long-term processes-Part II, Radiat. Environ. Biophys., Vol. 48, pp. 275-286, 2009.

[56] Shuryak I, et al., Radiation-induced leukemia at doses relevant to radiation therapy: modeling mechanisms and estimating risks. J Natl Cancer Inst, 2006. 98(24): pp. 1794-806.

[57] Little MP, A multi-compartment cell repopulation model allowing for intercompartmental migration following radiation exposure, applied to leukaemia. J Theor Biol, 2007. 245(1): pp. 83-97.

[58] Schneider U, Kaser-Hotz B, Radiation risk estimates after radiotherapy: application of the organ equivalent dose concept to plateau dose-response relationships. Radiat Environ Biophys, 2005. 44(3): pp. 235-9.

[59] Preston DL, Ron E, Tokuoka S, Funamoto S, Nishi N, Soda M, Mabuchi K and Kodama K. Solid Cancer Incidence in Atomic Bomb Survivors: 1958-1998, Radiat Res. 2007, 168(1):1-64.

[60] Dasu A, Toma-Dasu I, et al., The use of risk estimation models for the induction of secondary cancers following radiotherapy, *Acta Oncol.*, 44: pp. 339-47, 2005

[61] Dasu A, Toma-Dasu I. Dose-effects models for risk relationship to cell survival parameters, *Acta Oncol.*, 44: pp. 829-35, 2005

[62] Wheldon EG, Lindsay KA, and Wheldon TE, The dose-response relationship for cancer incidence in a two-stage radiation carcinogenesis model incorporating cellular repopulation. Int J Radiat Biol, 2000. 76(5): pp. 699-710

[63] Lindsay KA, Wheldon EG, et. al., Radiation carcinogenesis modeling for risk of treatment-related second tumors following radiotherapy, *Br. J. Radiol.*, Vol. 74, pp. 529-536, 2001.

[64] Zaider M, Wuu CS, The effects of sublethal damage recovery and cell cycle progression on the survival probability of cells exposed to radioactive sources. Br J Radiol, 1995. 68(805): pp. 58-63.

[65] Hahnfeldt, P. and L. Hlatky, Resensitization due to redistribution of cells in the phases of the cell cycle during arbitrary radiation protocols. Radiat Res, 1996.145(2): pp. 134-43.

[66] Hahnfeldt, P. and L. Hlatky, Cell resensitization during protracted dosing of heterogeneous cell populations. Radiat Res, 1998. 150(6): pp. 681-7.

[67] Weber DC, Johanson S, Peguret S, Cozzi L, Olsen DR, Predicted Risk of Radiation-Induced Cancers after Involved Field and Involved Node Radiotherapy with or without Intensity Modulation for Early-Stage Hodgkin Lymphoma in Female Patients, International Journal of Radiation Oncology Biol. Phys., Vol. 77, pp. 1-8, 2010.

[68] Hodgson D, Sachs RK, Brenner DJ, et. al., Individualized estimates of second cancer risks after contemporary radiation therapy for Hodgkin Lymphoma, Cancer, 110(11), pp. 2576-86, 2007.

[69] Aleman BMP, van den Belt-Dusebout AW, Klokman WJ, et al. Long-term cause-specific mortality of patients treated for Hodgkin's disease. J Clin Oncol. 2003, 21:3431-3439

[70] Hill DA, Gilbert E, Dores GM, et al. Breast cancer risk following radiotherapy for Hodgkin lymphoma: modification by other risk factors. Blood, 2005; 106:3358-3365.

[71] Gilbert E, Stovall M, Gospodarowicz M, et al. Lung cancer after treatment for Hodgkins disease: focus on radiation effects. Radiat Res. 2003;159:161-173

[72] U.S. Preventive Services Task Force. Screening for colorectal cancer: recommendation and rationale. Ann Intern Med. 2002; 137:129-131. Comment in: Ann Intern Med. 2003; 138:356-357; author reply, 357. Summary for patients in: Ann Intern Med. 2002; 137:I38.

[73] Swerdlow AJ, Barber JA, Hudson GV, et al. Risk of second malignancy after Hodgkins disease in a collaborative British cohort: the relation to age at treatment. J Clin Oncol. 2000; 18:498-509.

[74] Bhatia S, Yasui Y, Robison LL, et al. High risk of subsequent neoplasms continues with extended follow-up of childhood Hodgkins disease: report from the Late Effects Study Group. J Clin Oncol. 2003; 21:4386-4394.

[75] Dores GM, Metayer C, Curtis RE, et al. Second malignant neoplasms among long-term survivors of Hodgkins disease: a population-based evaluation over 25 years. J Clin Oncol. 2002; 20:3484-3494.

[76] Hodgson DC, Gilbert ES, Dores GM, et al. Long-term solid cancer risk among five-year survivors of Hodgkins lymphoma. J Clin Oncol. 2007; 25:1489-1497

[77] Travis LB, Hill D, Dores GM, et al. Cumulative absolute breast cancer risk for young women treated for Hodgkin lymphoma. J Natl Cancer Inst. 2005; 97:1428-1437

[78] Aleman BM, Klokman WJ, van Leeuwen FE. Second primary tumors in patients treated at an early age for Hodgkin's disease. Ned Tijdschr Geneeskd. 2000; 144(32):1517-20.

[79] Xu XG, Bednarz B, Paganetti H, A review of dosimetry studies on external-beam radiation treatment with respect to second cancer induction, Phys Med Biol. 2008 Jul 7;53(13):R193-241

[80] Newhauser WD, Durante M., Assessing the risk of second malignancies after modern radiotherapy, Nat Rev Cancer. 2011 Jun;11(6):438-48

[81] Allen PD, Chaudhri MA, The dose contribution due to photonuclear reactions during radiotherapy Med. Phys. 9 9045, 1982

[82] Allen PD, Chaudhri MA, Photoneutron production in tissue during high energy bremsstrahlung radiotherapy. Phys Med Biol. 1988 Sep;33(9):1017-36

[83] Allen PD, Chaudhri MA, Charged photoparticle production in tissue during radiotherapy, Med Phys. 1997 Jun;24(6):837-9

[84] Perez AC and Brady LW. Principles and Practice of Radiation Oncology. Philadelphia : J.B. Lippincott, c1992.

[85] Hall EJ and Giaccia AJ. Radiobiology for the Radiologist. Philadelphia : Wolters Kluwer Health/Lippincott Williams and Wilkins, 7th edn. c2012

[86] Taddei PJ, Mirkovic D, Fontenot JD, Giebeler A, Zheng Y, Kornguth D, Mohan R, Newhauser WD, Stray radiation dose and second cancer risk for a pediatric patient receiving craniospinal irradiation with proton beams, Phys Med Biol. 2009 Apr 21;54(8):2259-75

[87] Jarlskog CZ, Paganetti H, Risk of developing second cancer from neutron dose in proton therapy function of field characteristics, organ, AND patient age, Int J Radiat Oncol Biol Phys. 2008 Sep 1;72(1):228-35

[88] Paganetti H, Assessment of the risk for developing a second malignancy from scattered and secondary radiation in radiation therapy, Health Phys. 2012 Nov;103(5):652-61

[89] Brenner DJ, Hall EJ, Secondary neutrons in clinical proton radiotherapy: a charged issue, Radiother Oncol. 2008 Feb;86(2):165-70

[90] Hall EJ, The impact of protons on the incidence of second malignancies in radiotherapy, Technol Cancer Res Treat. 2007 Aug;6(4 Suppl):31-4

[91] Hall EJ, Intensity-modulated radiation therapy, protons, and the risk of second cancers, Int J Radiat Oncol Biol Phys. 2006 May 1;65(1):1-7.

[92] Schneider U, Lomax A, Lombriser N. Comparative risk assessment of secondary cancer incidence after treatment of Hodgkin's disease with photon and proton radiation. Radiat Res. 2000;154:382-8

[93] Wilkens JJ and Oelfke U. Analytical linear energy transfer calculations for proton therapy. Med Phys. 2003, 30(5) 806-15.

[94] Wilkens JJ and Oelfke U. A phenomenological model for the relative biological effectiveness in therapeutic proton beams. Phys Med Biol. 2004, 49(13); 2811-25

[95] Hei TK, Chen DJ, Brenner DJ, Hall EJ. Mutation induction by charged particles of defined linear energy transfer. Carcinogenesis. 1988; 9(7):1233-6.

[96] Yatagai F. Mutations induced by heavy charged particles. Biol Sci Space. 2004; 18(4):224-34.

[97] Belli M, Cera F, Cherubini R, Dalla Vecchia M, et al. RBE-LET relationships for cell inactivation and mutation induced by low energy protons in V79 cells: further results at the LNL facility. Int J Radiat Biol. 1998; 74(4):501-9.

[98] Wenzl T and Wilkens JJ. Modelling of the oxygen enhancement ratio for ion beam radiation therapy. Phys Med Biol. 2011; 56(11):3251-68

[99] Chen DJ, Tsuboi K, Nguyen T, Yang CT. Charged-Particle Mutagenesis II. Mutagenic effects of high energy charged particles in human fibroblasts. Adv Space Res. 1994; 14(10):347-54

[100] Chen Y, Ahmad S. Empirical model estimation of relative biological effectiveness for proton beam therapy. Radiat Prot Dosimetry. 2012; 149(2):116-23

[101] Furusawa Y, Fukutsu K, Aoki M, et al. Inactivation of aerobic and hypoxic cells from three different cell lines by accelerated (3)He-, (12)C- and (20)Ne-ion beams. Radiat Res. 2000; 154(5):485-96.

[102] Goodhead DT, Belli M, Mill AJ, et al. Direct comparison between protons and alpha-particles of the same LET: I. Irradiation methods and inactivation of asynchronous V79, HeLa and C3H 10T1/2 cells. Int J Radiat Biol. 1992; 61(5):611-24.

[103] Belli M, Goodhead DT, Ianzini F, et al. Direct comparison of biological effectiveness of protons and alpha-particles of the same LET. II. Mutation induction at the HPRT locus in V79 cells. Int J Radiat Biol. 1992; 61(5):625-9

[104] Belli M, Cherubini R, Finotto S, Moschini G, Sapora O, Simone G, Tabocchini MA., RBE-LET relationship for the survival of V79 cells irradiated with low energy protons, Int J Radiat Biol. 1989 Jan;55(1):93-104

[105] Folkard M, Prise KM, Vojnovic B, Davies S, Roper MJ, Michael BD, The irradiation of V79 mammalian cells by protons with energies below 2 MeV . I : Experimental arrangement and measurements of cell survival, Int J Radiat Biol. 1989 Sep;56(3):221-37.

[106] Inskip PD, Robinson LL, Stovall M, et al. 2009. Radiation dose and breast cancer risk in the childhood cancer survivor study. J Clin Oncol. 27 (24):3901-3907

[107] Travis LB, Hill DA, Dores MG, et al. 2003. Breast cancer following Radiotherapy and Chemotherapy among young women with Hodgkins Disease, JAMA. 290(4):465-475

[108] Norton L, Simon R. 1986. The NortonSimon hypothesis revisited. Cancer Treat. Rep. 70, 163169.

[109] Norton A. 1988. A Gompertzian model of human breast cancer growth. Cancer Res. 48, 70677071.

[110] Bokemeyer C, Schmoll HJ, Kuczyk MA, Beyer J, Siegert W. 1995. Risk of secondary leukemia following high cumulative doses of etoposide during chemotherapy for testicular cancer. J Natl Cancer Inst. 4; 87(1):58-60.

[111] Haupt R, Fears TR, Rosso P, Colella R, et al. 1994. Increased risk of secondary leukemia after single-agent treatment with etoposide for Langerhans cell histiocytosis. Pediatr Hematol Oncol. 11(5):499-507.

[112] Tucker MA, Meadows AT, Boice JD Jr, Stovall M, et al. 1987. Leukemia after therapy with alkylating agents for childhood cancer. J Natl Cancer Inst. 78(3):459-64.

[113] Samuels DC, Li C, Li B, Song Z, Torstenson E, et al. 2013. Recurrent Tissue-Specific mtDNA Mutations Are Common in Humans PLoS Genetics 9(11): e1003929.

[114] Tomasetti C, Vogelstein B, Parmigiani G. 2013. Half or more of the somatic mutations in cancers of self-renewing tissues originate prior to tumor initiation. Proc Natl Acad Sci. 5;110(6):1999-2004

[115] O'Rourke SF, McAneney H, Hillen T. Linear quadratic and tumour control probability modelling in external beam radiotherapy. J Math Biol. 2009 Apr;58(4-5):799-817

[116] Marková J, Maaloufov J, Strtesk J, Feltl D, Kozk T. Late recurrence of Hodgkin's disease 20 years after initial diagnosis. Personal observation of two cases and a literature review. VnitrLek. 2002 Feb;48(2):157-60

[117] Schneider U, Besserer J, Mack A. Hypofractionated radiotherapy has the potential for second cancer reduction. Theor Biol Med Model. 2010 Feb 11;7:4.

[118] Livsey JE, Cowan RA, Wylie JP, Swindell R, Read G, Khoo VS, Logue JP. Hypofractionated conformal radiotherapy in carcinoma of the prostate: five-year outcome analysis. Int J Radiat Oncol Biol Phys. 2003 Dec 1;57(5):1254-9

[119] Ortholan C, Hannoun-Lvi JM, Ferrero JM, Largillier R, Courdi A. Long-term results of adjuvant hypofractionated radiotherapy for breast cancer in elderly patients. Int J Radiat Oncol Biol Phys. 2005 Jan 1;61(1):154-62.

[120] Armitage P. Multistage models of carcinogenesis. Environ Health Perspect. 1985, 63: 195201.

[121] Armitage P, Doll R. The age distribution of cancer and a multi- stage theory of carcinogenesis. Br J Cancer. 2004, 91(12): 19831989.

[122] Huang L, Snyder AR, Morgan WF. Radiation-induced genomic instability and its implications for radiation carcinogenesis, Oncogene, 22, 5848-5854, 2003.

[123] Michor F, Nowak MA, et. al., Dynamics of cancer progression, *Nature Reviews*, Vol. 4, pp. 197-206, 2004.

[124] Michor F, Nowak MA, Iwasa Y, Stochastic dynamics of metastasis formation, *J. Theor. Biol.*, 240(4), pp. 521-30, 2006

[125] Nowak MA, Michor F, Komarova NL, Iwasa Y, Evolutionary dynamics of tumor suppressor gene inactivation, *Proc. Natl. Acad. Sci.*, 101(29), pp. 10635-8, 2004

[126] Komarova NL and Nowak MA, Language dynamics in finite populations, *J. Theor. Biol.*, 221, pp. 445457, 2003

[127] Moran P, The Statistical Processes of Evolutionary Theory Oxford: Clarendon; 1962.

[128] Nowak, MA, Five rules for the evolution of cooperation, *Science* Vol. 314, pp. 1560-1563, 2006b.

[129] Taylor C, Nowak MA, Transforming the dilemma, *Evolution*, Vol. 61, pp. 2281-2292, 2007.

[130] Szathmary E, Demeter L, Group selection of early replicators and the origin of life, *J. Theor. Biol.*, Vol. 128, pp. 463-486, 1987.

[131] Maynard S, Szathmary J, *The Major Transitions in Evolution*, Freeman, Oxford, 1995.

[132] Wilson DS, Sober E, *Unto Others: The Evolution and Psychology of Unselfish Behavior*, Harvard University Press, Cambridge, 1998.

[133] Boyd R, Richerson, PJ, Group beneficial norms spread rapidly in a structured population, *J. Theor. Biol.*, Vol. 215, pp. 287-296, 2002.

[134] Bowles S, *Microeconomics-Behavior, Institutions, and Evolution*, Princeton Univ. Press, Princeton, 2004.

[135] Bowles S, Group competition, reproductive leveling, and the evolution of human altruism, *Science*, Vol. 314, pp. 1569-1572, 2006.

[136] Traulsen A, Nowak MA, Evolution of cooperation by multi-level selection. *Proc. Natl. Acad. Sci. USA*, Vol. 103, pp. 10952-10955, 2006.

[137] Lehmann L, Keller L, West S, Roze D, Group selection and kin selection: Two concepts but one process, *Proc. Natl. Acad. Sci. USA*, Vol. 104, pp. 6736-6739, 2007.

[138] Lieberman E, Hauert C, Nowak MA, Evolutionary dyamics on graphs, *Nature*, Vol. 433, pp. 312-316, 2005.

[139] Komarova NL, Spatial stochastic models for cancer initiation and progression, *Bull. Math. Biol.*, Vol. 68, pp. 1573-1599, 2006.

[140] Craig JT, John SL, Dwayne S and Komarova NL, Selection in spatial stochastic models of cancer: Migration as a key modulator of fitness, *Biology Direct*, 5:21, 2010.

[141] Kaveh K, Manem VSK, Kohandel M, Sivaloganathan S. Random-Fitness Voter Model on Regular Graphs: An Analytical Approach. (In preparation), 2014.

[142] Martin A. Nowak, *Evolutionary dynamics, exploring equations of life*, The Belknap press of Harvard university press, 2006.

[143] Wodarz D and Komarova NL, *Computational Biology of Cancer*, World Scientific, 2005.

[144] Rajagopalan H, Nowak MA, et. al., The significance of unstable chromosomes in colorectal cancer, *Natue Reviews*, Vol. 3, pp. 695-700, 2003.

[145] Whigham P, Dick G, Evolutionary dynamics on graphs: The Moran process. *In: Simulated Evolution and Learning*, LNCS 4247, Springer, pp. 1-8, 2006.

[146] Whigham P, Dick G, How does space alter the formulation of evolutionary models? *In: Whigham P (ed.) Proceedings of the 18th Annual Colloquium of the Spatial Information Research Center (SIRC)*, Otago University Press, Dunedin, New Zealand, pp. 79-83, 2006.

[147] Whigham P, Dick G, Evolutionary dynamics for the spatial Moran process, *Genetic Programming and Evolvable Machines*, Vol 9, pp. 157-170, 2008.

[148] Maruyama T, A markov process of gene frequency change in a geographically structured population, *Genetics.*, 76, 367377, 1974.

[149] Maruyama T, A simple proof that certain quantities are independent of the geographical structure of population, *Theor Popul Biol.*, 5, 148154, 1974.

[150] Slatkin T, Fixation Probabilities and Fixation Times in a Subdivided Population, *Evolution*, 35(3), 477-488, 1981.

[151] Lieberman E, Hauert C, and Nowak MA, Evolutionary dynamics on graphs, *Nature*, 433, 312-316, 2005.

[152] Houchmandzadeh B, Vallade M, The fixation probability of a beneficial mutation in a geographically structured population, *New J. Physics*, 13, 073020, 2011.

[153] Nowell PC, The clonal evolution of tumor cell populations, *Science*, 194, 2328, 1976.

[154] Komarova NL, Sengupta A, Nowak MA, Mutation-selection networks of cancer initiation: tumor suppressor genes and chromosomal instability, *J Theor Biol*, 223(4):433-450, 2003.

[155] Nowak MA, Michor F, Komarova NL, Iwasa Y, Evolutionary dynamics of tumor suppressor gene inactivation, *Proc. Natl Acad. Sci U.S.A.*, 101(29):10635-10638, 2004.

[156] Michor F, Iwasa Y, Rajagopalan H, Lengauer C, Nowak MA, Linear model of colon cancer initiation, *Cell Cycle*, 3(3):358-362, 2004.

[157] Iwasa Y, Michor F, Nowak MA: Stochastic tunnels in evolutionary dynamics, *Genetics*, 166(3):1571-1579, 2004.

[158] Komarova NL, Loss- and gain-of-function mutations in cancer: mass action, spatial and hierarchical models, *J Stat Phys*, 128:413-446, 2007.

[159] Thalhauser CJ, Lowengrub JS, Stupack D and Komarova NL, Selection in spatial stochastic models of cancer: Migration as a key modulator of fitness, *Biol Direct*, 5:21, 2010.

[160] Foo J, Leder K and Michor F, Stochastic dynamics of cancer initiation, *Phys Biol.*, 8 015002, 2011.

[161] Maruyama T, On the fixation probability of mutant genes in a subdivided population, *Genet Res.*, 15: 221225, 1970.

[162] Deutsch A, Dormann S, Cellular automation modeling of biological pattern formation, Birkhauser, Boston, 2005.

[163] Byrne H, Alarcn T, Owen M, Webb S, Maini P, Modeling Aspects of Cancer Dynamics: A Review, *Phil. Trans. R. Soc. A*, 364:1563-1578, 2006.

[164] Anderson A, Chaplain M, Rejniak K, Fozard J, Single-cell based models in biology and medicine, *Math Med Biol*, 25:185-186, 2008.

[165] Quaranta V, Rejniak K, Gerlee P, Anderson A, Invasion emerges from cancer cell adaptation to competitive microenvironments: Quantitative predictions from multiscale mathematical models, *Sem Cancer Biol.*, 18:338-348, 2008.

[166] Sood V, Antal T, Redner S, Voter Models on Heterogeneous Networks, *Phys Rev E Stat Nonlin Soft Matter Phys*, 77, 2008.

[167] Martin A. Nowak, Evolutionary Dynamics: Exploring the Equations of Life, Belknap Press; 1 edition (Oct. 29 2006).

[168] Antal T, Redner S, Sood V. Evolutionary Dynamics on Degree-Heterogeneous Graphs, *Phys Rev Lett*, 2006, 96, 188104.

[169] Maruyama, T. (1970a) On the fixation probability of mutant genes in a sub- divided population. Genet. Res. 15, 221?225.

[170] Manem VSK, Kohandel M, Komarova NL, Sivaloganathan S, Spatial invasion dynamics on random and unstructured meshes: Implications for heterogeneous tumor populations, J Theor Biol 349 (2014) 66-73.

[171] Naoki Masuda, N. Gibert, and S. Redner, Heterogeneous voter models, Phys. Rev. E 82, 010103(R) ? Published 27 July 2010.

[172] Fedotov S and Iomin A. (2008) Probabilistic approach to a proliferation and migration dichotomy in tumor cell invasion. Phys. Rev. E 77, 031911.

[173] Kimura M. Process leading to quasi-fixation of genes in natural populations due to random fluctuation of selection intensities. Genetics 39, 280-295, 1954.

[174] VSK Manem, M Kohandel, DC Hodgson, MB Sharpe, S Sivaloganathan. The effect of Radiation Quality on the risks of Second Malignancies, 2014. (Submitted to Physics in Medicine and Biology)

[175] VSK Manem, M Kohandel, S Sivaloganathan. A Monte Carlo investigation of radiation injury analysis at sub-cellular scales and DNA damage spectrum analysis induced by Proton and Alpha of same LET, 2014. (Submitted to International Journal of Radiation Biology)

[176] VSK Manem, M Kohandel, DC Hodgson, S Sivaloganathan. Mathematical modeling of second cancer risks induced by adjuvant, neo-adjuvant and concurrent therapies, 2014. (Submitted to Mathematical Medicine and Biology)

[177] VSK Manem, A Dhawan, M Kohandel, S Sivaloganathan. An optimal treatment regimen to reduce second cancer risks, 2014. (Submitted to Medical Physics)

[178] VSK Manem, K Kaveh, M Kohandel, NL Komarova, S Sivaloganathan. Modeling Invasion Dynamics with Spatial Random-Fitness due to Micro-environment. (Submitted to PLos Computational Biology).

[179] Bethe HA. Ionization power of a neutrino, Proc. Cambridge Philos. Soc., Vol. 31, 108, 1935.

[180] Brenner DJ, Hlatky LR, Hahnfeldt PJ, Hall EJ, Sachs RK. A convenient extension of the linear-quadratic model to include redistribution and reoxygenation., Int J Radiat Oncol Biol Phys. 32(2):379-90.

[181] Hillen T, de Vries G, Gong J, Finlay C. From cell population models to tumor control probability: including cell cycle effects. Acta Oncol, 49(8):1315-23.

[182] Chen J, Sprouffske K, Huang Q, Maley CC. Solving the Puzzle of Metastasis: The Evolution of Cell Migration in Neoplasms. PLoS One, 6(4):e17933, 2011.

[183] Evdokimova V, Tognon C, Ng T, Sorensen PH. Reduced proliferation and enhanced migration: two sides of the same coin? Molecular mechanisms of metastatic progression by YB-1. Cell Cycle, 8(18):2901-6, 2009.